INVESTIGATING THE FREQUENCY BEHAVIOR OF FLUIDIC OSCILLATORS AND THEIR APPLICATION AS ACTIVE FLOW CONTROL FOR AN SNLF AIRFOIL

BY

CHRISTOPHER COLLETTI

THESIS

Submitted in partial fulfillment of the requirements
for the degree of Master of Science in Aerospace Engineering
in the Graduate College of the
University of Illinois at Urbana-Champaign, 2019

Urbana, Illinois

Adviser:

Assistant Professor Phillip J. Ansell

Abstract

This current study was performed to investigate the effect of geometric variation on the frequency behavior of fluidic oscillators. Fluidic oscillators are able to passively generate a self-induced, self-sustained sweeping planar jet that is highly dependent on internal geometries and inlet conditions. Frequency data was collected for 78 parametric variations of fluidic oscillators under different inlet conditions. A multi-variate non-linear regression procedure was used to build a model to predict the frequency behavior of a fluidic oscillator given a set of internal geometries and inlet conditions.

The SNLF S414 airfoil is a multi-element airfoil with an open slot to promote a laminar boundary layer across the entire fore element and large portions of the aft element. Active unsteady flow control using embedded fluidic oscillators was identified as a potential source to improve the flow field and maximize the lift of a multi-element system like the SNLF S414. The predictive model was used to design a set of fluidic oscillators to reach desired non-dimensional frequencies and C_μ when embedded in the SNLF S414 airfoil. The SNLF S414 airfoil was tested at $Re_c = 1.8x10^6$ in a 3-ft x 4-ft low-speed, low-turbulence wind tunnel with fluidic oscillators embedded in the aft element at x/c = 0.7 and x/c = 0.8 and applied actuation at various C_μ. Two different configurations of the SNLF S414 airfoil were tested with and without the applied actuation at both locations. This data will be used to inform additional studies investigating multi-element SNLF style airfoils with unsteady active flow control.

Acknowledgements

The work I completed here would not have been possible without the guidance and support of my advisor Prof. Phil Ansell. He has been tremendously helpful and patient with me throughout the completion of my research and I find myself very fortunate to have had the opportunity to have him as my advisor.

This work was supported by NASA University Leadership Initiative contract #NNX17AJ95A "Advanced Aerodynamic Design Center for Ultra-Efficient Commercial Vehicles." I would like to thank James Coder of the University of Tennessee, Knoxville for helpful interactions, and Koushik Datta from NASA Research Park at Ames Research Center for serving as the Technical Monitor for the ULI program.

I would like to express my gratitude to my undergraduate advisor Prof. Ray LeBeau at Saint Louis University who provided guidance and direction during my undergraduate research experience. He provided invaluable support that helped me achieve my academic goals and fostered my interest in research.

I am thankful to the friends I made at Illinois who made me feel at home during my time here. I am thankful for the support the members of the Aerodynamics and Unsteady Flows research group gave and their help with the completion of experiments in the Aerodynamic Research Laboratory. I am grateful for the many insightful conversations I have had that made my daily work more enjoyable.

Finally, I would like to thank my family and loved ones for their unending support and encouragement throughout the years. They have been an integral part of my life and I would not have become the person I am today without their support.

Table of Contents

List of Figures

List of Tables

Nomenclature

AR_o	Aspect ratio at the outlet
A	Area
b	Airfoil span or calculated coefficient
c	Chord
C	Empty test-section area or coefficient
C_d	Coefficient of drag
C_l	Coefficient of lift
$C_{m,LE}$	Coefficient of moment for the leading edge
$C_{m,c/4}$	Coefficient of moment for the quarter chord
C_P	Coefficient of pressure
C_μ	Coefficient of Momentum
D'	Sectional drag force
f	Frequency
F^+	Strouhal number
h	Test section height
K_l	Constant parameter
l_c	Characteristic length
l_o	Fluidic oscillator outlet length
l_t	Fluidic oscillator inlet/throat length
l_w	Fluidic oscillator wedge length
$\dot{m}_{jet}$	Mass flow rate through an individual oscillator
n	Number of fluidic oscillators/coefficients/samples
N	N observations
N_{esb}	Number of realizations in the data ensembles
p	Population sample size or probability
P	Pressure
q	Dynamic pressure
R	Specific ideal gas constant

$R^2{}_{adj}$	Adjusted R^2 value to better represent a multivariate scheme
Re	Reynolds number
$S_{(N)}$	Standard deviation of N observations
$se(\,)$	Standard deviation of a given variable
t	Fluidic oscillator or airfoil thickness
t^*	Student t-statistic
T	Temperature
u	Velocity
U	Velocity or uncertainty
v	Voltage
$\dot{v}$	Volume flow rate
V_m	Estimated airfoil model volume
x	Variable
X	Matrix of x-variables
$X(j)$	Sample voltage
$X_{(N)}$	Mean of N observations
y	Variable
Y	Matrix of y-variables

Greek Symbols

α	Angle of attack
α_E	Significance level to entry
α_R	Significance level to remove
β_j	Actual coefficient corresponding to jth x-variable
Δ	Change in a given variable
δ_f	Flap deflection angle
∂	Partial derivative
ε	Velocity increment factor
ϵ	Residual error

θ	Calculated angle
μ	Dynamic Viscosity
ρ	Density
σ	Empirically derived variable for streamline curvature effect

Subscripts

∞	Free Stream
a	Axial
amb	Ambient
atm	Atmospheric
cor	Corrected value
f	Flap
i	Index
j	Index
l	Lower Surface
m	Model
max	Maximum value
n	Normal
s	Static or Samples
sb	Solid Blockage
ss	Settling Section
ts	Test Section
u	Uncorrected Value or Upper Surface
wb	Wake Blockage
w	Wake

Abbreviations

CAD	Computer aided design
CFD	Computational Fluid Dynamics
DFT	Discrete Fourier Transform

FFT	Fast Fourier Transform
HLC	High Lift Configuration
ID	Inner Diameter
MVR	Multivariate regression
PDB	Positive displacement blower
PSD	Power Spectral Density
RMS	Root-mean square
SLA	Stereo-lithography
SNLF	Slotted Natural Laminar Flow
VFD	Voltage frequency drive
ZNMF	Zero Net Mass Flux

Chapter 1: Introduction

Fluidic oscillators were developed over fifty years ago at the Harry Diamond Laboratories as fluidic logic devices. Currently they are most commonly associated with liquids as the working fluid for windshield washers, sprinklers, shower heads, whirlpools and more. These unique devices generate a continuous, spatially oscillating jet with no moving parts. When supplied with a fluid source, the oscillations are passively self-induced and self-sustained. They generate a bi-stable effect in a mixing chamber that exits through the outlet as an oscillating jet. As the supplied flow passes from the inlet through the mixing chamber, it attaches to one wall of the mixing chamber before exiting through the outlet; before exiting, a small portion of the stream flows through a feedback channel back into the mixing chamber. This feedback creates a recirculating flow region that continues to grow until it forces the main stream to separate from its current side and reattach to the other side of the mixing chamber, were the process restarts. The resultant frequency can range from 10 Hz up to 20 kHz depending on the geometry, scale, and supplied flow rates. Additionally, oscillators are characterized by the angle of the exiting flow, called the jet deflection angle, which similarly varies with geometry, scale, and supplied flow rate.

Recent research has begun to investigate the use of fluidic oscillators with gases in active flow control applications. Active flow control utilizes some form of actuation to modify the behavior of a given flow field from what would naturally be produced. This actuation is commonly

used to produce a more desirable flow state, such as mitigating separation, preventing transition, or enhancing mixing. Previous work in unsteady active flow control has shown that interacting with the naturally occurring instabilities in a flow field will produced increased effectiveness or reduced amplitudes required for actuation, indicating that an improved understanding of the underlying jet oscillation frequency is important to ensure the highest gains in performance can be achieved when using active flow control.

1.1. Review of Literature

Previous work on fluidic oscillators have primarily focused on understanding the internal flow mechanics and some geometric parameters affecting the flow field. Osterman et al.[1] experimentally compared two common fluidic oscillator designs, one with rounded sides and smooth internal geometry and one with square edges and sharp corners, see Fig. 1.1. Both were found to exhibit similar internal flow mechanics; however, the sharp edges led to a greater extent of separation when compared with the round fluidic oscillators. Despite the similarities in the internal flow field, each exhibit very different external flow fields. Round oscillators generate a jet with a long dwelling time at the maximum deflection angles, which generates a higher concentration of fluid on either edge of the deflection cone. Square oscillators generate a more balanced sweeping jet through the full deflection cone and results in a more homogeneous distribution.

Wosizdlo et al.[2] and Gartlein et al.[3] examined the time-resolved flow field of a fluidic oscillator. Time resolved pressure measurements and PIV was used to characterize the internal and external flow fields of a square oscillator connected to an air supply. The underlying mechanism governing the jet's behavior, the recirculation bubble in the mixing chamber, was observed and characterized. Bobusch et al.[4] studied the internal flow behavior of a fluidic oscillator immersed in water using PIV, pressure measurements, and a hydrophone. Using water as the base fluid slowed down the oscillation behavior, making certain features easier to capture. In addition to observing the recirculation bubble, it was found that the largest external deflection occurred during the internal switching process instead of when the internal flow was attached to one side.

Bobusch et al.[5] investigated the geometric parameters that affect square fluidic oscillator properties, including the influence of outlet geometry, mixing chamber inlet geometry, outlet nozzle geometry, and feedback channel geometry. Using ANSYS CFX 14.5, this numerical study

determined that outlet geometry had no effect on internal flow characteristics and therefore no effect on oscillation frequency. An increase in the mixing chamber inlet length was found to increase the frequency due to a change in the formation of the initial circulation bubble and a faster growth of the bubble forcing the switching mechanism. Outlet nozzle variations were found to have little effect on the oscillator frequency but would lead to large changes in the jet deflection angle. Smaller outlet nozzles resulted in a larger axial velocity due to conservation of mass, causing the jet to have a smaller deflection angle but persist further downstream, while a larger outlet nozzle caused the opposite. Feedback channel geometry was investigated as one of the most important parameters, since it directly influences the feedback into the circulation bubble which forces the jet to oscillate in the mixing chamber. The channels were investigated in numerous ways, including changing the geometry to be round, changing the feedback channel length, and changing the feedback channel volume. While the feedback channels do have a significant effect on the oscillation frequency, the general trends are still not completely understood and need to be further examined.

Seo and Mittal [6] also numerically simulated the effect feedback channel length, mixing chamber, and an external grazing flow. While the feedback channel length was increased, there was no effect on the oscillator frequency, however the amplitude weakened, and the oscillation periodicity was not as coherent. Variations in the mixing chamber length showed a strong non-linear inverse relationship between the oscillator frequency and mixing chamber length. While the grazing external flow unsurprisingly made the oscillators favor one deflection side, the internal flow characteristics and resulting oscillation frequency were unaffected.

Hossian et al.[7] investigated the effect of surface roughness on several performance parameters of fluidic oscillators. Various cases were examined by adding sand paper of different grit, 60 and 100, to the top and bottom wall, as well as different surfaces of the feedback channels. It was discovered that the oscillation frequency was very sensitive to the aspect ratio of the fluidic oscillator, resulting in different frequency slopes with respect to the mass flow for each aspect ratio. Roughness was shown to reduce the jet deflection angle and increase the oscillation frequency. The roughness causes the separation bubble to “break” earlier, which increases the oscillation frequency and decreases the overall jet deflection angle. It was also determined that there are two distinct regimes in the frequency vs mass flow curves, a linear region at low mass flows and a non-linear region at high mass flows.

Previous studies have indicated that unsteady active flow control can produce benefits over a fixed constant blowing due to the excitation of naturally occurring instabilities, reducing the necessary amplitude to generate desired lift improvements. Many studies disagree, however, on the best order of magnitude of the dimensionless actuation frequency, F^+. Griffin et al.[8] used an open-loop control system to conduct flow control over a flat plat using zero-net-mass flux (ZNMF) actuators. It was demonstrated that matching the shear layer frequency would produce the largest pressure recovery from the baseline flow and reattached at smaller C_μ values than would be necessary with constant forcing. Gupta and Ansell [9] demonstrated that using closed loop control, high-energy modes could be used to inform actuation to match the shear-layer frequencies and excite vortical structures. This closed loop method to match frequencies proved to be more efficient at separation control on the trailing edge of the NLF-0414 airfoil than no actuation or a fixed actuation at $F^+ = 1$. Other studies have recommended F^+ ranging from 0.14-0.56 with a low pressure turbine blade[10] up to O(10) with a NACA symmetrical airfoil[11].

Somers and Maughmer [12,13] developed the S414 as a SNLF multi-element airfoil that would achieve a high maximum lift coefficient with an extensive portion of laminar flow across the chord during cruise. The aft element eliminates the requirement for the trailing edge of the fore element to recover to freestream pressure, which allows for favorable pressure gradients along the entire length of the fore element and large portions of the aft element. Unlike conventional aircraft with slotted flaps, the S414 has no nested configuration; the slot between the two elements is always open and the airfoil can achieve high lift without a need to deflect the aft element. However, the airfoil has an abrupt leading-edge stall that needs to be mitigated in future iterations of SNLF airfoils.

1.2. Research Motivation and Objectives

Many early studies on fluidic oscillators have focused on studying the unique internal flow features through CFD applications. While there have been some studies on the frequency behavior and jet deflection behavior of fluidic oscillators under differing inlet conditions and geometric parameters, there has not been a focus on developing tools to predict the frequency behavior of these oscillators. In this investigation, a heavy emphasis is placed on characterizing the behavior of fluidic oscillators under different conditions to develop a predictive model for the frequency behavior of fluidic oscillators.

The S414 multi-element SNLF airfoil was developed for rotorcraft with large portions of laminar flow across the chord. This airfoil system does have some unfavorable characteristics, such as a large suction peak on the fore element that leads to a sharp abrupt leading-edge stall. The S414 also serves as a stepping stone in the development of a high lift SNLF airfoil for cruise on a transonic transportation aircraft as part of a NASA-sponsored University Leadership Initiative research program. The additional focus of this study is necessitated by the fact that previous studies have not investigated the influence of unsteady active flow control on SNLF style airfoils with fixed open slots. Emphasis was placed on investigating the influence of embedded fluidic oscillators on the S414 airfoil, maximizing the airfoil lift characteristics while also trying to alleviate the large suction peak on the fore element and redistribute some of the loading to the aft element. Finally, insights on how unsteady active flow control interacts with the S414 can be applied to later SNLF designs. The primary objectives of the current investigation can be summarized by the following:

- Characterize the frequency behavior of fluidic oscillators under varying inlet conditions and geometric parameters and develop a model to predict the frequency of oscillators.
- Design a set of fluidic oscillators to be embedded in the SNLF S414 airfoil based on various constraints, i.e., F^+, C_μ, and internal airfoil geometry.
- Characterize the effectiveness of fluidic oscillators as active flow control elements for the SNLF S414 airfoil in different configurations for use in later SNLF designs.

1.3. Chapter 1 Figure

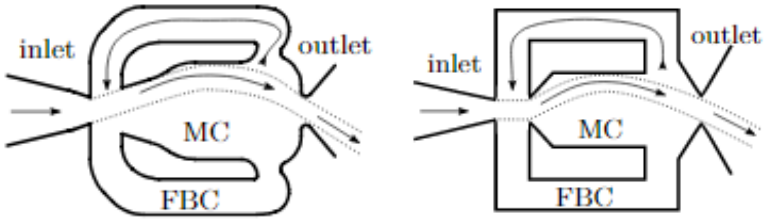

Fig. 1.1. Round and Square Fluidic Oscillator Designs.

Chapter 2: Experimental Methods

This chapter will detail the experimental methods and facilities used during the experimental study. It details the parts and manufacturing methods used, equipment used, and formulations used to evaluate the acquired results.

2.1. Testing Environment

2.1.1. Fluidic Oscillators

Two different fluidic oscillator designs were tested, a round and square version. The square fluidic oscillator is defined by squared edges in the mixing chamber and feedback channels, while the round fluidic oscillator has rounded edges in the mixing chamber and feedback channels. During this study a naming scheme was developed to identify which oscillator variation was being tested, with the round and square oscillators denoted by a -R- and -S- respectively. An initial geometry for both oscillator designs was found based on previous studies, see Fig. 1.1.

Once the baseline geometries for the two designs were created, geometric variants were also designed to determine the influence of geometric parameters on the flow frequency of the oscillators. In this study, the effect of three geometric parameters were studied, the throat length into the oscillator, the wedge length into the mixing chamber, and the outlet length. These parameters were denoted by -T-, -W-, and -O-, for the throat, wedge, and outlet respectively, see Fig. 2.1. Each of the three geometric parameters had their baseline dimension varied to produce

four other geometries, having variations of +10%, +20%, -10%, and -20%, denoted by a -1, -2, -3, and -4, respectively. The baseline geometry is denoted with a -B. Only one parameter would be varied for each geometry, the other parameters would keep their baseline length. This approach resulted in two sets of 13 oscillator variants, one for each of the round and square oscillator designs.

It is believed that the aspect ratio, defined as the outlet length divided by the oscillator thickness, $AR = l_o/t$, has a large effect on the frequency behavior of the oscillator. Each set of oscillator designs was made using three different aspect ratios corresponding to two different material thicknesses. Using plexiglass with a thickness of 6.35 mm, sets of oscillators were made with an aspect ratio of 2 and 4, denoted as S- and L-. A set of oscillators with an aspect ratio of 1 was built using plexiglass with a thickness of 12.7 mm, denoted as LT-. Including the three aspect ratios for each of the two sets of oscillators, a total of 78 individual oscillators were designed and analyzed. Using the discussed naming convention, a round oscillator with a wedge variation of +20% and an aspect ratio of 4 would be denoted as LRW2. Table 2.1 shows the baseline dimensions for the six sets of fluidic oscillators, while Table 2.2 shows the main dimensions for the small round oscillators, demonstrating the percent change in the geometric parameters.

The fluidic oscillators were built using multiple layers of plexiglass. Each oscillator design and scale had a single back that was constructed from 1-in thick aluminum. The back had a mounting plate so it could be fixed to an optics table and had threaded holes for screws to mount the fluidic oscillators in place. A second layer had the oscillator geometry, which resulted in three pieces: the main piece with the outer geometry and two floating “wedges” which would create the channels and mixing chamber. This layer was cut out of plexiglass using a laser cutter for the 6.35 mm thick material and using a water jet cutter for the 12.7 mm thick material. The final layer was cut out of plexiglass in the same fashion as the second layer and makes the front face. Holes were cut in both the second and final layer so that bolts could be used to secure the plexiglass layers to the aluminum back. A seal was maintained through the bolts holding the plexiglass layers together, however in some cases c-clamps were also used to help maintain the seal. The tolerance in the 6.35 mm plexiglass material thickness was good and did not require additional support to maintain a pneumatic seal, though the 12.7 mm thick plexiglass did have some tolerance issues, so a soft cloth was placed between the layers as needed. When the layers were tightened together, the cloth would compress, and a seal would be maintained. Fig. 2.2 shows a CAD rendering of the layers that make

up the fluidic oscillators, where the transparent parts are plexiglass and all other parts are aluminum.

2.1.2. Wing and Airfoil Configurations

This second focus of this research was how fluidic oscillators augment the lift of a slotted natural laminar flow (SNLF) airfoil. The S414 airfoil is a multi-element SNLF airfoil designed by Dan Somers with Airfoils Inc and was analyzed by Dan Somers and Mark Maughmer[12]. The S414 SNLF design is a passive natural laminar flow concept with the goal of achieving a high maximum coefficient of lift with an extensive portion of the chord in laminar flow during cruise. The addition of the aft element allows for the fore element to support favorable pressure gradients along its entire surface and therefore support laminar flow along its entire length, while the aft element supports 100% laminar flow along its lower surface and 60% laminar flow along its upper surface[13]. While this airfoil was originally designed for rotorcraft applications, analysis with this airfoil will serve as a baseline for later studies.

Additional configurations of the S414 airfoil were developed previously through an MSES analysis[14]. These additional configurations used the aft element as a deployable flap to attempt to generate higher lift than what is normally possible in the standard S414 configuration. As a result of this analysis, five additional configurations were developed with the aft element in different locations to augment the total lift of the airfoil. Case 5, documented in the other study, represents an intentionally aggressive position for the aft element, which was determined using empirical data from other cases configured in this way. In this Case 5 position the aft element is inclined by 21.0°, shifted to have a gap of 0.015 x/c and overhang of 0.025 x/c. This aggressive positioning of the aft element in Case 5 leads to a larger portion of separated flow, which creates more flow features that could benefit from flow control.

For this study, both the baseline S414 configuration and the Case 5 configuration were studied without and with fluidic oscillators applying active flow control. Case 5 will be referred to as the "high lift configuration" (HLC) in this report.

2.1.3. Wind Tunnel

All the experiments were conducted using an open-return type, subsonic wind tunnel. The tunnel has a rectangular test section, measuring 2.8 ft x 4 ft and extends 8 ft in length along the

streamwise direction. The test section was designed with a linear gradient such that the downstream end is slightly larger to accommodate for the growth of the boundary layer along the walls. A four-inch thick honeycomb flow straightener and a total of four anti-turbulence screens form the inlet section of the tunnel. This flow conditioning is effective in containing the turbulence intensity in the test section to under 0.1% at all operating speeds. The area ratio between the inlet and the upstream end of the test section was 7.5:1. A schematic of the tunnel is seen in Fig. 2.3.

A five-bladed fan installed near the end of the diffuser is powered by an ABB ACS 800 Low Voltage AC drive with a regulated 125-horsepower AC motor. The motor can achieve a maximum angular speed of approximately 1200 RPM, which corresponds to an empty section speed of approximately 165 mph (242 ft/s). The Reynolds number of a given airfoil was calculated based on the chord using,

$$Re = \frac{\rho U_\infty c}{\mu} \tag{2.1}$$

where U_∞ is equal to the free stream velocity, c is the model chord, ρ is the freestream air density, and μ is the free stream dynamic viscosity of air. During testing, the Reynolds number was kept within 0.5% of the desired value through an iterative routine and was adjusted with each angle of attack to account for variations in tunnel blockage.

The difference in static pressures (ΔP) between the inlet settling section and the test-section ($P_{ss} - P_{ts}$) was used to determine the free stream velocity in the test-section. A Setra 239 15" WC differential pressure transducer was used to measure ΔP. The settling section pressure is averaged between four taps, one on each of the four walls, just downstream of the anti-turbulence screens. Similarly, the test section pressure was averaged by four taps just upstream of the test section. Knowing the difference in static pressure along the wind tunnel inlet, ΔP, and assuming a steady, inviscid, and incompressible flow through the tunnel, the velocity in the test section can be calculated using an expression for the constant volume flow rate (Eq (2.2) in combination with Bernoulli's equation (Eq (2.3) applied at the settling section and the test section inlet. The test section velocity is then calculated through Eq 2.4.

$$A_{ss} U_{ss} = A_{ts} U_{ts} \tag{2.2}$$

$$\frac{1}{2}\rho {U_{ss}}^2 + P_{ss} = \frac{1}{2}\rho {U_{ts}}^2 + P_{ts} \tag{2.3}$$

$$U_{ts} = \sqrt{\frac{2(P_{ss} - P_{ts})}{\rho_{amb}\left(1 - \left(\frac{A_{ts}}{A_{ss}}\right)^2\right)}} \tag{2.4}$$

The term A_{ts}/A_{ss} in Eq (2.4 represents the ratio between the cross-sectional areas of the test section and the tunnel settling section, while ρ_{amb} represents the ambient air density. The ideal gas law (Eq (2.5) was used to calculate the ambient density of the room.

$$\rho_{amb} = \frac{P_{amb}}{RT_{amb}} \tag{2.5}$$

where R is the air specific ideal gas constant. The ambient pressure, P_{amb}, and ambient temperature, T_{amb}, were measured using a Setra 270 absolute pressure transducer and a National Instruments Type-J thermocouple respectively.

2.1.4. Aluminum Airfoil Model

The current study was performed using a multi-element SNLF S414 airfoil, presented in Fig. 2.4. Both elements were imported into XFOIL and then were modified to create a finite-thickness trailing edge. The trailing edge thickness on both elements was increased to 0.34% of the chord and the airfoil contour was blended along the full chord length of each element to minimize the change in the airfoil shape. This final geometry was used during the construction and manufacturing of the model for wind tunnel testing. The airfoil model was fabricated out of both aluminum and stereo-lithographically (SLA) deposited plastic, it had an 18 in chord and a 34.1 in span. The SNLF airfoil was mounted to turntables in the floor and ceiling of the wind tunnel, with an extra ¼" extrusion into these turn tables, which gives an effective test span of 33.6 in. The fore element has two spars, while the aft element has one spar, all three of which are secured to both turntables by L-brackets. The spars transfer the loads of the model to both turntables through the L-brackets and the turntables transfer the loading to the support legs of the balance.

The Fore element extends for 80% of the chord and was constructed out of seven aluminum blocks and three SLA printed components for the trailing edge. The aluminum components make up 90% of the fore element chord, while the SLA printed components slot into the aluminum components to make up the rest of the trailing edge. Heat-set inserts were installed into the SLA printed trailing edge components so that they could be screwed to the aluminum components. A total of 61 static pressure taps were distributed across the upper (30) and lower (31) surface of the fore element, with 52 on the aluminum components and 9 on the SLA printed trailing edge, see

Table 2.3. These pressure taps were used for acquiring time averaged static pressure measurements. To prevent any downstream taps from being affected by bypass transition induced by an upstream tap, the taps were displaced along the spanwise axis by 14 deg with respect to the freestream. This approach ensured that taps would be outside of the turbulent wedge formed by upstream taps and the static pressure readings would not be affected by tap-induced turbulence. The fore element has two steel spars, one at 28.5% of the chord and the other at 51.1% of the chord; the pressure tap lines were fed through the spar and out of the tunnel.

The aft element extends for 33.3% of the chord and was constructed out of seven aluminum blocks and had a 10% total chord flap, which is composed of three SLA printed components. The aluminum aft element has 27 taps divided between the upper (15) and lower (12) surface, while the SLA printed flap has 5 taps divided evenly between its surfaces, with one at the trailing edge, see Table 2.4. Like the fore element, the pressure taps on the aft element are displaced along the spanwise axis by 14 deg to be larger than the spreading angle of the turbulent wedge formed by any upstream taps. An additional 6 taps were spaced along the spanwise section at 87.3% chord with a variable separation, locations are summarized in Table 2.4. These taps were used to determine if 3D flow effects developed across the model due to interactions between the wind tunnel walls and high-lift conditions. The aft element has a single spar, at 79.2% of the chord where the pressure tap lines were fed into and out of the tunnel. Small brackets were added in the back cove of the aft element so a hollow rod could be threaded through, allowing the SLA printed flap to be attached. Taps for the flap were fed through the hollow rod to exit the tunnel. Fig. 2.5 shows the model mounted in the wind tunnel spanning from floor to ceiling.

2.1.5. SLA Printed Aft Element

An additional SLA printed aft element was made and consists of 9 components that allow for the testing of embedded fluidic oscillators in different chordwise locations. The SLA printed aft element has 30 taps divided along the upper (19) and lower (11) surfaces with a different distribution than the aluminum aft element, see Table 2.5. This new distribution was chosen to try and capture flow features, such as a laminar separation bubble[12], which would not have been captured by the previous distribution. Like the aluminum aft element, the SLA printed element has a single spar in the same position, at 87.3% chord, where the pressure tap lines were fed into and out of the tunnel. Unlike the aluminum aft element, there are no spanwise taps embedded in this

element. When testing with the SLA printed aft element, the same SLA printed flap that was previously incorporated into the aluminum aft element was also used.

The SLA aft element is composed of three spanwise sections that are slid together using a small steel ¼" rod to prevent torsion and then locked into place with screws through the steel spar. Each section is composed of three components: a main core, front surface, and top surface. The main core has a hollow cylinder that acts as a plenum to transport air through each component. While the main core component is attached to the spar, the other two components can be interchanged, allowing for parts with and without embedded fluidic oscillators to be added to the model. These two components slot into the main core and interface with the plenum that runs spanwise through the model. At each interface there are rubber o-rings of 0.354in ID to maintain the pressure seal. Heat-set inserts were installed in the various SLA printed components so that the parts could be screwed together for testing. The SLA printed aft element was tested with three oscillator configurations: (i) clean with no embedded oscillators installed, (ii) only the top surface with embedded oscillators, and (iii) only the front surface with embedded oscillators. The second and third configuration each required a different set of SLA printed components with embedded oscillators to apply spanwise actuation. In Chapter 2:, the (ii) configuration is referred to as the upper surface oscillators and ejects at 80% chord, while the (iii) configuration is referred to as the leading edge oscillators and ejects at 70% chord. Each configuration had 28 evenly spaced oscillators embedded, each with an outlet slot 0.0625 in wide by 0.075 in long, see Fig. 2.6. Section 2.6 details the control of the embedded oscillators in the SLA printed aft element.

2.1.6. Oscillator Pressure Supply

The fluidic oscillators embedded in the airfoil are part of a closed loop control system. The air was supplied by a tank farm, which maintains an air pressure of approximately 700 kPa (101 psi) and was stepped down to the desired pressure using a pressure regulator. The pressure regulator was a SMC ITV3050-31NCL 4, which operates on an input of 0-5 V and correlates this to a percentage of the input pressure, up to 100%, however the regulator can only output up to 130 PSI. After the pressure regulator, the air goes through a mass flow meter, Omega Model FMA-1613A. Air temperature, pressure, volume flow, and mass flow are all measured by the mass flow meter. The mass flow meter is rated for up to 1000 SLPM, but can measure slightly higher, up to 1250 SLPM.

A closed loop control system was designed to control the mass flow through the oscillators, in either the embedded airfoil system or the individual oscillators. The pressure regulator was connected to the computer through a NIDaq 6009 board and was powered by a DC power supply, while the mass flow meter was connected through a serial port to the computer. A desired value, either gauge pressure or mass flow, was input and an initial value was given to the pressure regulator. The current flow conditions were recorded by the mass flow meter and the computer compared the desired flow condition with the current condition. An updated voltage setting was sent through the NIDaq board to the pressure regulator. This loop continued until the desired condition met a certain threshold; within 172 Pa (0.025 psi) of the desired gauge pressure for the geometric frequency evaluation, or within 0.5% of the desired C_μ for wind tunnel testing. During the geometric parameterization analysis, the pressure of the flow into the oscillator was set once at the beginning for each geometry, while the C_μ was checked and updated at each angle of attack during the polar sweep in the wind tunnel due to changing flow conditions. Fig. 2.7 shows a flow chart detailing the routine for controlling the oscillator pressure. Section 2.6 details more on the parameters considered during wind tunnel testing, such as C_μ.

2.1.7. Tunnel Suction System

Due to the large pressure gradients generated by the S414 airfoil, the boundary layer can be pulled off the sides of the wind tunnel, introducing 3D effects into the data and resulting in artificial reductions in airfoil lift and increases in drag measurements. In order to counter this affect, a heavy-duty suction system combined with porous turntables was installed on the top and bottom of the tunnel, where the airfoil was mounted into the walls. This suction system was designed to reduce the boundary layer growth in the test section and limit the separation of the boundary layer off the tunnel walls during testing.

Based on previous studies, suction is most effective up to approximately 0.4% of the total mass flow in the tunnel test section, beyond this value there is limited gain in airfoil performance[15]. As an added factor of safety, the target percent mass flow was chosen to be 0.45%, which requires a mass flow of 10.49 ft^3/s or 630 cubic feet per minute (CFM). Accounting for pressure losses in the ducting or potential leakages that could develop in the system, a mass flow of 700 CFM became the design target.

In order to accomplish this a motor and positive displacement blower (PDB) system was designed to attach to the walls of the tunnel. The positive displacement blower is a Grainger-

Speedaire 2EPR9, it can apply a max vacuum of 7 psia, runs at 2.6 to 33.1 HP, operates at 764 – 2850 RPM, moves 388 to 953 CFM, and displaces 0.35 CF/revolution. The motor is a Dayton 2MXW3, has a nameplate 3550 RPM, operates at 208-230/460 V, 58/29 Amps, and 60 Hz. A WolfAutomation LSIS-LSLV0185H100-2Conn voltage frequency drive (VFD) was used to control the motor and PDB system, which is a 3 phase AC VFD that can operate a 25 HP motor from 200-240 V, up to 70 Amp.

In order to reach the target CFM of 700, the PDB needs to operate at 2000 RPM and requires 19.4 HP. To reach the desired HP, the VFD operates at 77.8% maximum power to provide 45 Amps at 46.7 Hz; at this value, a pulley ratio of 0.724 is needed to reduce the RPM of the motor to the required RPM for the PDB. This pulley reduction was accomplished using two v-belt systems chained together, one combining a 6.5" and 7.5" pulley to produce a pulley ratio of 0.867 and the second combining a pulley of 3.95" and 4.75" to achieve a pulley ratio of 0.832 for a composite ratio of 0.721. Each pulley had two belt grooves, so 4 type A v-belts were used to transfer power from the motor to the displacement blower. The motor, PDB, and VFD were all assembled onto a steel pallet that was welded together and then the pulley system was covered in a plywood box for safety. Fig. 2.8 shows the suction system on the pallet with the pulleys, while Fig. 2.9 shows the system with the safety cover over it.

The porous pattern on the turn table was designed based on previous studies[16]. Two small portions on the wall were designed with a porous section. This includes a section that follows the curvature of the turntable upwind of the airfoil, from just above the top surface to far below the bottom surface, and a section that follows the upper surface of the airfoil and then the curvature of the aft element past the trailing edge. These sections were designed with a 10% porosity using holes with a 0.2" diameter. Fig. 2.10 shows the CAD model of one of the turntables illustrating the porous section as well as the insert for the airfoil; this design is repeated on the other turntable as well. Plenum boxes were designed to follow the contour of the porous sections; they are two inches deep and constructed with ½" plywood, screws, liquid nails, and lined with a foam tape to help maintain pressure. The boxes are connected to 10' long sections of 4" flexible tubing which is connected to the PDB by 4" PVC pipe, see Fig. 2.11.

2.2. Oscillator Model Development

A multivariate linear regression (MVR) model was used as the basis for developing a model to predict oscillator frequencies for a given geometry. A popular representation of the model relates a y-variable to $p-1$ x-variables, where p is the number of coefficients, β_j.

$$y_i = \beta_0 + \beta_1 x_{i,1} + \beta_2 x_{i,2} + \cdots + \beta_{p-1} x_{i,p-1} + \epsilon_i \tag{2.6}$$

where β_j represents the population coefficients and will be represented as an estimate of the coefficient, b_j. The residual error, ϵ_i, is calculated as the difference between the actual and predicted values of y, $y_i - \hat{y}_i$. The predicted values, $\hat{y}_i$, are calculated using the estimated coefficients.

$$\hat{y}_i = b_0 + b_1 x_{i,1} + b_2 x_{i,2} + \cdots + b_{p-1} x_{i,p-1} \tag{2.7}$$

The coefficient values are calculated by creating a matrix of the resultant values, Y, and columns of each variable of interest with a column of 1's in front such that $X = [1\ x_i]$. This column of 1's allows for the constant coefficient or intercept, b_0, to be calculated. Coefficient estimates are then calculated using the following method.

$$b = (X'X)^{-1}X'Y \tag{2.8}$$

When determining the accuracy of a model, R^2 is generally used to represent how well the data can be "explained" by the linear regression model predictions. As more variables are added, R^2 will always increase or remain the same, even if the variables are unrelated to the resulting data. On its own, R^2 is not a good predictor of the accuracy of the model. However, an alternative adjusted R^2 can be calculated, which will not increase if a variable is not a good fit for the model.

$${R^2}_{adj} = 1 - \left(\frac{n-1}{n-p}\right)(1 - R^2) \tag{2.9}$$

In order to determine if a variable is a useful predictor in a model, a significance test is performed. The assessment is done by performing a t-test for the null hypothesis, $H_0: b_i = 0$. If the null hypothesis is correct, then a change in the given variable will not yield a significant change in the resulting variable, y_i. The t-statistic was calculated using the following: $t^* = b_i / se(b_i)$, where $se(b_i)$ is the standard error of the given coefficient.

A stepwise regression procedure was used to develop the model relating the frequency to the geometric parameters of the fluidic oscillator. The procedure involves first setting alpha-to-entry, α_E and alpha-to-remove, α_R values. These values are prescribed as the necessary significance levels to include or remove a variable while building the model. During the

development of this model, both significance levels were set to the same value, $\alpha_E = \alpha_R = 0.05$. The procedure is started by regressing each individual variable of interest with the resultant value, y, and recording the resultant b, t^*, and $p - value$. Any variable with a $p - value$ greater than α_E is removed as an option for the model. The variable with the smallest $p - value$ or the largest t^* is chosen as the first variable and noted. Each variable that is not removed is then regressed individually with both the resultant value, y, and the first variable of significance, which results in multiple two-variable models. Of the new regressions, the model with the lowest $p - value$ that is below the α_E now becomes a part of the model. However, it must be checked to see if the inclusion of a new variable reduces the significance of any of the previously included variables. Therefore another $t^* - test$ is performed to determine the significance of the previously included variables with the newly included variable. If the resulting $p - value$ is greater than the alpha-to-remove, α_R, then the previous variable is removed, and the model only includes the new variables. This process is repeated until there are either no more variables to add to the model or the remaining variables have resulting $p - values$ that are above the α_E. All variables in the model at the end of this process make up the resultant regression model. A non-linear regression model can also be developed using the same methods and equations, before starting to calculate any coefficients, a non-linear equation would be applied to any variable of interest, such as squaring them or taking the natural log.

2.3. Time averaged pressure measurements

Two major classes of time-averaged pressure measurements were used over the course of this study, including static pressure measurements over the airfoil surface and total pressure measurements in the wake of the airfoil. Miniature electronic differential pressure measurement units, ESP-32HD manufactured models by Esterline, Inc, were used to acquire all time averaged pressure measurements. These scanners use an array of silicon piezo-resistive sensors connected in a Wheatstone bridge configuration to generate a voltage that is proportional to the pressure inputs. A Digital Temperature Compensation (DTC) Initium Data Acquisition System is used to acquire the output voltages from these sensors. Pressure tubes connect the static pressure taps on the surface of the airfoil or total pressure probes on the wake rake to the 32 ports on each of the ESP scanning modules use in tise investigation.

Five ESP-32HD scanners were used during the current study. Total pressure probes in the wake rake connected to two ±0.35 psid (10 in. WC) ESP scanners. Pressure taps across regions of

the expected highest pressure differentials were connected to a ±5.0 psid ESP scanner, namely the leading edge of both the fore and aft elements. Two ±1.0 psid ESP scanners were used for the remaining static pressure taps on the airfoil. Measurements were taken at a sample rate of 50 Hz and averaged over two seconds. The static pressure inside the tunnel test section was used as the zero-reference for all static pressure measurements on the airfoil surface. Ambient pressure in the test facility was used as the zero-reference for all total pressure measurements for the airfoil wake. Applying a momentary pulse of control pressure allows for the ESP scanners to be switched between run and calibrate modes. In calibration mode, the zero-load voltage is redefined for each channel. A 6th order, temperature-compensated calibration curve is provided by the DTC Initium system for each port to convert the recorded voltages to pressure measurements.

2.3.1. Airfoil Performance Coefficients

One of the ports in the pressure scanner was also reserved for measuring ($P_{ss} - P_{ts}$) in order to calculate the velocity and dynamic pressure of the freestream flow with a higher accuracy than that of the Setra 239 pressure transducer, as outlined in section 2.1.2. Setting the tunnel speed for a desired Reynolds number was the only use of the measurements from the Setra 239 transducer.

Pressure coefficients along the airfoil surface were found by taking static pressure measurements for the airfoil model and non-dimensionalizing them with respect to the freestream dynamic pressure, based on the measurements form the ESP pressure scanners. Dynamic pressure of the freestream flow (q_∞) was calculated using,

$$q_\infty = \frac{1}{2}\rho_\infty {U_\infty}^2 \tag{2.10}$$

Using Eq (2.4 , Eq (2.10 can be rewritten as a function of the tunnel contraction ratio,

$$q_\infty = \frac{1}{2}\rho_\infty {U_\infty}^2 = \frac{P_{ss} - P_{ts}}{1 - \left(\frac{A_{ts}}{A_{ss}}\right)^2} \tag{2.11}$$

The flow through the wind tunnel was assumed to be incompressible ($M_\infty \leq 0.3$), such that the ambient density (ρ_{amb}) is assumed to be equal to the density of the freestream air (ρ_∞). The pressure coefficient on the airfoil at any given location was calculated using,

$$C_p = \frac{P_s - P_\infty}{q_\infty} \tag{2.12}$$

A constant freestream dynamic pressure q_∞ was assumed between the test section inlet, where the test section static pressure (P_{ts}) was measured, and the upstream region of the airfoil model. The test section effective cross-sectional area could be assumed constant at the location of the airfoil since the boundary layer growth was accounted for in the design of the tunnel. As a result, the static pressure measured at the test section inlet could be assumed to be the same static pressure encountered by the airfoil model.

The collected static pressure distribution over the surface of the airfoil was used to calculate the airfoil lift and pitching moment coefficients by approximating the contours of the airfoil as a series of panels. Linear geometric interpolation between each adjacent tap on the surface was used to generate a total of (n-1) panels for (n) number of taps. The pressure across the length of a panel was assumed to be the average of the two pressures on either end of the panel. Forces due to the pressure distribution acting in the normal direction to the panels was split into chord-normal and chord-axial components. Using the known panel orientation with respect to the airfoil chord line, geometric transformations were used to extract the chord-normal and chord-axial components. Pressure coefficients were calculated from the pressures at each panel and used to calculate the chord-normal and chord-axial force components as coefficients acting on each panel. The sectional force coefficients acting on the panels were summed to calculate the net chord-normal and chord-axial force coefficient acting on the spanwise section of the airfoil. The net force coefficients were calculated using,

$$C_{n,j} = \sum \frac{C_{P_{l,i+1}} + C_{P_{l,i}}}{2}(x_{l,i+1} - x_{l,i}) - \sum \frac{C_{P_{u,i+1}} + C_{P_{u,i}}}{2}(x_{u,i+1} - x_{u,i}) \tag{2.13}$$

$$C_{a,j} = \sum \frac{C_{P_{u,i+1}} + C_{P_{u,i}}}{2}(y_{u,i+1} - y_{u,i}) - \sum \frac{C_{P_{l,i+1}} + C_{P_{l,i}}}{2}(y_{l,i+1} - y_{l,i}) \tag{2.14}$$

here u and l represent the upper and lower surface of the airfoil respectively and j refers to which of the two elements the coefficient is being calculated. In these equations, the x and y components have been normalized by the airfoil chord. This process was repeated for both the fore and aft elements and then summed together for the total chord-normal and chord-axial forces using,

$$C_n = C_{n,1} + C_{n,2} \tag{2.15}$$

$$C_a = C_{a,1} + C_{a,2} \tag{2.16}$$

Airfoil sectional lift coefficient was calculated using the chord-normal and chord-axial sectional force coefficients,

$$C_l = C_n \cos(\alpha) - C_a \sin(\alpha) \tag{2.17}$$

The sectional pitching moment coefficient about the leading edge of the airfoil due to the sectional forces across a given panel was calculated using,

$$\begin{aligned} C_{m_{LE},j} = & \sum \frac{C_{P_{u,i+1}} + C_{P_{u,i}}}{2} \left(y_{u,i+1} - y_{u,i}\right) \frac{(y_{u,i+1} + y_{u,i})}{2} \\ & - \sum \frac{C_{P_{l,i+1}} + C_{P_{l,i}}}{2} \left(y_{l,i+1} - y_{l,i}\right) \frac{\left(y_{l,i+1} + y_{l,i}\right)}{2} \\ & + \sum \frac{C_{P_{u,i+1}} + C_{P_{u,i}}}{2} (x_{u,i+1} - x_{u,i}) \frac{(x_{u,i+1} + x_{u,i})}{2} \\ & - \sum \frac{C_{P_{l,i+1}} + C_{P_{l,i}}}{2} (x_{l,i+1} - x_{l,i}) \frac{(x_{l,i+1} + x_{l,i})}{2} \end{aligned} \tag{2.18}$$

Like the sectional chord-normal and chord-axial forces, the leading-edge pitching moment coefficient was calculated for each element with respect to the airfoil system leading edge and then summed using,

$$C_{m_{LE}} = C_{m_{LE},1} + C_{m_{LE},2} \tag{2.19}$$

Once the leading-edge pitching moment coefficient was calculated, it was used to calculate the quarter-chord pitching moment coefficient using,

$$C_{m_{c/4}} = C_{m_{LE}} + \frac{1}{4} C_l \tag{2.20}$$

This process was used to calculate the aerodynamic coefficients for the entire S414 airfoil system.

2.3.2. Drag Calculations from Wake Pressures

Since surface pressure measurements would only contribute to a portion of the total airfoil drag, namely pressure drag, a wake survey system was used to calculate the airfoil drag with a momentum-deficit approach. A two-axis traverse system and a traversable wake rake make up the wake survey system. A total of 59 total pressure probes, each with an outer diameter of 0.04", were aligned horizontally along the wake. In order to acquire the total pressure profile of the airfoil wake downstream of the airfoil, the wake rake was suspended from the ceiling of the test section using the support structure shown in Fig. 2.12. The wake profile was captured on a plane approximately 1.2 chord lengths downstream of the trailing edge. Through an automated process in a LabView computer routine, the rake traverses across the plane until it captures both wake tails. Wake tails are found by comparing the gradient of the total pressure deficit in multiple locations along the span until a certain threshold is met, indicating a tail.

A momentum deficit method, as described by Jones[17] and Schlichting[18], was used to calculate the drag of the airfoil. A sufficiently large control volume is assumed around the airfoil model with the exit sufficiently downstream such that the freestream static pressure (P_∞) and the static pressure in the wake at the exit plane (P_w) can be considered equal. The wake velocity deficit, due to viscous effects, is attributed to creating a lower total pressure in the wake than that in the freestream total pressure. The drag of a given spanwise section of an airfoil model can be calculated using the integral form of the conservation of momentum,

$$D' = \rho \int u_w(U_\infty - u_w)dy \tag{2.21}$$

The flow velocities can be rewritten in terms of the static and total pressures (within the incompressibility limit),

$$P_\infty + \frac{1}{2}\rho U_\infty^2 = P_{0,\infty} \tag{2.22}$$

$$P_\infty + \frac{1}{2}\rho u_w^2 = P_{0,w} \tag{2.23}$$

The static and total pressure from Eq (2.22 and (2.23 are rewritten for the flow velocities and substituted into Eq (2.21. The resulting drag equation is found,

$$D' = 2\int \sqrt{P_{0,w} - P_\infty}\left(\sqrt{P_{0,\infty} - P_\infty} - \sqrt{P_{0,w} - P_\infty}\right)dy \tag{2.24}$$

The wake total pressure, freestream total pressure, and freestream dynamic pressure can explicitly express the dynamic pressure at the wake plane using,

$$q_w = q_\infty - (P_{0,\infty} - P_{0,w}) \tag{2.25}$$

Combining Eq (2.24 and (2.25, the airfoil sectional drag can be found using the wake total pressure deficit,

$$D' = 2\int \sqrt{q_\infty - (P_{0,\infty} - P_{0,w})}\left(\sqrt{q_\infty} - \sqrt{q_\infty - (P_{0,\infty} - P_{0,w})}\right)dy \tag{2.26}$$

Since the difference between the freestream total pressure and the wake total pressure could be directly measured, this expression is simpler than the corresponding sectional drag equation in Eq (2.24. To improve repeatability of the drag measurements, the ESP scanners reference the stable atmospheric pressure in the control room when acquiring the wake pressures. Gauge pressure measurements of the freestream total pressure, ($P_{o,\infty} - P_{atm}$) were obtained in the potential flow region outside of the airfoil wake, while gauge pressure measurements of the wake total pressure,

$(P_{0,w} - P_{atm})$ were obtained in the wake of the airfoil. The pressure deficit could now be calculated using,

$$P_{0,\infty} - P_{0,w} = \left(P_{0,\infty} - P_{atm}\right) - (P_{0,w} - P_{atm}) \tag{2.27}$$

The sectional drag of the airfoil was calculated through numerical integrating Eq (2.26 by the trapezoid method using the wake total pressure deficit given in Eq (2.27. The airfoil sectional drag was calculated using,

$$\begin{aligned} D' = \sum_{i=1}^{n_{rake}-1} \Bigg[& \sqrt{q_\infty - \left(P_{0,\infty} - P_{0,w_i}\right)} \left(\sqrt{q_\infty} - \sqrt{q_\infty - \left(P_{0,\infty} - P_{0,w_i}\right)} \right) \\ & + \sqrt{q_\infty - \left(P_{0,\infty} - P_{0,w_{i+1}}\right)} \left(\sqrt{q_\infty} - \sqrt{q_\infty - \left(P_{0,\infty} - P_{0,w_{i+1}}\right)} \right) \Bigg] * (y_i \\ & - y_{i+1}) \end{aligned} \tag{2.28}$$

here n_{rake} represents the total number of probes that were used to measure the wake total pressure. While the flow around a model extending from floor to ceiling would generally be associated with non-zero spanwise variations, due to manufacturing imperfections and seams between parts, this may not be true. The sectional drag was therefore calculated over several spanwise stations and then averaged to provide a spanwise invariant estimate of the sectional drag that would be characteristic of an infinite span airfoil model. Using the drag from Eq (2.28, the drag coefficient was calculated using,

$$C_d = \frac{D'}{q_\infty c} \tag{2.29}$$

2.4. Hot Film Measurements

In order to characterize the passive oscillation frequency of each geometric variation, a set of unsteady velocity measurements were acquired across the oscillator jet. The measurements were acquired with a TSI Model 1201 hot-film probe with an IFA-100 anemometer. Calibrations for the hot-film probe were produced using an empty 15”x15” wind tunnel under a noted air temperature and humidity. Hot-film data were collected along the centerline position and 50° from the centerline at a fixed radial distance from the outlet center of 1.52 cm and 3.04 cm for the small and large oscillators, respectively. Previous studies have shown that the external flow field of fluidic oscillators can have a varying sweep angle, up to 70°, so a position of 50° from the centerline was chosen to capture data close to the edge of the jet sweep. Data were collected for 15 seconds at a

frequency of 47 kHz. Voltage data from the hot-film probe ranged from 0 to 5 Volts and was converted to velocity readings using a 5th-order polynomial that was found using calibration data,

$$U = 1.02642v^4 - 8.45347v^3 + 28.9571v^2 - 39.6439v + 18.191 \quad (2.30)$$

here U is the calculated velocity and v is the voltage from the hot-film probe. The calibration curve was found by mounting the probe in the wind tunnel and recording known velocities with the recorded voltages, then building a curve fit model.

The probe was mounted to a system of two traverses for positioning. One traverse was mounted vertically, while the other was mounted horizontally with an aluminum arm to hold the probe support above the outlet of the oscillator. The hot film probe was mounted into the probe support, so the film was perpendicular to the oscillator walls and spanned across the outlet. The probe was mounted 6.6 cm from the support arm to minimize the potential disruption of the flow field from the support. Fig. 2.13 shows the hot-film probe mounted over the small oscillator to collect data.

Once the data was collected a Fast Fourier Transform (FFT) was applied to the unsteady velocity data to generate a power spectral density (PSD) and determine the passive frequency of the jet oscillations. Voltage data had the mean value of the signal removed and then was separated into either 15 or 20 ensembles of data for either the round or square oscillator designs, respectively. A Hamming window was used to isolate each segment of data and then an FFT was performed on the corresponding segment. A single-sided spectrum (DFT) was extracted from the data and the PSD was calculated, then root mean square (RMS) averaging of the PSD across the full ensemble of data was performed. Using the power spectra, the peak fundamental frequency was identified for each flow condition of each oscillator.

$$Y(k) = \sum_{j=1}^{n} X(j) W_n^{(j-1)(k-1)} \quad (2.31)$$

$$W_n = e^{(-2\pi i)/n} \quad (2.32)$$

$$PSD = \frac{1}{f_s * \frac{N_s}{N_{esb}}} * |DFT|^2 \quad (2.33)$$

$$DFT = Y(0{:}\frac{n}{2} + 1) \quad (2.34)$$

Where $X(j)$ is the sample voltage, N_s is the number of samples, N_{esb} is the number of realizations in the data ensembles, and n is the number of samples in each realization (N_s/N_{esb}).

Hot film data collected along the centerline generally resulted in a frequency that was double that which was collected at 50° from the centerline. This occurred since the jet would sweep along the centerline twice each oscillation cycle. For this study, only the frequencies corresponding to the measurements at 50° from the centerline were used during the creation of a predictive model.

2.5. Wind Tunnel Corrections

In order to simulate the flow around an airfoil in a spatially unbounded freestream, a wind tunnel testing environment is used. However, this design is infeasible due to the constraints of finite wall boundaries in the wind tunnel, which introduce wall effects and boundary layers that would be absent in the hypothetical unbounded freestream. Using standard correction procedures following the work of Barlow et al.[19] for 2D, low-Reynolds number wind testing, three major tunnel wall effects were compensated for in the acquired data. These corrections include solid blockage, wake blockage, and streamline curvature; the validity of which is dependent on the assumption of steady, incompressible flow.

An effective reduction in the test-section cross-sectional area due to model thickness and the angle of attack is called the solid blockage effect. This affect creates local flow accelerations and can be corrected for using a solid-blockage velocity increment factor, ε_{sb}. This was calculated using,

$$\varepsilon_{sb} = \frac{K_l V_m}{C^{3/2}} \tag{2.35}$$

where K_l is a constant parameter based on the airfoil configuration ($K_l = 0.52$ for airfoil models spanning the entire test section), C is the empty test-section area, and V_m is the estimated airfoil model volume. The estimated volume flow was found using,

$$V_m = \frac{3}{4} tcb \tag{2.36}$$

such that t and b are the dimensional thickness and span of the airfoil model.

A local region of increased streamwise velocity develops across the potential flow regions outside the wake of the airfoil to account for the region of velocity deficit and ensure a constant mass flux across any given cross-sectional plane in the wind tunnel. Since the profile drag of the airfoil is directly related to the wake velocity deficit, a correlation can be made with the local flow acceleration around the wake region. A wake blockage velocity increment factor was calculated using,

$$\varepsilon_{wb} = \frac{1}{2}\frac{c}{h}C_{d,u} \tag{2.37}$$

to account for the influence of the wake blockage effect. In Eq (2.37, h and $C_{d,u}$ are the test section height and uncorrected airfoil drag coefficient respectively. By combining the solid and wake blockage increment factors, a net velocity increment can be calculated,

$$\varepsilon = \varepsilon_{sb} + \varepsilon_{wb} \tag{2.38}$$

Finite wall boundaries also constraint streamline curvature, which would otherwise be unaffected in an unbounded flowfield. The lift and magnitude of the quarter-chord pitching moment artificially increases due to an increase in the apparent camber of the airfoil due to curvature effects. An empirically derived variable, σ, is calculated to compensate for the streamline curvature effect using,

$$\sigma = \frac{\pi^2}{48}\left(\frac{c}{h}\right)^2 \tag{2.39}$$

Using the calculated factors, the airfoil angle of attack, pressure coefficient, lift coefficient, drag coefficient, and quarter-chord pitching moment coefficient were corrected. These corrected performance coefficients and airfoil angle of attack were calculated using,

$$\alpha_{cor} = \alpha_u + \frac{57.3\sigma}{2\pi}\left(C_{l,u} + 4C_{m,u}\right) \tag{2.40}$$

$$C_{l,cor} = C_{l,u}(1 - \sigma - 2\varepsilon) \tag{2.41}$$

$$C_{d,cor} = C_{d,u}(1 - 3\varepsilon_{sb} - 2\varepsilon_{wb}) \tag{2.42}$$

$$C_{m,cor} = C_{m,u}(1 - 2\varepsilon) + \frac{1}{4}\sigma C_{l,u} \tag{2.43}$$

$$C_{p,cor} = \frac{C_{p,u}}{(1+\varepsilon)^2} \tag{2.44}$$

2.6. Flow Control Parameters

When using active unsteady flow control, there are generally two major control parameters, the non-dimensional actuation frequency, F^+, and the non-dimensional jet momentum coefficient, C_μ. In this study, only one length scale was used in the evaluation of the non-dimensional actuation frequency, the chord-wise normal height from the top of the aft element flap to its trailing edge, see Fig. 2.14. While the chord length is commonly used as the characteristic length, this length was preferred to better reflect the length scale of shear-layer vortices that are being targeted by the fluidic oscillator actuation frequency. The dimensionless frequency was calculated using,

$$F^{+} = \frac{f l_c}{U_\infty} \tag{2.45}$$

where l_c is the characteristic length and was calculated using,

$$l_c = c_f \sin(\alpha_m + \alpha_f + \theta) \tag{2.46}$$

where c_f is the chord length of the 10% flap, α_m is the model angle of attack, α_f is the deflection angle of the flap, and θ is the calculated angle from the top of the flap to the trailing edge when in its zero-deflection position.

For this present study, the C_μ is calculated as a ratio between the average jet velocity from the outlet of the fluidic oscillators to the momentum in the freestream air moving past the airfoil. Flow parameters used for the fluidic oscillator jet were measured from the mass flow meter and based on a combined area of all the oscillator slots,

$$C_\mu = \frac{2n}{cbtl_o}\left(\frac{\dot{m}_{jet}}{\rho U_\infty}\right)^2 \tag{2.47}$$

In Eq. (2.47, $\dot{m}_{jet}$ is the mass flow rate through an individual oscillator, l_o and t are the oscillator outlet length and outlet thickness respectively, ρ is the local density at the outlet, and n is the number of oscillators. The mass flow for an individual oscillator was found by assuming the mass flow measured by the mass flow meter going into the plenum system would be equally split among all embedded oscillators.

Due to the behavior of the fluidic oscillators, the mass flow and resulting oscillation frequency is linearly related and is intrinsically reliant on the geometry of the oscillator. Part of the motivation behind this research was to develop a model, as detailed in section 2.2 to predict the frequency behavior of a fluidic oscillator based on certain geometric values. As a result, the non-dimensional frequency and non-dimensional jet momentum coefficient are also linearly related and have a fixed relationship depending on the geometry of the oscillator. While these parameters could not be individually varied, a model was developed to predict frequency behavior of the fluidic oscillators and was used to assist in the design of the oscillators embedded in the SLA printed aft element for the testing of the S414 airfoil. Development of the model and its application are detailed in section 3.2.

2.7. Chapter 2 Tables

Table 2.1 Dimensions of the baseline geometries for all 6 sets of fluidic oscillators.

Oscillator Designation	Thickness (mm)	Throat (mm)	Outlet (mm)	Wedge (mm)
SR (Small Round)	3.18	5.81	6.35	10.23
LR (Large Round)	3.18	11.62	12.70	20.46
LTR (Large Thick Round)	12.70	11.62	12.70	20.46
SS (Small Square)	3.18	4.45	6.35	4.45
LS (Large Square)	3.18	8.89	12.70	8.89
LTS (Large Thick Square)	12.70	8.89	12.70	8.89

Table 2.2 Dimensions of the small round (SR) fluidic oscillators and the naming convention for the geometric changes.

Name	% Change	Height (mm)	Throat (mm)	Outlet (mm)	Wedge (mm)
Baseline	**0%**	**3.175**	**5.81**	**6.35**	**10.23**
T1	+10%	3.175	6.39	6.35	10.23
T2	+20%	3.175	6.97	6.35	10.23
T3	-10%	3.175	5.23	6.35	10.23
T4	-20%	3.175	4.65	6.35	10.23
O1	+10%	3.175	5.81	6.99	10.23
O2	+20%	3.175	5.81	7.62	10.23
O3	-10%	3.175	5.81	5.72	10.23
O4	-20%	3.175	5.81	5.08	10.23
W1	+10%	3.175	5.81	6.35	11.25
W2	+20%	3.175	5.81	6.35	12.27
W3	-10%	3.175	5.81	6.35	9.21
W4	-20%	3.175	5.81	6.35	8.18

Table 2.3 Coordinates for the taps on the aluminum fore element

Upper Surface			Lower surface		
x/c	y/c	z/b	x/c	y/c	z/b
0.000		0.607	0.000		0.607
0.002		0.606	0.001		0.393
0.005		0.606	0.006		0.394
0.011		0.605	0.011		0.395
0.018		0.604	0.021		0.396
0.028		0.603	0.031		0.397
0.038		0.602	0.041		0.399
0.048		0.600	0.066		0.402
0.073		0.597	0.091		0.405
0.098		0.594	0.116		0.409
0.123		0.590	0.166		0.416
0.148		0.587	0.241		0.426
0.186		0.582	0.316		0.436
0.242		0.574	0.391		0.446
0.298		0.567	0.466		0.456
0.348		0.560	0.528		0.464
0.414		0.551	0.558		0.468
0.483		0.542	0.591		0.472
0.546		0.534	0.616		0.476
0.583		0.529	0.626		0.477
0.612		0.525	0.636		0.478
0.634		0.522	0.646		0.480
0.653		0.519	0.656		0.481
0.669		0.517	0.666		0.482
0.683		0.515	0.676		0.484
0.693		0.514	0.686		0.485
0.713		0.579	0.696		0.486
0.723		0.580	0.706		0.602
0.733		0.580	0.716		0.599
0.799		0.586	0.726		0.596
			0.736		0.594
			0.799		0.586

Table 2.4 Coordinates for the taps on the aluminum aft element including the spanwise taps

Upper Surface			Lower surface			Spanwise		
x/c	y/c	z/b	x/c	y/c	z/b	x/c	y/c	z/b
0.667		0.455	0.667		0.455	0.873		0.963
0.669		0.544	0.673		0.456	0.873		0.877
0.672		0.544	0.680		0.457	0.873		0.746
0.676		0.543	0.690		0.459	0.873		0.517
0.683		0.542	0.710		0.461	0.873		0.254
0.693		0.541	0.730		0.464	0.873		0.123
0.718		0.538	0.755		0.467	0.873		0.037
0.743		0.534	0.790		0.472			
0.773		0.530	0.830		0.477			
0.803		0.526	0.870		0.483			
0.838		0.522	0.921		0.489			
0.873		0.517	0.956		0.494			
0.927		0.509	1.000		0.500			
0.962		0.505						
1.000		0.500						

Table 2.5 Coordinates for the taps on the SLA printed aft element

Upper Surface			Lower surface		
x/c	y/c	z/b	x/c	y/c	z/b
0.667		0.544	0.667		0.544
0.669		0.544	0.674		0.456
0.671		0.544	0.684		0.458
0.675		0.543	0.694		0.459
0.680		0.543	0.709		0.461
0.696		0.541	0.724		0.463
0.719		0.538	0.765		0.469
0.747		0.534	0.810		0.475
0.779		0.530	0.857		0.481
0.812		0.525	0.921		0.489
0.847		0.520	0.956		0.494
0.865		0.518	1.000		0.500
0.874		0.517			
0.882		0.516			
0.890		0.513			
0.927		0.510			
0.962		0.505			
1.000		0.500			

2.8. Chapter 2 Figures

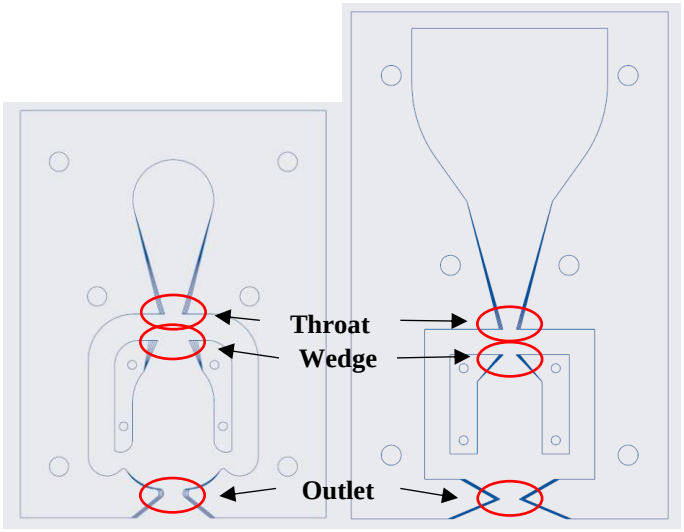

Fig. 2.1. Round and Square Oscillators highlighting the inlet, wedge, and outlet geometries that were varied.

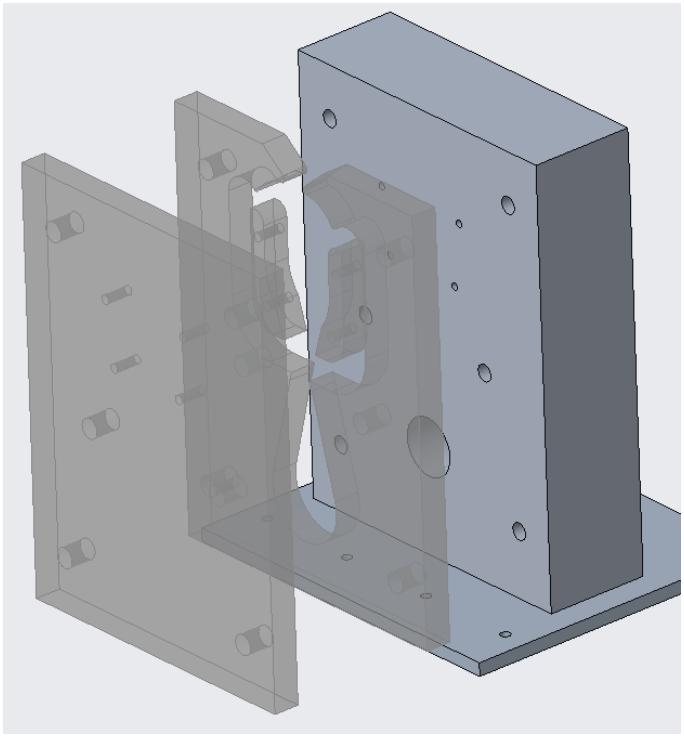

Fig. 2.2. CAD Rendering of the individual oscillator geometry; transparent parts are plexiglass, while all others are aluminum.

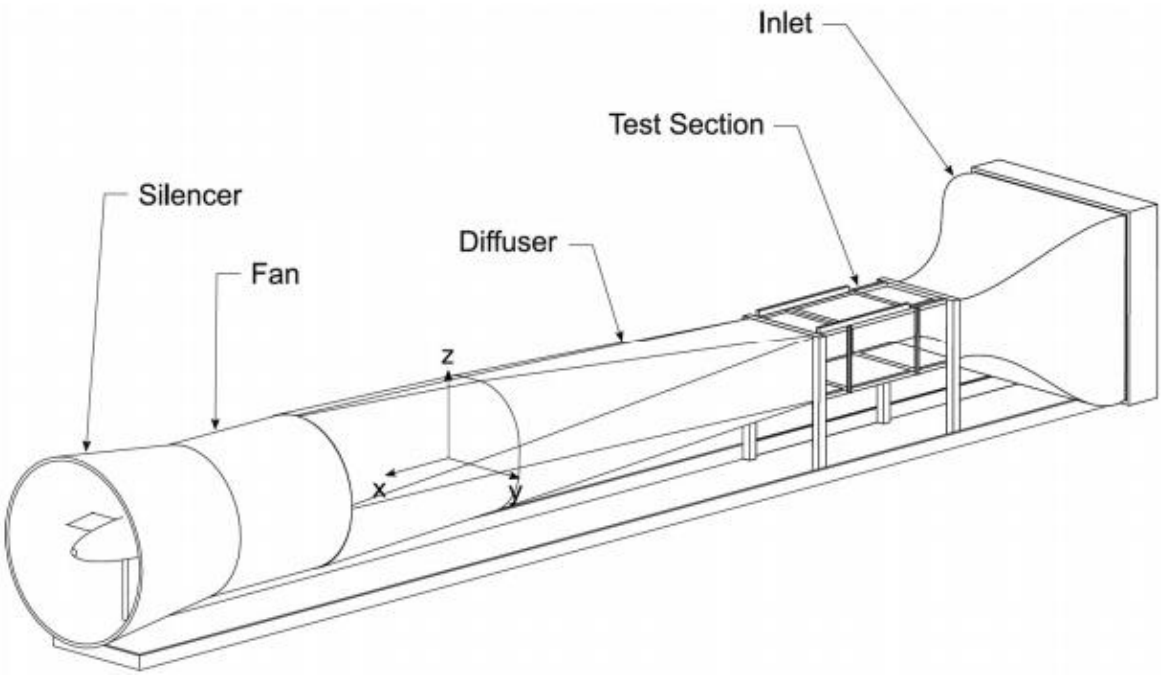

Fig. 2.3. Wind Tunnel Schematic

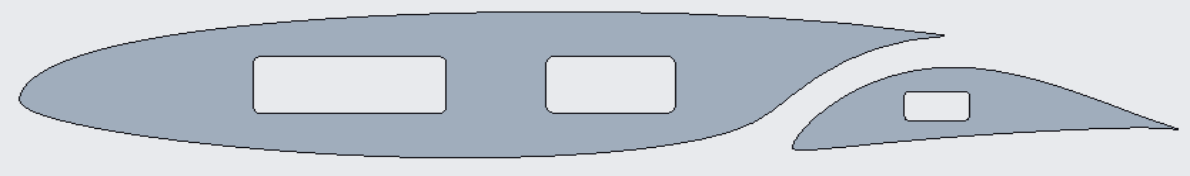

Fig. 2.4. S414 Airfoil with spar locations marked for the fore and aft element. (Image is distorted)

Fig. 2.5. Aluminum Model Mounted in the wind tunnel from floor to ceiling.

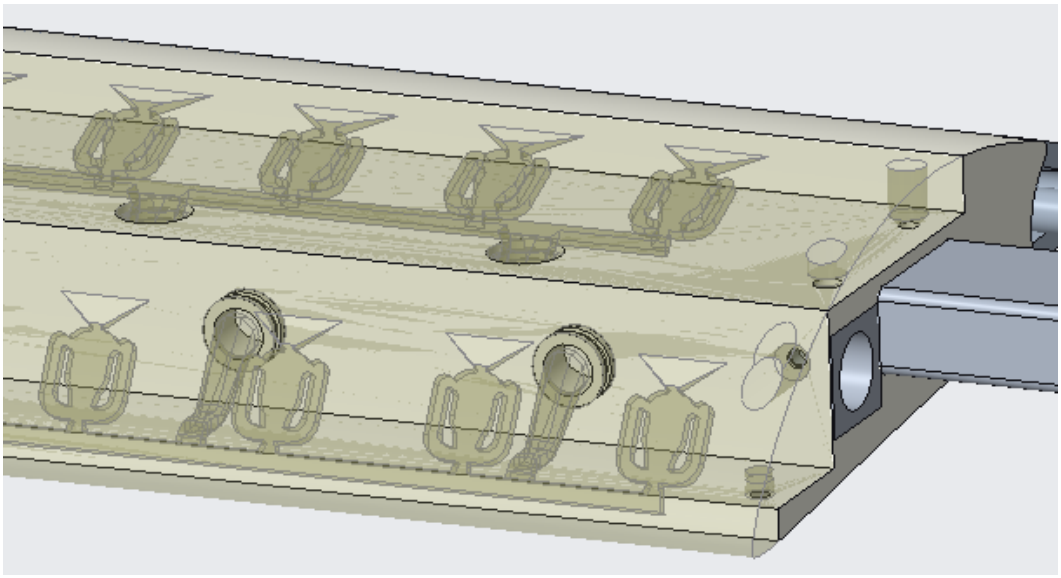

Fig. 2.6. SLA printed aft element with embedded oscillators

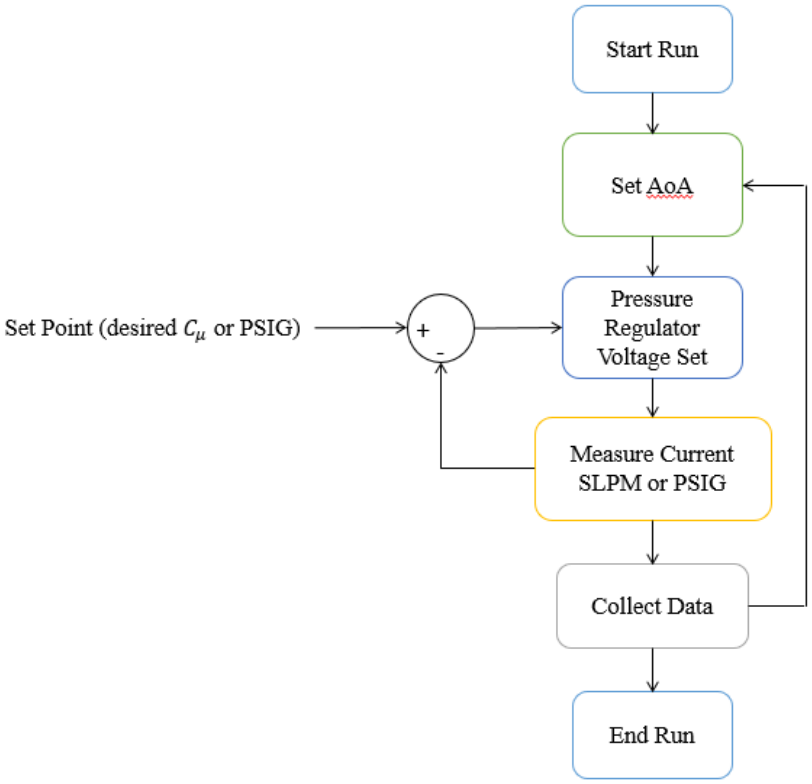

Fig. 2.7. Flow chart detailing the feedback control of the oscillators, either embedded in the model or stand alone

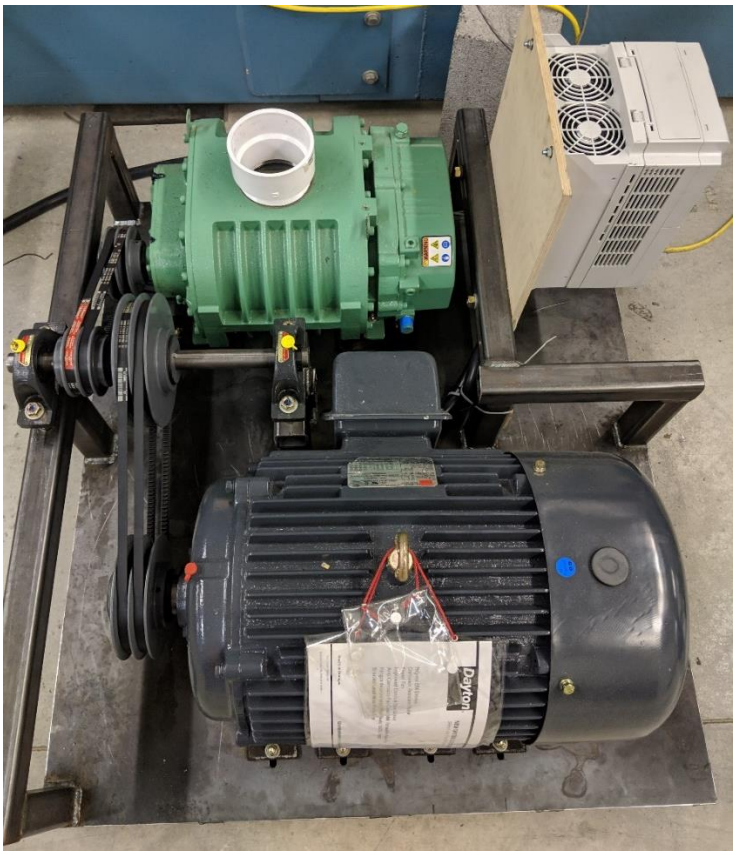

Fig. 2.8. Suction System on the metal pallet

Fig. 2.9. Suction system with the safety cover on

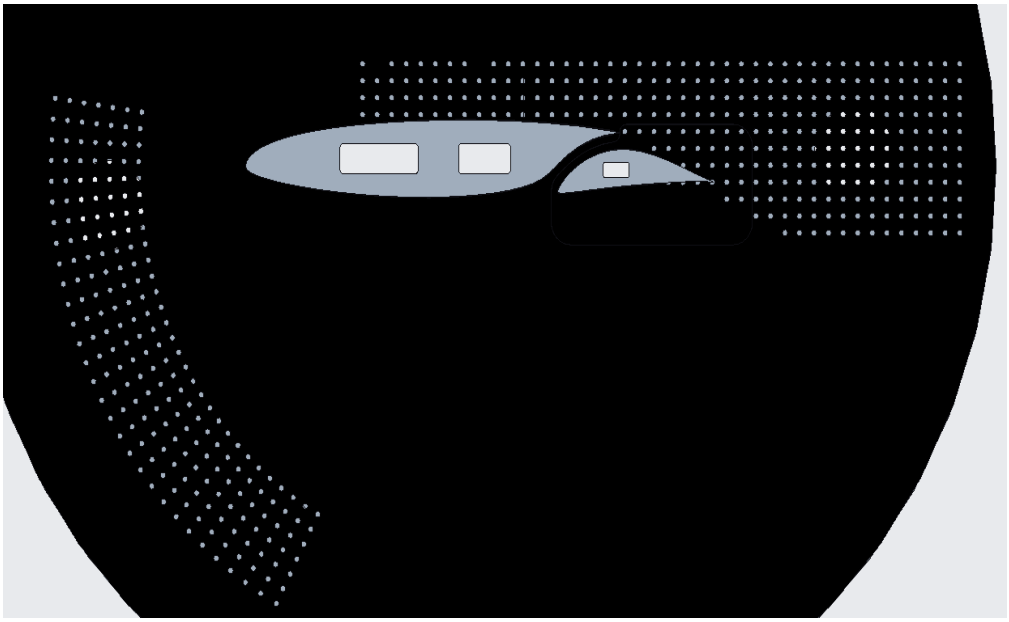

Fig. 2.10. Porous design on the wind tunnel turn table. Airfoil outline with spar holes are marked. (Image is distorted)

Fig. 2.11. Plenum boxes attached to the top and bottom of the wind tunnel, connecting to the suction system.

Fig. 2.12. Wake rake installed in the wind tunnel

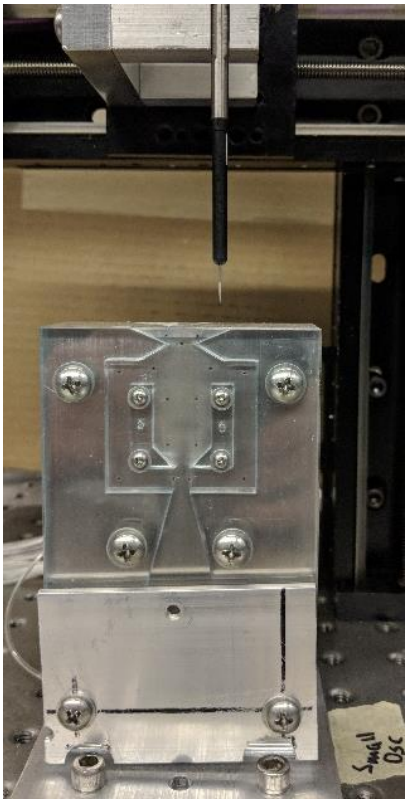

Fig. 2.13. Hot-film probe mounted above a small square fluidic oscillator.

Fig. 2.14. S414 with a deflected flap showing the characteristic length

Chapter 3: Results and Discussion

This chapter details the results from the experimental investigations, including a detailed analysis on the frequency behavior of fluidic oscillators under different geometric variations for each of the two design styles, as well as a predictive model for the round oscillators. Also presented in this chapter is the application of the predictive model to size and embed fluidic oscillators in the S414 airfoil model for testing. Airfoil performance results with the embedded fluidic oscillators are detailed, focusing on three major parameters: oscillator location, aft element rigging, and blowing magnitude.

3.1. Fluidic Oscillators Frequency Analysis

A total of 78 different fluidic oscillators were tested and analyzed over the course of this research. Data were acquired for each oscillator at varying back pressures, from 1 psig to 5 psig in 0.2 psig increments to determine both the individual frequency behavior as well as the frequency behavior with respect to geometric variations.

3.1.1. Initial Frequency Analysis

Once hot-film data were collected for each oscillator at each pressure reading, a FFT was applied to each set of unsteady velocity data to determine the PSD. Fig. 3.1 and Fig. 3.2 shows the PSD of a small round fluidic oscillator and small square fluidic oscillator at 1.0 psig (150 SLPM). A dominant frequency mode was selected from each PSD and assigned to the corresponding

geometry and inlet conditions. In Fig. 3.1, the fundamental peak frequency can clearly be seen occurring at f = 184 Hz, along with a second and third harmonic occurring at f = 368 Hz and f = 552 Hz, respectively. Fig. 3.2 shows fundamental peak frequency occurring at f = 197 Hz, with a less defined second and third harmonic occurring at f = 390 Hz and f = 580 Hz. At this scale, the square oscillators have a higher fundamental frequency than the round oscillators. The round oscillators produce a well-defined narrow peak fundamental frequency, while the square oscillators have much larger bandwidth and the higher order frequencies are not well defined. This bandwidth difference is attributed to the differing internal geometries, where rounded internal geometry has a smoother periodic influence on the jet oscillation, while square edges generate more separation which leads to a less-regular periodicity for the square oscillators.

Due to this non-regular periodicity, some of the square oscillators at varying inlet conditions had spectral peaks that were difficult to decisively identify, as seen in Fig. 3.3. In this case, the square oscillator dominant peak frequency could lie between f = 156 Hz and f = 173 Hz. In other cases, the dominant frequency and the peak frequency do not line up on the same harmonic, making it difficult to build an accurate trendline for the characteristic oscillation frequency of certain fluidic oscillator geometries. Fluidic oscillators, in previous studies, have demonstrated a linear relationship between the mass flow into the oscillator and the resulting frequency of the oscillator. This linear nature was used to help identify the fundamental dominant frequency of the square fluidic oscillators when there were conflicting harmonics.

Once dominant peak frequencies were determined for a given oscillator geometry at all inlet conditions, trendlines were built. Due to the narrow, well-defined frequency bands, the round oscillators show a smooth monotonic increase in frequency as the mass flow is increased, see Fig. 3.4. Square oscillators showed a less regular, non-smooth increase in frequency with respect to the mass flow as a result of their wider frequency bands. In some instances, there were also discontinuous variations in the trendlines for the square oscillators, as seen in Fig. 3.4, caused by different harmonics and frequencies being energized as the inlet conditions were adjusted. This non-smooth frequency behavior can again be attributed to the sharp edges in the mixing chamber creating separated regions that affect the behavior of the fluidic oscillator.

3.1.2. Geometric Variation vs Frequency Behavior

Once baseline oscillator frequencies were determined, comparisons were drawn between the baseline oscillator geometry and geometric variations of the different parameters.

3.1.2.1. Inlet Dependent Frequency Response

Fig. 3.5 through Fig. 3.10 show frequency vs mass flow rate trendlines for the small, large, and large thick round and square oscillators as the inlet dimension is varied by ±10% and ±20%. As discussed in section 3.1.1, the round oscillators show a smooth monotonic increase in the frequency as the as the mass flow increases. Both the small round (Fig. 3.5) and large round (Fig. 3.6) oscillators, with an aspect ratio of 2.0 and 4.0 respectively, show identical trends. As the inlet length is decreased by 10% and 20%, T3 and T4 respectively, the frequency trendline shifted to higher values for the same mass flow. When the inlet length was increased by 10% and 20%, T1 and T2 respectively, the frequency shifted to lower values for the same mass flow. However, the two curves overlap and suggest that there is a threshold that governs how low the frequency will shift as the inlet length is increased, which can be assumed to have been reached between the baseline dimension and the 10% increase. Trends for the large thick round oscillator (Fig. 3.7), aspect ratio of 1.0, shows slightly different trends than the other two round oscillators. An increase in the throat length by 10%, T1, produces a shift of the frequency trendline to higher values, however all other inlet dimensions yielded similar frequency trendlines that overlapped. One possible explanation is a manufacturing imperfection that led to other geometric parameters being varied and shifting the frequency behavior. Assuming a manufacturing defect for the T1 design, the frequency curves for the other dimensions could imply that the limiting threshold was met much sooner when the aspect ratio was 1.0. An additional explanation is that the internal interactions of the flow could be different due to boundary layer growth at different aspect ratios, which leads to differing trends as the throat length was adjusted.

Like the round oscillators, the small square (Fig. 3.8) and large square (Fig. 3.9) oscillators have similar trends as the inlet dimension is varied, while the large thick square (Fig. 3.10) oscillators show a deviation from these trends. Both the small and large square oscillators show that a decrease in the inlet size, T3 and T4, shifted the frequency trendline to decreased values. As the inlet dimension is increased with T1 and T2, there are no clear trends; which is a result of the non-smooth, non-monotonic relation between the frequency and mass flow. While increasing the inlet width leads to a general increase in frequency, a local decrease in frequency is produced across certain mass flows. There was no shift in the frequency curve with the increase in inlet size for the square oscillators, like what was seen for the round oscillators, but instead a change in the shape of the curve was observed. No clear trends were observed for the large thick square

oscillator, with an aspect ratio of 1.0. Both the increase in throat size and decrease in throat size led to an increase in frequency at some mass flows and a decrease at others, when compared to the baseline. The frequency vs mass flow curve trend line was not preserved as the throat size was varied. As seen with LTST2, the frequency harmonics were more statistically distributed and did not show a smooth growth with increasing mass flow, although the variation in the throat width did produce an overall increase in frequency. Underlying inconsistencies in the frequency variation trendlines could possibly be attributed to the internal geometry promoting separation and the influence of boundary layer growth in the AR = 1.0 oscillators.

In conclusion, varying the throat length shifts the frequency curve across increased and decreased values. For the small round and large round oscillators, as the throat length decreases, the frequency curves shift to higher values, while increasing the throat length decreases the frequency until some threshold is reached, and then the oscillation frequency no longer decreases. The large thick round oscillator curves almost all overlap, which could indicate that the threshold has already been met and the throat length was not reduced past the threshold. In general, decreasing the throat length shifts the frequency curves to lower values for the large square and small square geometries, while an increase in throat length leads to a small upward shift in frequency values, but is inconclusive due to irregularity in the curves. The large thick square oscillator geometry provides no clear, predictable trends in the underlying jet oscillation frequency and leads to both increases and decreases in overall frequency values as the inlet conditions vary.

3.1.2.2. Wedge Dependent Frequency Response

Frequency vs mass flow trendlines produced across changes in the wedge length can be seen in Fig. 3.11 through Fig. 3.13 for the round oscillators and Fig. 3.14 through Fig. 3.16 for the square oscillators. In general, adjusting the wedge length also shifts the frequency curves to higher or lower values, depending on the specific aspect ratio and geometric configuration.

Similar to the inlet dependent trendlines, the small round (Fig. 3.11) and large round (Fig. 3.12) oscillators show very similar trends. As the wedge dimension increases by +10%, the frequency is shifted to higher values. Further increasing the wedge dimension to +20% shifts the frequency curve even higher, but by a different amount based on the mass flow. At lower mass flows, the Δf from +10% to +20% is nearly the same Δf as increasing the wedge from the baseline to +10%; however, as the mass flow increases, there is a portion where the frequency no longer increases and then starts to increase again, effectively lowering the harmonic frequency curve by

a small amount. This shift in the frequency behavior is likely due to the larger wedge length scale causing the internal flow field behavior to change as the mass flow increases. As the wedge length decreases, W3 and W4, there is a small decrease observed in the frequency curve; a threshold is quickly reached and the frequency does not further decrease, resulting in overlapping frequency curves close to the baseline curve. The large thick round oscillator (Fig. 3.13) with an aspect ratio of 1.0 shows a slightly different trendline behavior from the other round oscillators. Due to manufacturing issues, the LTRW2 was never tested, so the resulting frequency curve is not displayed. For the LTR geometries, increasing the wedge dimension by +10%, W1, did shift the frequency curve to higher values and decreasing the wedge by -20% showed a similar threshold response where the frequency curve did not decrease. However, decreasing the wedge distance by -10% shifted the frequency curve higher than increasing the wedge distance by +10%, This behavior is very different from previous trends seen and is inconsistent with trends seen with other variants of this design. One possible explanation for the variation in behavior is that there where tolerancing issues with the manufacturing of the large thick oscillators, which could result in other dimensions varying by enough that the behavior of the fluidic oscillator is different than if the wedge dimension had been isolated.

The square oscillators continued to show non-smooth frequency curves as the wedge distances were varied. The small square (Fig. 3.14) and large square (Fig. 3.15) oscillators showed similar trends as the wedge length was increased to +10% and +20%, resulting in the frequency curve to shift towards decreased values. A larger Δf was observed as the wedge length was increased from the baseline geometry to a +10% increase than when the wedge length was increased from +10% to +20%, suggesting that a threshold would be reached that would prevent the frequency from decreasing further, but that threshold has not been reached yet. As the wedge length was decreased, no clear trends were observed in the jet oscillation frequency due to the inconsistent nature of the frequency behavior for the square oscillators. The small square oscillator trendlines are inconsistent and switch between different dominant harmonics as the mass flow changes, resulting in instances of both higher and lower frequencies compared to the baseline geometry. The large square oscillators exhibit increases in frequency in general as the wedge length is decreased, with LSW3 showing a shift in the curve towards increased frequencies, while the LSW4 trendline was inconsistent with other trendlines. When testing the large thick square oscillators (Fig. 3.16), the LTSW4 design had manufacturing issues and was not tested. The other

geometric variations appeared to show the opposite behavior as seen with the small and large square oscillators when the wedge distance was varied. As the wedge distance was increased by +10% and +20%, LSTW1 and LSTW2, the frequency curves shifted towards increased values until a threshold was met, resulting in both curves overlapping on each other. When the wedge distance was decreased by -10%, LSTW3, the frequency curve generally shifted towards decreased frequency values, but some irregularity in this trend was observed, such that some frequencies were higher or lower than the baseline results at lower mass flows. As with the previous square oscillator analysis, it is likely that the internal sharp edges in the geometry promote extensive separated flow in the mixing chamber which led to irregularity in the peak fundamental frequency.

In conclusion, the round and square oscillator configurations show opposite trends as the wedge dimension is varied. The small and large round oscillators increased in frequency with an increase in the wedge dimension and decreased in frequency, up to a threshold, as the wedge dimension decreased. The small and large square oscillators decreased in frequency with an increase in the wedge dimension and in general increased in frequency as the wedge dimension decreased but had irregular trendlines. The large thick round oscillator followed the same trends as seen with the large and small variants, except for one wedge dimension. Trends for the large thick square oscillator were opposite of the large and small square designs, where the increase in wedge dimension led to an increase in frequency and decrease in wedge length led to a decrease in frequency. The inconsistent behavior with the large thick oscillators could be due to manufacturing tolerances, resulting in the variation of wedge dimensions not being isolated. Additionally, the larger thickness of the large thick oscillators could have resulted in additional interactions in the internal flow field as the boundary layer grows, which produces differing frequency behaviors.

3.1.2.3. Outlet Dependent Frequency Response

As the outlet length was varied for the fluidic oscillator designs, the frequency curves show a very different behavior when compared to the other dimensions. Instead of shifting the jet oscillation frequency curves to higher or lower values, the slope either increased or decreased. Fig. 3.17 through Fig. 3.19 show the behavior and resulting trends of the round oscillators, while Fig. 3.20 through Fig. 3.22 show the resulting frequency behavior of the square oscillators.

All three variants of the round oscillators, small (Fig. 3.17), large (Fig. 3.18), and large thick (Fig. 3.19) showed the same behavior. As the outlet length was increased, the slope of the

frequency curve also increased, while the slope of the frequency curve decreased as the outlet length was decreased. For all these cases, at the lowest mass flow and lowest back pressure, the frequency was approximately the same, ≈190 Hz for the SR, ≈105 Hz for LR, and ≈45 Hz for LTR. The one exception to this trend is the LTRB, implying that there could have been some manufacturing tolerancing issue resulting in the frequency behavior changing. This is especially likely since the entire curve was shifted to lower values than for the other dimensions, instead of changing just the slope, which was seen when the other geometric parameters were varied. It can be assumed that even with the boundary layers growing differently in the thick fluidic oscillator, since the geometric variation is at the outlet the boundary layers would have likely mixed long before the outlet and so the thick oscillators behaves like the thinner oscillators that also have quickly growing and mixing boundary layers.

Similar to previous instances, the small square (Fig. 3.20) and large square (Fig. 3.21) oscillators show similar frequency behaviors as the outlet dimension is varied. As with the other square oscillators, the frequency curves are not smooth which makes it difficult to discern trends. While it is not as clear with the small square oscillator curves, the large square oscillators indicate that varying the outlet length changes the slope of the curve instead of shifting the curves as indicated previously for the round oscillators. As the outlet size is decreased, O3 and O4, the frequency curve slope decreases in general. However, there is some inconsistency, the -10% variant appears to reduce the slope more than the -20% variant with the LS group and with the SS group both the -10% and -20% variants have a reduced slope compared to the baseline, but they overlap. Increasing the outlet length gives no clear trends for the square oscillators. There are both increases in the frequency and decreases in the frequency under different inlet conditions for the SS group; the LS group indicates that increasing the outlet length slightly decreases the overall slope of the frequency curve. It could be possible that a threshold has been reached for the square oscillators as the inlet length is increased, but since the oscillatory behavior is more irregular, the curves don't overlap as closely as would be expected. The large square oscillator (Fig. 3.22) frequency curves show no clear trends and are grouped in such a way that it could be assumed that the oscillator is at a threshold value as well and increasing or decreasing the outlet length has no appreciable impact on the frequency behavior. This again implies that the small differences in the frequency curves under varying outlet lengths is caused by the irregularity in the frequency behavior due to internal flow features.

In conclusion, as the outlet length is adjusted, there are very clear trends for the round oscillators that are shared between all three variants, while the square oscillators have few clear trends in their frequency behavior. Instead of shifting the frequency curves up or down, like with the other dimensional changes, varying the outlet length instead changes the slope of the frequency curves. For all three round variants, as the outlet length increases, the slope of the frequency curve increases, while a decreasing outlet length decreases the overall slope of the frequency curve. For the small and large square oscillators, it appears that decreasing the outlet length decreases the slope. However, increasing the outlet length gives no clear trends and could imply that a threshold value has been reached and there would be no appreciable changes in the frequency behavior as the outlet length increases further. The large thick square oscillators have no clear trends for any variation in outlet length and again imply that a threshold could have been reached.

3.1.3. Mass Flow Dependent Frequency Response

During the testing of each oscillator, the inlet conditions were varied by monitoring and adjusting the system total pressure. Previous studies indicated that the operating frequency is linearly related to the mass flow entering the oscillator[2]. Frequency curves for each geometric variant of the LTR design can be found in Fig. 3.23 for frequency vs total pressure, and Fig. 3.24 for frequency vs mass flow. It can easily be seen that there is a non-linear relationship between the oscillator frequency and the total pressure going into the oscillator, but there is a linear relationship between the frequency and the mass flow (kg/s) of the oscillator.

This linear relationship between the frequency and mass flow is dependent on the aspect ratio of the fluidic oscillators. This linear relationship can only be seen with the large thick oscillators, which have an aspect ratio (AR) of approximately 1.0. Examining the frequency curves of all the geometric variations on the small round, AR = 2.0, and large round, AR = 4.0, designs show a non-linear relationship between the frequency and mass flow, Fig. 3.25 and Fig. 3.26 respectively. The effect of the aspect ratio on the frequency behavior of the oscillators is likely occurring due to boundary layer growth across the mixing chamber influencing the internal flow field differently.

3.2. Geometric Based Frequency Model

3.2.1. Non-Linear Frequency Model

All observations and trends observed in section 3.1 were used to attempt to develop a predictive model for the fluidic oscillator frequency behavior. The stepwise regression procedure

outlined in section 2.2 was used to develop linear and non-linear models. Due to the irregularity of the square oscillator frequency behavior, and the inconclusive trends as different geometric parameters were varied in isolation, a model was only developed for the round fluidic oscillators. During the development of the model, five variables were determined to be significant and were then tested for inclusion in the frequency model: $\dot{v}$, l_o, l_t, l_w, and t. Here $\dot{v}$ is the volume flow rate, l_o, l_t, and l_w are the outlet, throat, and wedge lengths respectively, and t is the oscillator thickness.

During the initial development of a frequency model, it was expected that there would be a non-linear relationship between the variables, so the log was taken of each of the five variables. Using the stepwise regression procedure, it was found that each variable had a statistical significance and was included in the model. However, this model, which is discussed in section 3.2.2 was unable to capture certain characteristic features of the frequency behavior. Fig. 3.27 shows the frequency vs mass flow curves for all baseline oscillators and their geometric variants; there are three groupings of frequency curves, corresponding to variations in the scale and aspect ratio of the oscillators. Additionally, each group has a distinct slope for the frequency curve, indicating that there is a strong relationship between the aspect ratio of the oscillator and its frequency behavior. The original model was unable to capture this change in frequency curve slope as the oscillator aspect ratio was varied. Based on this observation, the aspect ratio, with respect to the outlet, was considered and a non-linear predictive model was developed that included the following variables: $\dot{v}$, l_o, l_t, l_w, and AR_o. Non-linear combinations of the variables were also considered during this analysis.

Using the stepwise regression method, it was again found that each variable had statistical significance and should be included in the model. An equation was developed using this method, which can be represented in two ways, a linear representation of the non-linear variables with calculated coefficients, on the resulting non-linear equation.

$$\log(f) = -3.5439 + 0.9624\log(\dot{v}AR_o) - 1.5151\log(l_o) - 0.9980\log(l_t) - 0.4019\log(l_w) \tag{3.1}$$

$$f = \left[\frac{(\dot{v}AR_o)^{0.9624}}{e^{3.5439}{l_o}^{1.5151}{l_t}^{0.9980}{l_w}^{0.4019}}\right] \tag{3.2}$$

Metric units were used during the development of this model, with $\dot{v}$ in m^3/s, and the different lengths all in m. Statistics for the model can be seen in Table 3.1, where overall the model had an

$R^2{}_{adj} = 0.9546$. Fig. 3.28 shows the predicted frequencies of the model overlain with the recorded frequencies, while Fig. 3.29 shows the residuals of the model with a 5% confidence interval; outliers are filled in for both plots.

This model was able to successfully capture the frequency behavior of the fluidic oscillator under different aspect ratios and scales with good accuracy. Consistency in the dimensional units of the model was also approximately preserved with the three length scales in the denominator matching the volume flow rate, yielding a unit of 1/s, to match the units of frequency. Further development of the model will still be needed to handle certain situations and improve its predictive ability. These situations include any thresholds that were reached and lead to an unchanging frequency as the physical geometries continue to change. Additionally, there are numerous conditions outside of the model's viable range, either based on inlet conditions or different geometric combinations not considered during this exploratory investigation. There could be undesirable variations in the internal mechanisms that control the oscillation behavior that occur outside of the tested region and lower the accuracy of the model. Predominantly, it is unknown if the model could still accurately predict the frequency behavior of oscillators with geometry that is on a smaller or larger scale than what was tested.

3.2.2. Early Stage Linear Model Development

In addition to the non-linear model that was developed in section 3.2.1, an earlier linear model was developed to predict the frequency of the fluidic oscillator system. During the development of this model, the natural log of each independent variable was taken, however the dependent frequency variable was kept in its normal form. Linear combinations of non-linear variables were used since there was a visible appearance of a non-linear relationship between various geometric parameters and the oscillator frequency, but variable combinations were not yet considered.

This earlier model was used to size the fluidic oscillators that would be embedded in the SLA printed aft element so airfoil construction could begin while a more detailed and accurate model was still being developed. The model can be seen below,

$$f = -970.74 + 88.36\log(AR_o) + 64.72\log(\dot{m}) - 345.64\log(l_w) \quad (3.3)$$

The statistical data for each coefficient can be seen in Table 3.2 and the model had a corresponding $R^2{}_{adj} = 0.7890$. Metric units were used, kg/s for $\dot{m}$ and m for l_w.

Overall the model clusters of estimated frequency values were consistent with the acquired test data as the aspect ratio and scale is varied, however this earlier model does not accurately represent the change in the frequency curve slope under different geometric conditions. The model overlain with the actual collected data can be seen in Fig. 3.30 with residuals in Fig. 3.31, note the residuals are orders of magnitude larger for this earlier model compared to the final model presented in section 3.2.1. A comparison of this earlier frequency model and the final non-linear predictive model can be seen in Fig. 3.32, showing the predicted frequencies of both models overlain with the collected data.

3.3. Sizing of Embedded Oscillators in the Model

Once a model was developed to predict the frequency of a fluidic oscillator at given inlet conditions, a set of fluidic oscillators were sized to be added to the S414 SNLF airfoil. As discussed in section 2.6, the fluidic oscillators were designed by balancing the non-dimensional actuation frequency, or Strouhal number F^+, and the non-dimensional jet momentum coefficient, C_μ. The oscillators were sized for $F^+ \approx 0.1$ and $C_\mu \approx 0.1 - 0.2\%$. Due to the linear relationship between the mass flow and resulting oscillation frequency, there was a linear relationship between the F^+ and C_μ. In order to fit the fluidic oscillators and the necessary pneumatic routing into the aft element, the total scale of the oscillator was limited. While the scale of the oscillator in the airofil would be outside the range of the developed model, the other geometric parameters were limited to be within ±20% of the baseline geometries and would therefore be in range of the model. The geometry was scaled such that the outlet and inlet lengths would keep their respective baseline values, while the wedge length and oscillator thickness would be varied to reach the desired frequency range across the momentum range of interest.

Fig. 3.33 shows a carpet plot comparing F^+ and C_μ for different wedge lengths with $\alpha = 5°$, an AR of 1.2, and 28 oscillators total. This style of analysis was repeated while varying the number of oscillators, scale, angle of attack, flap deflection, and aspect ratio of the oscillators until a final design was found. Due to the measurement of the critical length scale for the F^+ calculation, a given frequency will yield different values as the angle of attack and flap deflection angle changes. Since not all variables can reach their desired values at all test conditions, oscillator geometry decisions were made such that the system would be close to the desired values for a large range of testing conditions. Designing around the non-dimensional actuation frequency and momentum coefficient, gave an outlet length of 0.075 in, an inlet length of 0.0686 in, a wedge

length of 0.1375 in, and a thickness of 0.0625 in. Each row contains 28 oscillators evenly spread out along the 2.8 ft span, the oscillators were angled within the airfoil such that the ejection angle, θ_{out}, was 15° relative to the surface tangent, which was chosen based on geometric limitations to fit the oscillators and necessary pneumatic lines within the aft element.

Once the non-linear frequency model was built, the expected frequencies and corresponding F^+ and C_μ were calculated and confirmed to have the same general order of magnitude as what was expected from the earlier model. Fig. 3.34 shows the predicted C_μ and f values for the fluidic oscillators embedded in the airfoil as a function of the $\dot{m}$, while Fig. 3.35 shows a carpet plot of the predicted F^+ as a function of C_μ and α.

3.4. Polar Analysis of S414 with Fluidic Oscillators

This section details the lift polar results of the wind tunnel testing that was used to evaluate the effectiveness of fluidic oscillators in improving the lift characteristics of the S414 airfoil. Numerous variables were examined during this testing period, including two different actuation locations, 0.7c and 0.8c, and a range of C_μ from 0.1 to 0.5. Each aft element location, denoted as a case, will be examined individually. The applied actuation locations will be compared as the C_μ is increased, with a subsequent comparison of oscillator effects across actuation location and then against each other.

3.4.1. Qualifying the Suction System

As discussed in Section 2.1.7, a system was designed to apply suction at either end of the mounted model in the wind tunnel. Before testing the airfoil system with and without the embedded fluidic oscillators, an analysis was performed to evaluate the true effect of the applied suction on the performance of the airfoil. Lift data was collected for the aluminum airfoil model for a range of VFD settings, from 30 Hz to 50 Hz in 5 Hz increments. Pressures for the spanwise taps and the resulting $C_{l,max}$ was examined and compared for each of the motor settings. The spanwise pressure distribution for $\alpha = 5°$ and $\alpha = 15°$ are shown in Fig. 3.36 and Fig. 3.37, respectively.

The $\alpha = 5°$ case shows a region of lower pressure at either end of the airfoil section, where there are still interactions with the tunnel walls, before it starts to even out along most of the span of the airfoil section. There is a large variance in the pressure distribution across the spanwise section with no applied suction, indicating 3D flow effects which would reduce the effective $C_{l,max}$ of the airfoil. While the tunnel wall interactions are not completely removed at either end of the

model, the application of suction on the tunnel walls does even out the spanwise distribution. As the VFD frequency setting is increased, the spanwise pressure distribution has a more even distribution and better approximates the lift distribution of a 2D airfoil. At $\alpha = 15°$, there are different flow features which lead to a less uniform spanwise distribution than at $\alpha = 5°$, however the applied suction is still shown to smooth out the spanwise distribution.

A comparison of the lift curve for each case can be seeing in Fig. 3.38. With no applied suction, the airfoil stalls at $\alpha \approx 16.5°$ instead of $\alpha \approx 17.5°$ when suction is present. Additionally, the application of sidewall suction increased the $C_{l,max}$ from 1.98 with no suction to about 2.04 with the VFD set at 50 Hz, approximately a 3% increase in lift. Based on the collected data, it was determined that the sidewall suction system was functioning as expected and improving the 2D flow aspects of the model. While a VFD setting at 50 Hz did provide the greatest improvements, future tests were conducted at a VFD setting of 45 Hz since there was only a marginal improvement in the lift when increasing from 45 Hz to 50 Hz and the spanwise pressure distribution is still smooth and even at 45 Hz.

3.4.2. Non-Dimensional Frequency

As detailed in section 2.6, two major control parameters were used during the design of the fluidic oscillators for embedding in the SLA-printed aft element, the dimensionless frequency, F^+, and the jet momentum coefficient, C_μ. As discussed earlier, the fluidic oscillator frequency is linearly related to the inlet conditions and the internal geometry of the oscillator. For consistency during data collection and to better compare against previous studies, C_μ was kept constant throughout each test run. In order to keep C_μ constant, the mass flow was also kept constant throughout each run, which results in a constant actuation frequency maintained during each run. As the angle of attack was increased throughout each run, the characteristic length, l_c, would also increase and result in the F^+ changing during each test. It should be noted that while F^+ did vary throughout each run, the order of magnitude was consistent per run. Fig. 3.39 illustrates this behavior by showing the variation in the F^+ with respect to the angle of attack for the HLC at various C_μ settings. The fluidic oscillators were sized so that the baseline S414 configuration would be actuated around $F^+ \approx 0.1$, however this is not true for the HLC; each flap deflection also resulted in different F^+ ranges. In general, the F^+ was considered when sizing the fluidic

oscillators for the airfoil, however the C_μ became the main control variable during testing and only the F^+ order of magnitude was targeted.

3.4.3. Baseline Configuration

Results from the baseline S414 configuration analysis can be seen with Fig. 3.40 through Fig. 3.51. Fig. 3.40 through Fig. 3.43 contain lift curves for the leading-edge oscillators with $\delta_f =$ 0, 10, 20, and 30 deg; Fig. 3.44 through Fig. 3.47 show the lift curves for the upper surface oscillator set with δ_f from 0 to 30 deg. Results from both sets of oscillators are summarized in Fig. 3.48 through Fig. 3.51, which contain the entire lift curve in subplot a) and a lift curve zoomed in on the positive angle stall in subplot b), this occurs for δ_f from 0 to 30 deg.

While the upper surface oscillators could be tested to a max $C_\mu = 0.5$, limitations in the rigidity of the 3D printed aft element components meant the leading-edge oscillators could only be tested to a max $C_\mu = 0.3$ for the baseline configuration. During some runs, an error would occur mid test and a run had to be restarted, so some lift curves at a given oscillator and C_μ value are the combination of two runs, as seen with Fig. 3.41. The S414 configuration is a leading-edge stall type and has a sharp drop in effective lift once at the positive angle of attack stall is exceeded; the negative angle of attack stall is more gradual and does not have as large of a ΔC_l when the flow reattaches. This differing stall behavior could be a result of data collection going from negative to positive angle of attack and some hysteresis effects leading to a more gradual reattachment of the flow field.

At $\delta_f = 0°$, the baseline airfoil with no fluidic oscillator control has a $C_{l,max} \approx 2.0$ at an angle of attack around 17.5°. Adding leading edge fluidic oscillators had a negligible effect on the resulting lift curve for both $C_\mu = 0.1$ and $C_\mu = 0.3$. The lift curve is shifted down slightly, on the order of $\Delta C_l \approx 0.02$, and the $C_{l,max} \approx 1.95$, which occurs around 16.5° for both momentum settings. The positive stall process is also smoothed out a small amount, producing a more gradual stalling behavior with the leading edge actuation. The addition of upper surface oscillators shifted the lift curve up by a small amount, approximately $\Delta C_l \approx 0.025$ for $C_\mu = 0.1$ up to approximately $\Delta C_l \approx 0.03$ for $C_\mu = 0.5$. As the C_μ increases and the lift curve slope shifts up, $C_{l,max}$ increases from 1.95 to 2.0 at an angle of attack, $\alpha = 16.5°$.

At $\delta_f = 10°$, the baseline airfoil with no fluidic oscillator control has a $C_{l,max} \approx 2.175$ at an angle of attack of $\alpha = 16.5°$. The addition of the leading edge oscillators again results in a

negligible change at both $C_\mu = 0.1$ and $C_\mu = 0.3$. The lift curve is shifted down by about $\Delta C_l \approx 0.05$ for both momentum settings across the entire lift curve. At a $C_\mu = 0.1$, $C_{l,max} \approx 2.1$ at an angle of attack of $\alpha = 16.5°$, while the $C_{l,max} \approx 2.09$ at $\alpha = 15.5°$ and $C_\mu = 0.3$. The stall behavior is still sharp with a $C_\mu = 0.1$, but is slightly softened with a $C_\mu = 0.3$. Upper surface actuation resulted in a larger downward shift of the lift curve, by approximately $\Delta C_l \approx 0.15$ at a $C_\mu = 0.1$ and a $C_\mu = 0.3$. Increasing the momentum coefficient to $C_\mu = 0.5$ results in the lift curve shifting up slightly by $\Delta C_l \approx 0.015$. The $C_{l,max} \approx 2.05$ at stall angles of attack of $\alpha = 17.5°$ and $\alpha = 16.5°$ for the lower C_μ values, 0.1 and 0.3 respectively, while $C_{l,max} \approx 2.185$ for $C_\mu = 0.5$. It is likely that the lift curve behavior for the upper surface oscillators is not consistent due to issues with tape seams creating additional flow field features and artificially reducing the lift curve.

At $\delta_f = 20°$, the $C_{l,max} \approx 2.25$ at $\alpha = 16.5°$ for the baseline geometry with no active flow control. The addition of flow control from leading edge fluidic oscillators had no effect on the lift curve at either $C_\mu = 0.1$ or $C_\mu = 0.3$, resulting in the lift curves overlapping the baseline curve except at the positive angle of attack stall. The positive stall process was sharp for both momentum values, with the $C_{l,max} \approx 2.19$ at $\alpha = 15.5°$. The upper surface oscillators overlapped with the baseline lift curve at all C_μ, increasing from 0.1 to 0.5. As the $C_\mu$increased from 0.1 to 0.5, there was a slight shift in $C_{l,max}$, going from 2.21 to 2.24 to 2.18. Overall the stall behavior stayed sharp, indicating that there are likely geometric features, such as tape seams, that created the small differences in the airfoil lift.

When the flap was deflected to 30°, the baseline S414 system had a $C_{l,max} \approx 2.3$ at $\alpha = 15°$. Adding leading edge fluidic oscillators had no effect on the lift curve in the lower angle of attack regime, but at higher angle of attacks (above 5°) there was a large reduction in the lift curve slope. Upper surface fluidic oscillators similarly had no effect on the lift curve at the lower C_μ values, 0.1 and 0.3, resulting in overlapping lift curves with the baseline configuration. At $C_\mu = 0.5$, the $a_{L=0}$ overlaps with the baseline analysis, but the lift curve slope is reduced, indicating significant 3D effects leading to a reduction in the overall lift at higher AOAs. During testing of the airfoil system, seams were taped over in order to help reduce manufacturing-based 3D effects in the results. However, during testing of both the leading edge and upper surface fluidic oscillators at a $\delta_f = 30°$, this tape started to lift and create large 3D effects across the airfoil model, leading to the reduction of the lift curve slope. Previous testing at other flap deflections indicate that the

S414 airfoil system sees little benefit when adding leading edge flow control, so this set of testing was not repeated as it was assumed to follow the trends already seen with earlier testing.

Overall, the largest ΔC_l occurs with the upper surface oscillators at a $C_\mu = 0.5$ for each flap deflection. However, the most efficient increase in lift occurs with the upper surface oscillators at $C_\mu = 0.1$, where the largest upward shift in the lift curve can be seen with respect to the applied oscillation. As the C_μ increases, the airflow around the aft element becomes energized and "saturated", such that further increasing the momentum has diminishing returns. The leading edge mounted fluidic oscillators did not show any appreciable effect on the resulting lift curve; in many cases the lift curve shifted slightly down, which could be a result of tape seams and other manufacturing defects. Additionally, as the mass flow limits are reached for each oscillator set, back pressure combined with the pressure gradient over the airfoil surface can result in components starting to bend and deform which alters the shape of the airfoil and leads to a decrease in the effective lift of the airfoil system.

3.4.3.1. S414 C_p Plot Analysis

The C_p distribution of the baseline S414 configuration with no actuation shows the expected relationship between the two elements. The aft element supports the large pressure recovery and as a result the fore element maintains a favorable pressure gradient along its entire length. As the flap is deflected, the flow velocity increases around the upper surface and decreases around the lower surface generating higher lift at a given angle, as expected. There is a laminar separation bubble that can be seen from around 0.85c to 0.9c, which matches what was seen during the initial development of the airfoil[12]. This laminar separation bubble can be seen at all flap deflections and is one of the features that the fluidic oscillators could delay or improve upon. Fig. 3.52 shows the C_p distribution for the S414 configuration with no actuation for all four tested flap deflections at $\alpha = 1°$. Fig. 3.53 shows the C_p distribution of the S414 configuration for $\delta_f = 0°$ without actuation, and with applied actuation of $C_\mu = 0.1$ for both the leading edge and upper surface oscillator configurations.

The addition of leading edge actuation does create a small low-pressure peak in the C_p distribution around the actuation location of 0.7c, however it does not have a large effect on the resulting C_p distribution. Actuation from the leading edge oscillator set is not applied near the laminar separation bubble and instead is applied where there is already a suction peak and

favorable pressure gradient, which could be saturating the flow field sooner and reducing any potential benefits of the additional momentum. Overall, the leading edge fluidic oscillators offer little benefit to the airfoil system due to their location with respect to flow features on the S414 airfoil configuration.

Upper surface actuation is applied further aft at 0.8c, which is right before the laminar separation bubble. It can be seen in Fig. 3.53, that the application of this oscillation slightly lowers the suction peak of the aft element and instead promotes favorable pressure gradients further along the surface until the formation of a laminar separation bubble around 0.86c before the flow becomes turbulent. The application of the upper surface oscillators increases the circulation around the aft element and slightly lowers the circulation load of the fore element, leading to the increase in C_l seen in the lift curve polars. Since the flow is attached for almost the entire length of the chord in the baseline S414 configuration, there is only a small improvement in the lift of the airfoil system.

As the flap is deflected from $\delta_f = 10°$ to $\delta_f = 30°$, there is a region of separation that forms over the flap. Neither leading edge or upper surface actuation was able to alleviate or delay this separation at any C_μ value for $\delta_f \geq 20°$, see Fig. 3.54. Upper surface actuation can partially alleviate the separation at $\delta_f = 10°$ with $C_\mu \geq 0.1$, see Fig. 3.55, but no amount of actuation was able to completely prevent or alleviate separation.

At higher angles of attack, the C_p distribution is largely unaffected by the applied actuation at either location. Fig. 3.56 shows the C_p distribution for no actuation as well as applied actuation at both the leading edge and upper surface for $C_\mu = 0.1$ at $\alpha = 15°$. Circulation around the fore element is largely unaffected, while the circulation around the aft element is largely unaffected by the leading edge actuation and is shifted to a higher aft loading by the upper surface actuation. This behavior is consistent at higher C_μ and other flap deflections as well.

With the application of upper surface actuation, the flow field around the fore element was quickly saturated and increased C_μ had a negligible effect, resulting in little change of the C_p distribution after the initial reduction in the circulation around the fore element. At a $C_\mu = 0.1$ and $C_\mu = 0.3$ the C_p distribution is shifted to feature increased aft loading on the airfoil, though the increase in actuation amplitude does not significantly alter the aft-element pressures, implying a saturation of the flow field around the aft element. However, at $C_\mu = 0.5$ the C_p distribution reverts

back to what was seen no applied actuation. This trend with the aft element was seen throughout the α sweep and can be seen for $\alpha = 1°$ in Fig. 3.57.

The application of the leading edge actuation had similar effects on the resulting C_p distribution as the upper surface actuation at a $C_\mu = 0.1$ and $C_\mu = 0.3$. The circulation around the fore element is slightly decreased, but then the flow field is "saturated" and there is little further change as the C_μ is increased. The circulation around the aft element also appears to reduce slightly and does not change any further as the C_μ is increased; this behavior can be seen in Fig. 3.58.

3.4.4. High Lift Configuration

Results from the HLC analysis can be seen with Fig. 3.59 through Fig. 3.70. Fig. 3.59 through Fig. 3.62 show lift curves for the leading edge oscillators with $\delta_f = 0$, 10, 20, and 30 deg; Fig. 3.63 through Fig. 3.66 show the lift curves for the upper surface oscillators with δ_f from 0 to 30 deg. Results from both sets of oscillators are summarized in Fig. 3.67 through Fig. 3.70, which contain the entire lift curve as subplot a) and a lift curve zoomed in on the positive angle of attack stall as subplot b), across a range of δ_f from 0 to 30 deg. Even in the different configuration the stall is still very sharp at the positive angle of attack stall, while smoother and less sudden at the negative angle of attack stall. In order to reach the larger momentum values of $C_\mu = 0.5$ for both leading edge and upper surface actuation, additional attachment points were drilled into the SLA printed parts to prevent bending of the components.

At $\delta_f = 0°$, the baseline airfoil in the HLC has a $C_{l,max} \approx 2.39$ at an angle of attack $\alpha = 14.5°$. Both leading edge and upper surface actuation had a positive effect on the resulting lift behavior of the configuration, the results can be seen in Table 3.3. The addition of actuation results in an overall positive shift in the lift curve, presented as ΔC_l in Table 3.3, across most of the α range. However, the stall behavior and resulting $\Delta C_{l,max}$ is not always consistent with the ΔC_l. This disagreement between the $\Delta C_{l,max}$ and ΔC_l will be seen for all δ_t in the HLC. The sharp, sudden stall behavior still occurs for the leading edge oscillator set at the lower two settings with $C_\mu = 0.1$ and $C_\mu = 0.3$, while the sudden stall behavior only exists at the lowest setting at $C_\mu = 0.1$ for the upper surface fluidic oscillator set. Once the momentum addition from the fluidic oscillators is high enough, $C_\mu = 0.5$ for the leading edge oscillators and $C_\mu = 0.3$ or $C_\mu = 0.5$ for the upper surface oscillators, then the stall behavior starts to smooth out and the lift is observed to not decrease as quickly once stall is reached.

For $\delta_f = 10°$, the baseline airfoil in the HLC, has a $C_{l,max} \approx 2.44$ at an angle of attack $\alpha = 13.5°$. Both leading edge and upper surface actuation had a positive effect on the resulting lift behavior of the configuration, the results can be seen in Table 3.4. The sharp, sudden stall behavior occurs for all oscillator settings except for the baseline configuration with $\delta_f = 10°$ and the leading edge oscillator set at a $C_\mu = 0.1$, which have a slightly smoother stall.

For a $\delta_f = 20°$, the baseline airfoil in the HLC, has a $C_{l,max} \approx 2.53$ at an angle of attack $\alpha = 13.5°$. The stall behavior seen during previous cases continues for this flap deflection as well, although both the baseline case with a 20° deflection and no actuation and the case with leading edge oscillators at a $C_\mu = 0.3$ have a slightly smoother stall behavior. The addition of momentum control through both the leading edge and upper surface oscillators provided a positive effect on the lift behavior and shows similar trends as seen with the previous flap deflections, the results can be seen in Table 3.5.

For a $\delta_f = 30°$, the baseline airfoil in the HLC, has a $C_{l,max} \approx 2.53$ at an angle of attack $\alpha = 13.5°$. With no actuation, $\delta_f = 30°$, and leading edge oscillators at $C_\mu = 0.3$, the lift curve has a slightly smoother stall behavior, while all other test conditions still have the characteristic sharp leading edge stall. The addition of momentum control through both the leading edge and upper surface oscillators continues to create a positive effect on the lift behavior and shows similar trends as seen with the previous flap deflections, see Table 3.6.

Several very distinct behaviors showed up in the lift curve with actuation for the airfoil in the HLC. For all flap conditions, the largest ΔC_l occurred at $C_\mu = 0.5$, however, the airfoil system was most efficient at $C_\mu = 0.1$. In this way, the airfoil, for both upper surface and leading edge oscillator configurations, almost always saw the largest relative increase in lift with respect to the applied actuation at $C_\mu = 0.1$. As the applied actuation further energized the surrounding flow, there were some marginal gains in lift, but the flow field became "saturated" and there were diminishing returns with increased actuation amplitude. Upper surface oscillators were shown to be more effective than the leading edge oscillators when in the HLC. For almost all flap deflections, the smallest applied actuation, $C_\mu = 0.1$, with the upper surface actuators provided a larger increase in lift than that of the largest applied actuation, $C_\mu = 0.5$, with the leading edge oscillators.

3.4.4.1. High Lift Configuration C_p Plot Analysis

Comparisons between the C_p distributions of the HLC at each of the four tested flap deflections can be seen in Fig. 3.71. Due to the aggressive positioning of the aft element, most of the upper surface of this element is separated, which is seen for all flap deflections. Around 0.7c there is a sudden increase in suction in the C_p distribution over the aft element, which is caused by the accelerated flow "dumping" off the fore element trailing edge and then energizing the flow field around the aft element. The C_p distributions for the HLC with no actuation compared to leading edge and upper surface actuation with $\delta_f = 0°$ can be seen in Fig. 3.72.

The leading edge oscillator set ejects at 0.7c, which is consistent with the region of increased suction observed previously; this pressure peak leads to a faster saturation of the actuation authority in the flow field and diminishes the total effectiveness of the leading edge oscillators. There is some increase in the overall circulation around both elements which does lead to a slight increase in the C_l of the airfoil. Leading edge oscillators do offer more improvements with the HLC compared to the baseline S414 configuration since a larger portion of the chord benefits from momentum addition, however it is still less efficient than the application of upper surface actuation.

Upper surface oscillators reenergize the boundary layer at 0.8c, which corresponds to the beginning of the large regions of massive separation in the HLC. The actuation at the separated region leads to a large increase in the circulation around both elements and slightly alleviates the separated region on the upper surface. However, the separation region is not completely removed, as the upper surface actuation has diminishing returns as the C_μ increases and the flow becomes "saturated" before the separation region can be overpowered. Overall, a large increase in the airfoil C_l can be seen with the application of the upper surface oscillators.

Due to the larger flow features that would benefit from momentum injection, significant improvements in the lift behavior are seen with the addition of either leading edge or upper surface actuation. The oscillator position with respect to the flow features lead to the upper surface oscillators generating larger improvements in the airfoil system lift than that of the leading edge oscillators. This behavior is continued throughout the test regime of the HLC, at all angles of attack and flap deflections.

As discussed in section 3.4.4, increasing the C_μ quickly "saturates" the flow field and there are diminishing increases in lift with increased C_μ for both the leading edge and upper surface oscillators. Fig. 3.73 shows the C_p distributions for the HLC with no actuation and applied leading edge actuation at all C_μ values tested at $\alpha = 1°$. At this angle of attack, the C_p distributions start to overlap with $C_\mu = 0.1$ showing the saturation of the actuation effect. C_p distributions for the HLC with no actuation and applied upper surface actuation at all C_μ values tested at $\alpha = 1°$ can be seen in Fig. 3.74. At this angle of attack, there is an increase in circulation going from no actuation to $C_\mu = 0.1$ and another smaller increase in circulation as C_μ is increased to 0.3. After $C_\mu = 0.3$, the C_p distributions start to overlap and there is no appreciable increase in lift.

Similar to lower α, the flow fields at higher α get saturated and an increase in C_μ results in C_p distributions that start to overlap. This can be seen in both Fig. 3.75 and Fig. 3.76 comparing the C_p distributions for leading edge and upper surface actuation, respectively, at various C_μ for $\alpha = 15°$.

3.5. Chapter 3 Tables

Table 3.1 Non-linear model calculated constants and resulting statistical data

Variable	$\boldsymbol{\beta_i}$	**SE($\boldsymbol{\beta_i}$)**	$\boldsymbol{t^*}$	**P**
Constant (β_0)	-3.5439	0.0733	-48.32	4.11E-234
$\log(\dot{v}AR_o)$	0.9624	0.0125	76.74	0.00E+0
$\log(l_o)$	-1.5151	0.0464	-32.63	6.21E-147
$\log(l_t)$	-0.9980	0.0425	-23.48	2.30E-92
$\log(l_w)$	-0.4019	0.0467	-8.60	2.33E-17

Table 3.2 Early model calculated constants and resulting statistical data

Variable	$\boldsymbol{\beta_i}$	**SE($\boldsymbol{\beta_i}$)**	$\boldsymbol{t^*}$	**P**
Constant (β_0)	-970.74	22.54	-43.07	2.69E-206
$\log(l_t)$	88.36	3.88	22.78	0.00E+00
$\log(\dot{m})$	64.72	6.11	10.59	0.00E+00
$\log(l_w)$	-345.64	10.24	-33.75	1.56E-153

Table 3.3 Results of testing the HLC with $\boldsymbol{\delta_f = 0°}$

Oscillator	C_μ	ΔC_l	$C_{l,max}$	$\alpha_{C_{l,max}}$
Leading Edge	0.1	0.05	2.42	14.5
Leading Edge	0.3	0.07	2.44	14.5
Leading Edge	0.5	0.08	2.36	14.5
Upper	0.1	0.09	2.46	14.5
Upper	0.3	0.14	2.44	14.5
Upper	0.5	0.15	2.44	14.5

Table 3.4 Results of testing the HLC with $\boldsymbol{\delta_f = 10°}$

Oscillator	C_μ	ΔC_l	$C_{l,max}$	$\alpha_{C_{l,max}}$
Leading Edge	0.1	0.01	2.43	13.5
Leading Edge	0.3	0.03	2.46	13.5
Leading Edge	0.5	0.05	2.46	13.5
Upper	0.1	0.07	2.48	13.5
Upper	0.3	0.09	2.53	13.5
Upper	0.5	0.11	2.54	13.5

Table 3.5 Results of testing the HLC with $\boldsymbol{\delta_f = 20°}$

Oscillator	C_μ	ΔC_l	$C_{l,max}$	$\alpha_{C_{l,max}}$
Leading Edge	0.1	0.01	2.53	13.5
Leading Edge	0.3	0.03	2.55	13.5
Leading Edge	0.5	0.04	2.55	13.5
Upper	0.1	0.05	2.56	13.5
Upper	0.3	0.07	2.58	13.5
Upper	0.5	0.09	2.56	13.5

Table 3.6 Results of testing the HLC with $\boldsymbol{\delta_f = 30°}$

Oscillator	C_μ	ΔC_l	$C_{l,max}$	$\alpha_{C_{l,max}}$
Leading Edge	0.1	0.06	2.58	13.5
Leading Edge	0.3	0.07	2.60	13.5
Leading Edge	0.5	0.08	2.58	13.5
Upper	0.1	0.09	2.58	13.5
Upper	0.3	0.09	2.55	12.5
Upper	0.5	0.09	2.61	13.5

3.6. Chapter 3 Figures

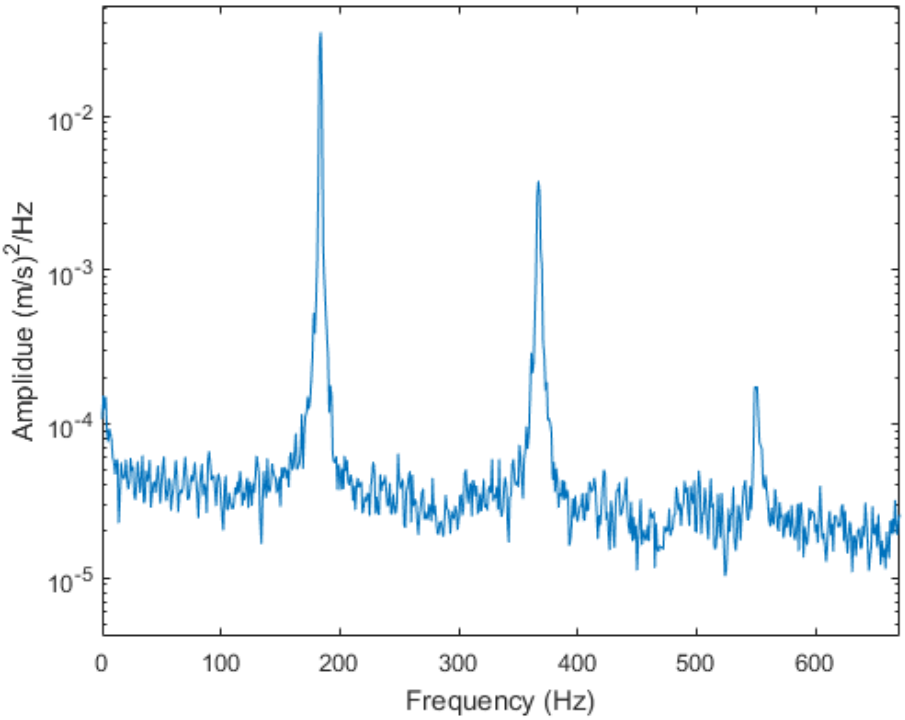

Fig. 3.1 PSD for Baseline Small Round Oscillator (7.0 kPa)

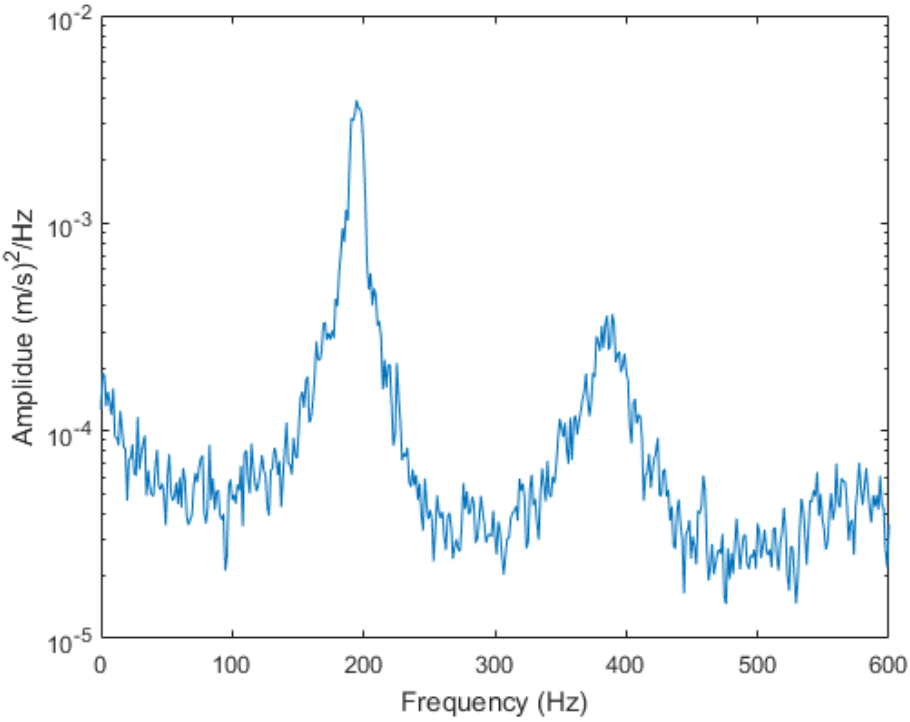

Fig. 3.2 PSD for Baseline Small Square Oscillator (7.0 kPa)

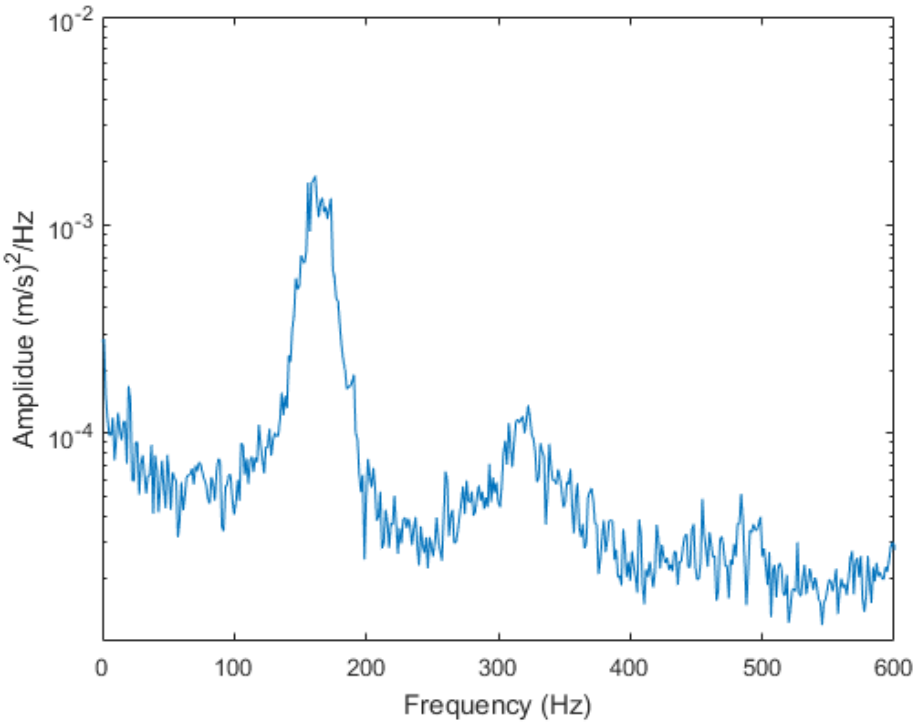

Fig. 3.3 PSD for Baseline Large Square Oscillator (14.0 kPa)

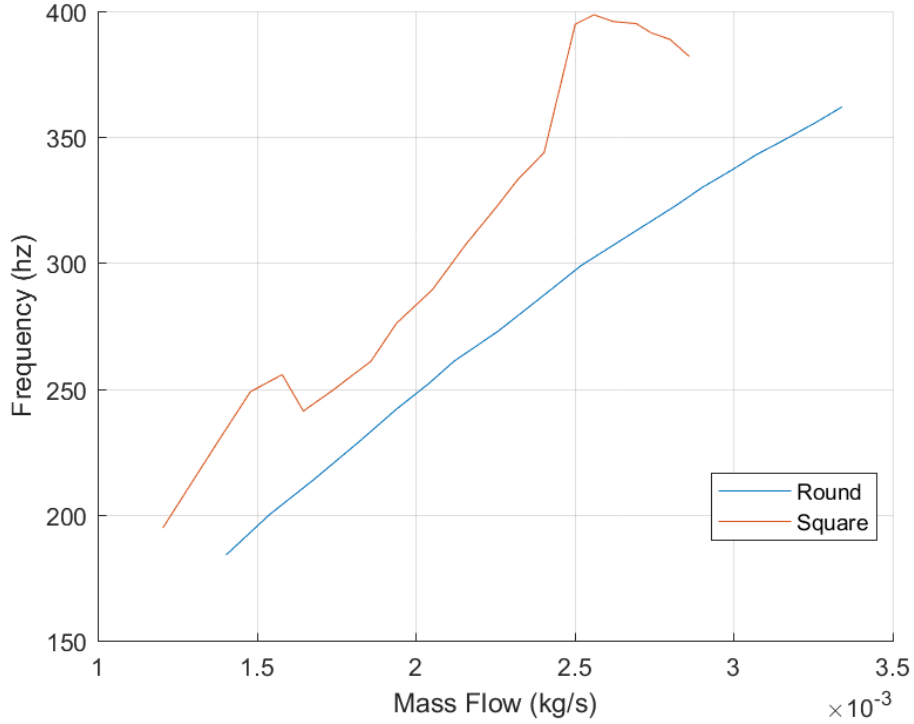

Fig. 3.4 Frequency vs Mass Flow for Small Round and Square Fluidic Oscillators

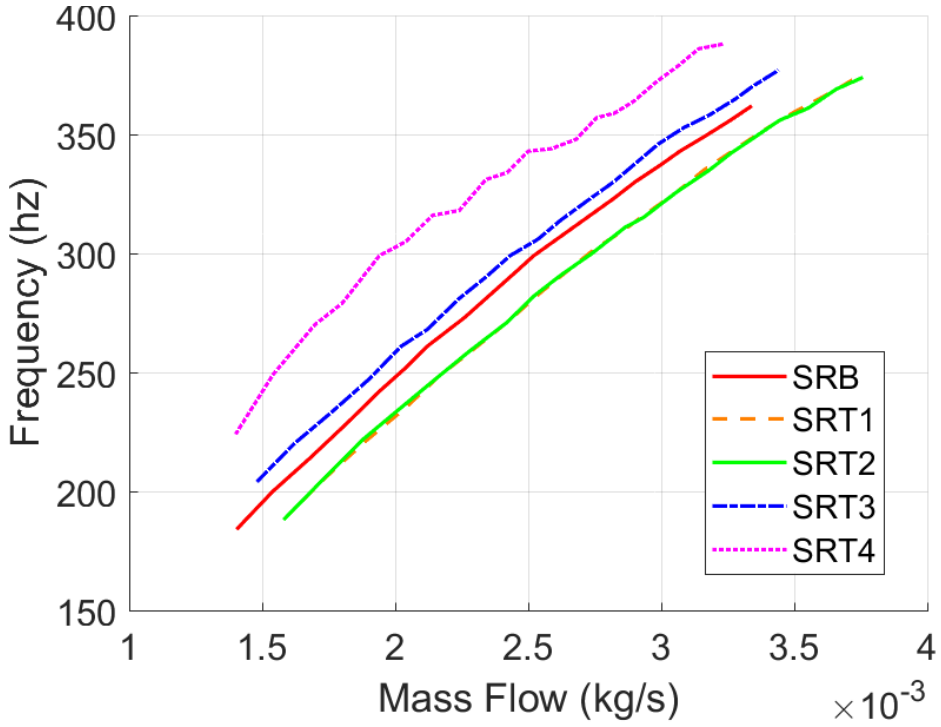

Fig. 3.5 Frequency vs mass flow rate for the small round oscillators with the throat geometry varied by ±10% and ±20%.

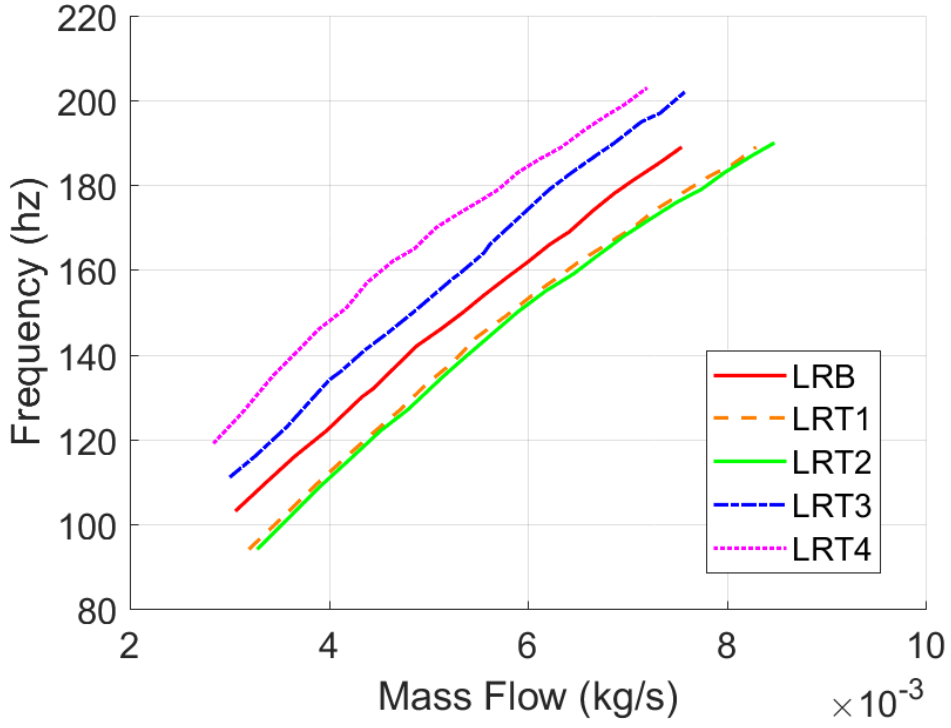

Fig. 3.6 Frequency vs mass flow rate for the large round oscillators with the throat geometry varied by ±10% and ±20%.

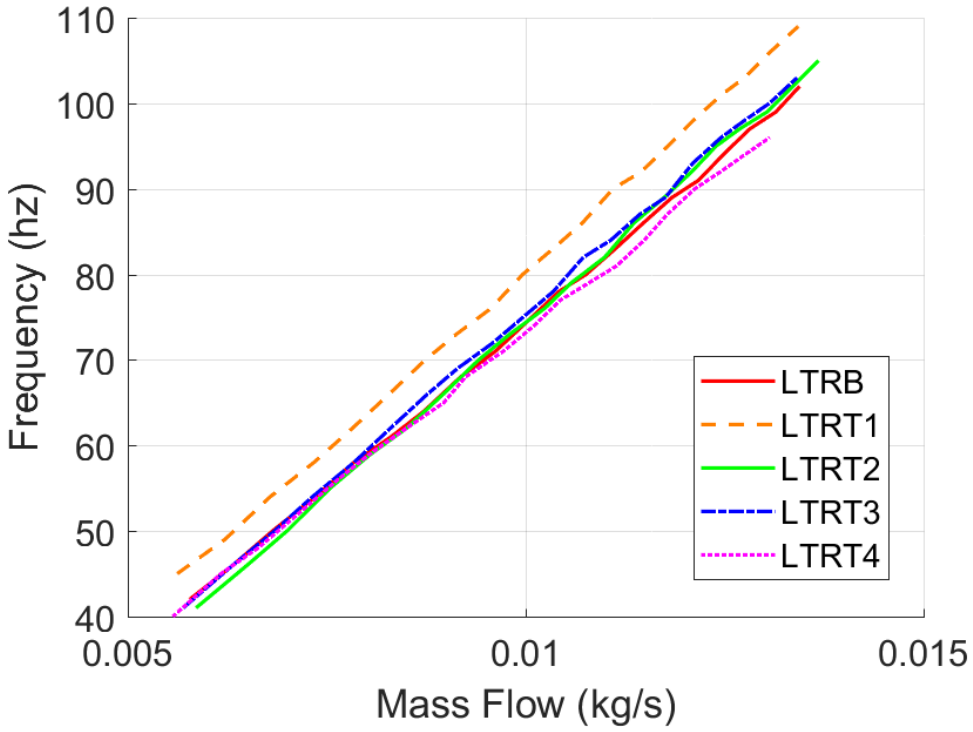

Fig. 3.7 Frequency vs mass flow rate for the large thick round oscillators with the throat geometry varied by ±10% and ±20%.

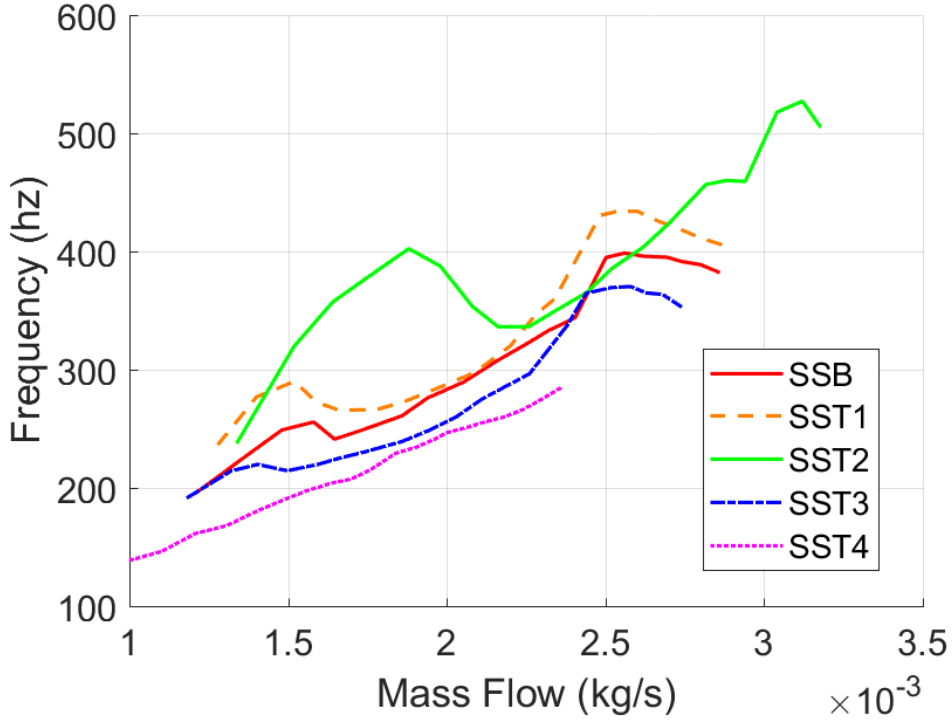

Fig. 3.8 Frequency vs mass flow rate for the small square oscillators with the throat geometry varied by ±10% and ±20%.

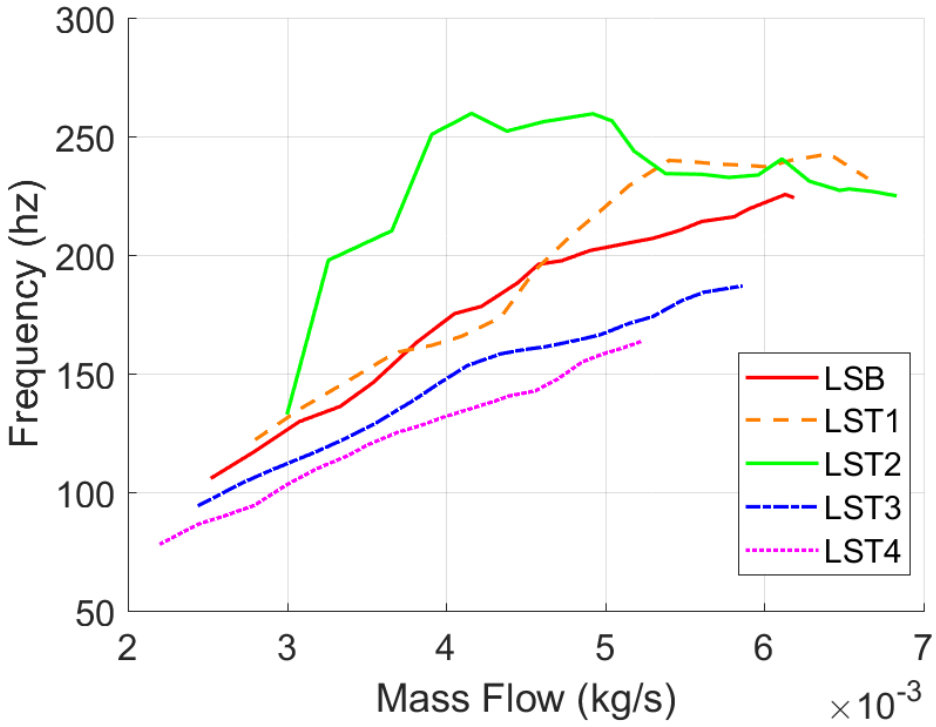

Fig. 3.9 Frequency vs mass flow rate for the large square oscillators with the throat geometry varied by ±10% and ±20%.

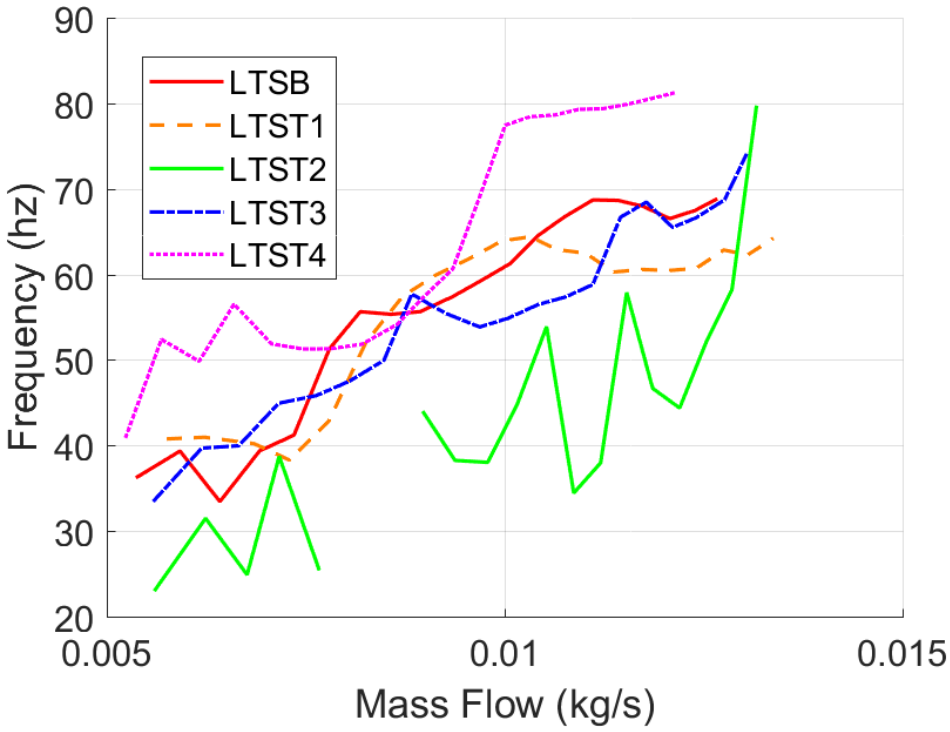

Fig. 3.10 Frequency vs mass flow rate for the large thick square oscillators with the throat geometry varied by ±10% and ±20%.

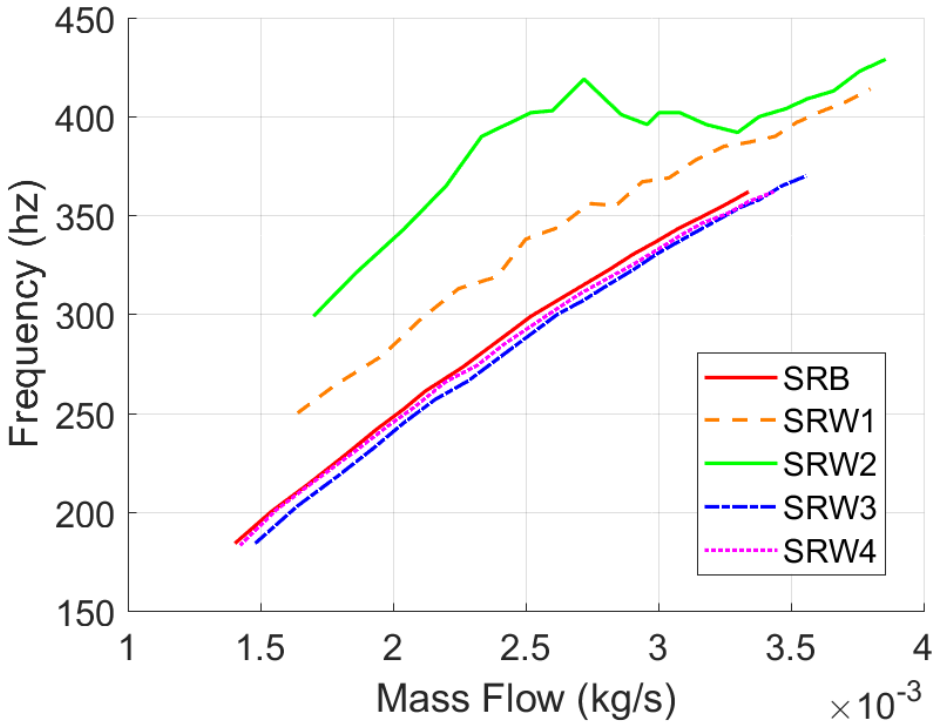

Fig. 3.11 Frequency vs mass flow rate for the small round oscillators with the wedge geometry varied by ±10% and ±20%.

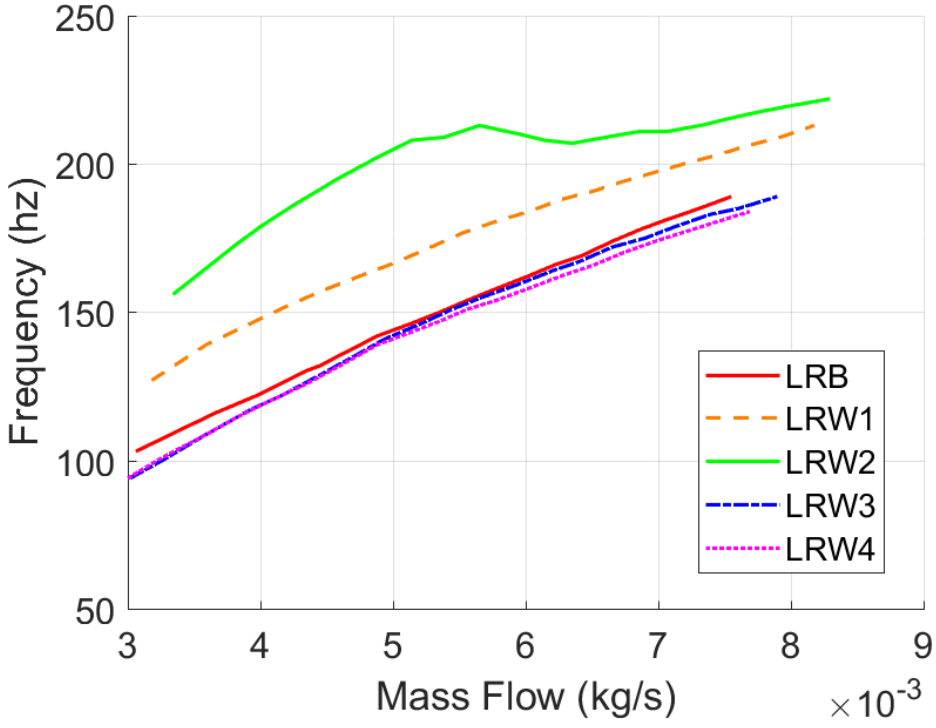

Fig. 3.12 Frequency vs mass flow rate for the large round oscillators with the wedge geometry varied by ±10% and ±20%.

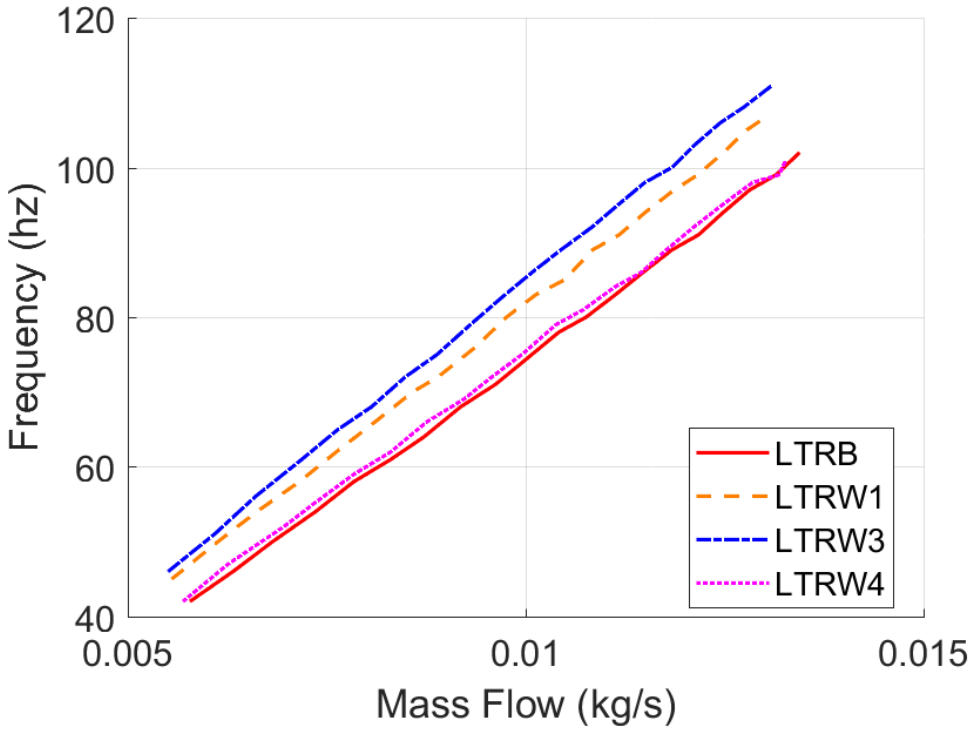

Fig. 3.13 Frequency vs mass flow rate for the large thick round oscillators with the wedge geometry varied by ±10% and ±20%.

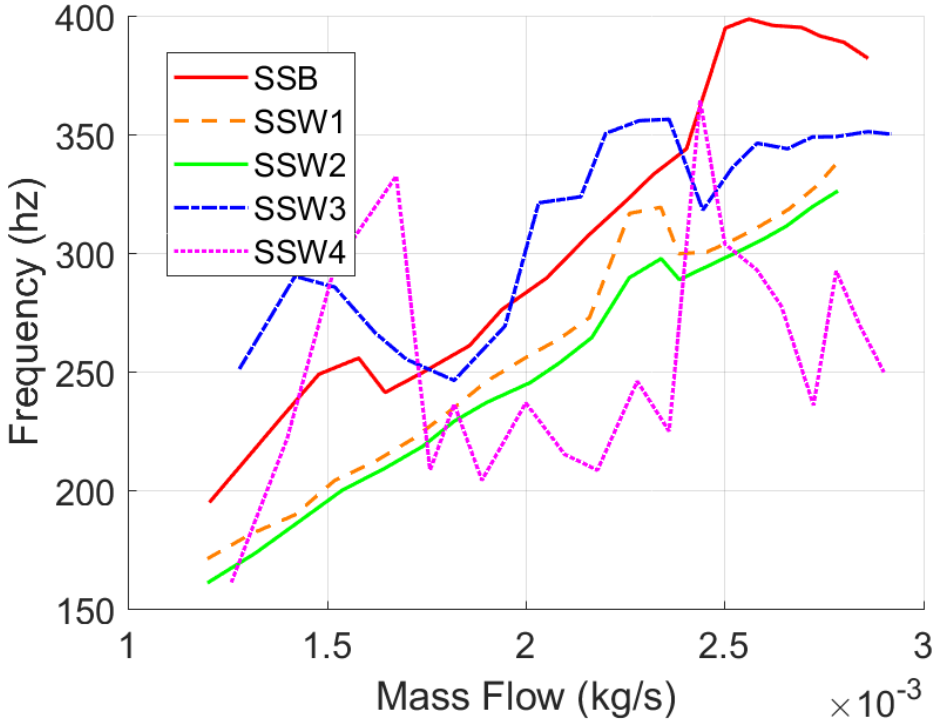

Fig. 3.14 Frequency vs mass flow rate for the small square oscillators with the wedge geometry varied by ±10% and ±20%.

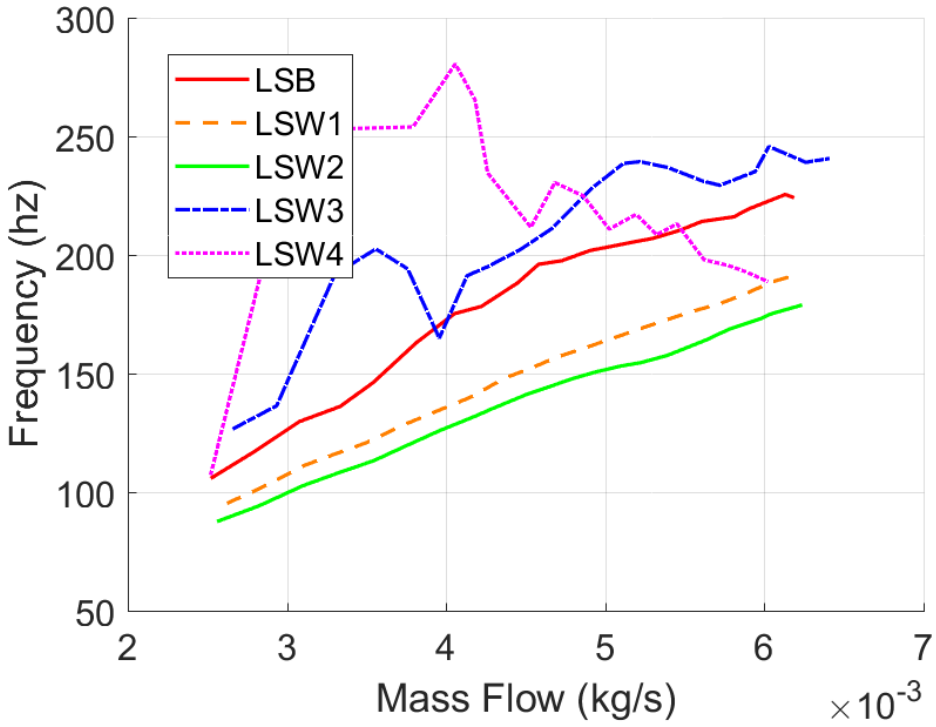

Fig. 3.15 Frequency vs mass flow rate for the large square oscillators with the wedge geometry varied by ±10% and ±20%.

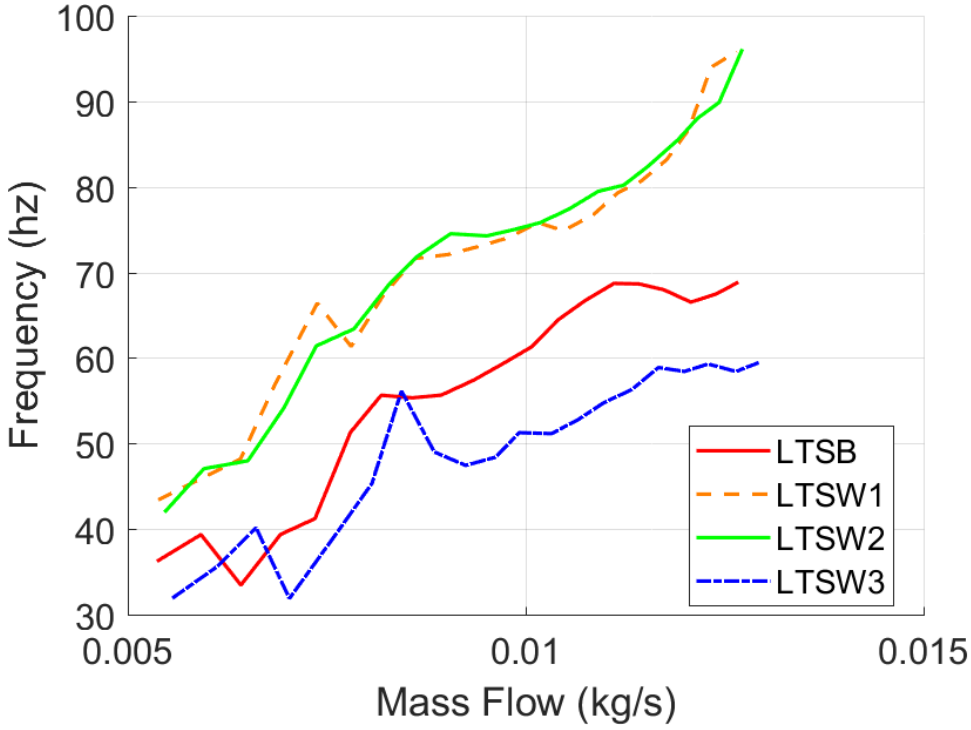

Fig. 3.16 Frequency vs mass flow rate for the large thick square oscillators with the wedge geometry varied by ±10% and ±20%.

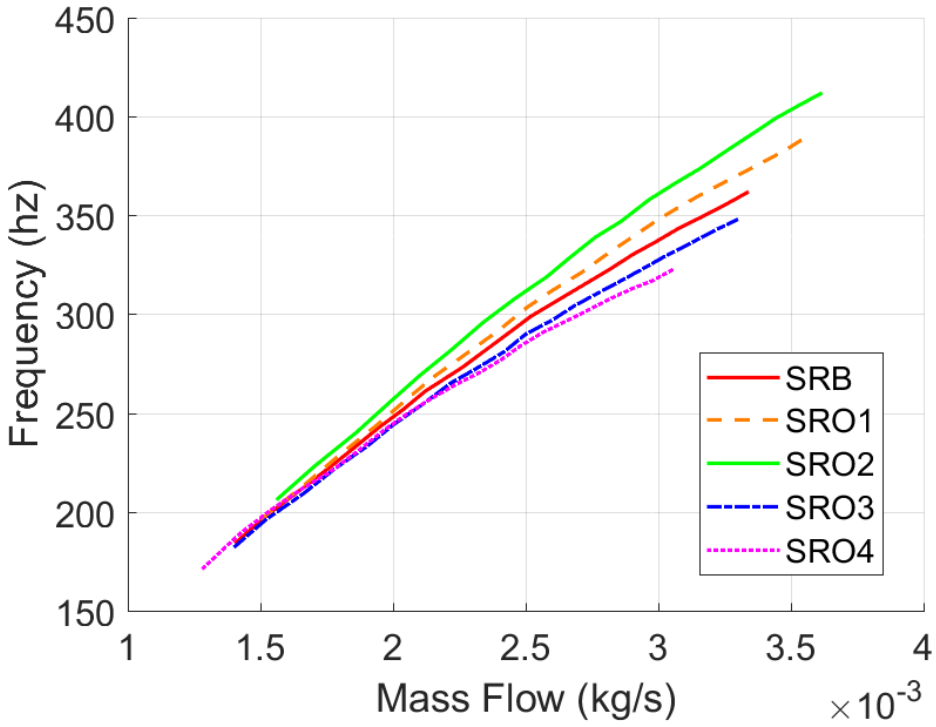

Fig. 3.17 Frequency vs mass flow rate for the small round oscillators with the outlet geometry varied by ±10% and ±20%.

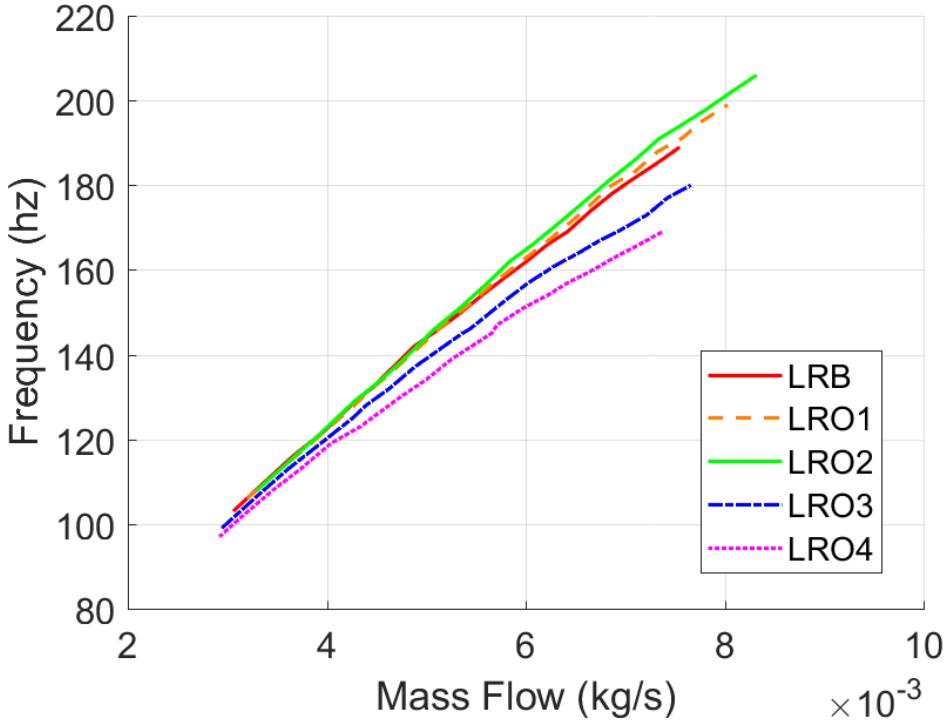

Fig. 3.18 Frequency vs mass flow rate for the large round oscillators with the outlet geometry varied by ±10% and ±20%.

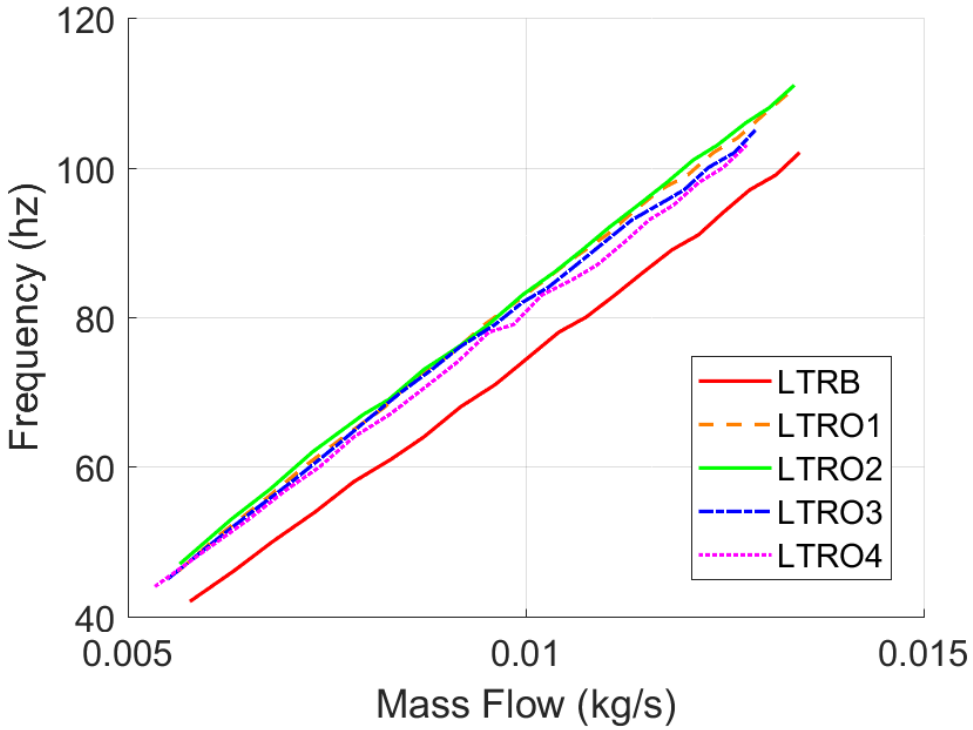

Fig. 3.19 Frequency vs mass flow rate for the large thick round oscillators with the outlet geometry varied by ±10% and ±20%.

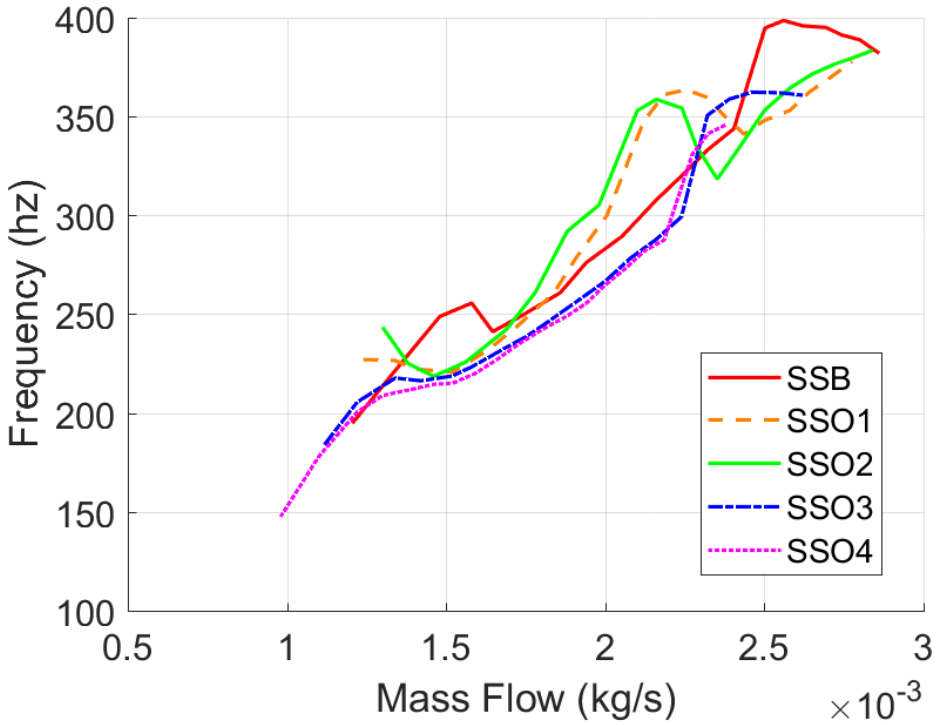

Fig. 3.20 Frequency vs mass flow rate for the small square oscillators with the outlet geometry varied by ±10% and ±20%.

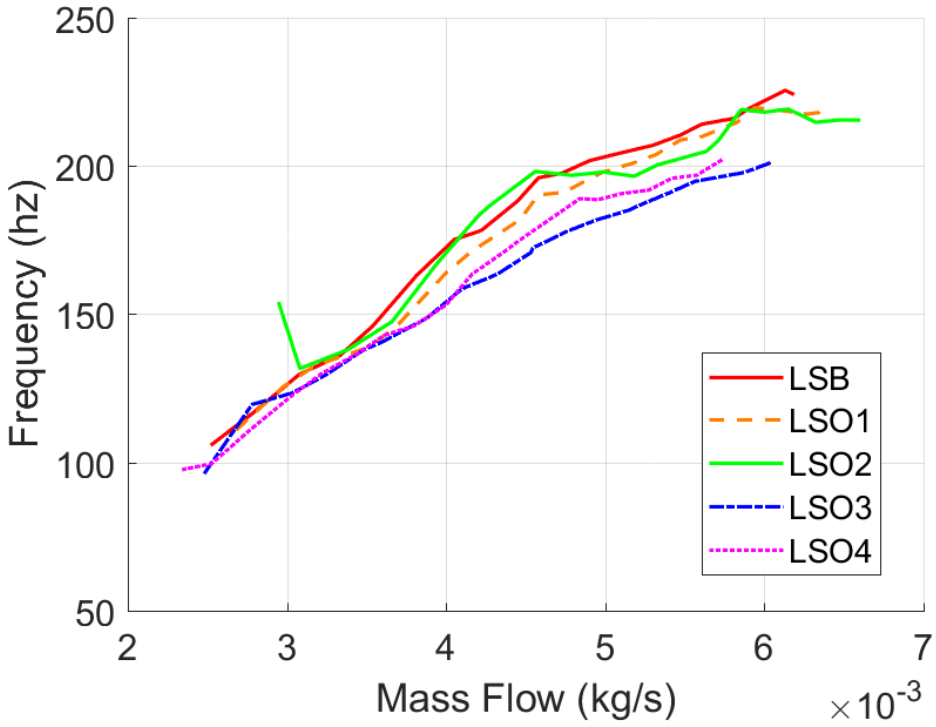

Fig. 3.21 Frequency vs mass flow rate for the large square oscillators with the outlet geometry varied by ±10% and ±20%.

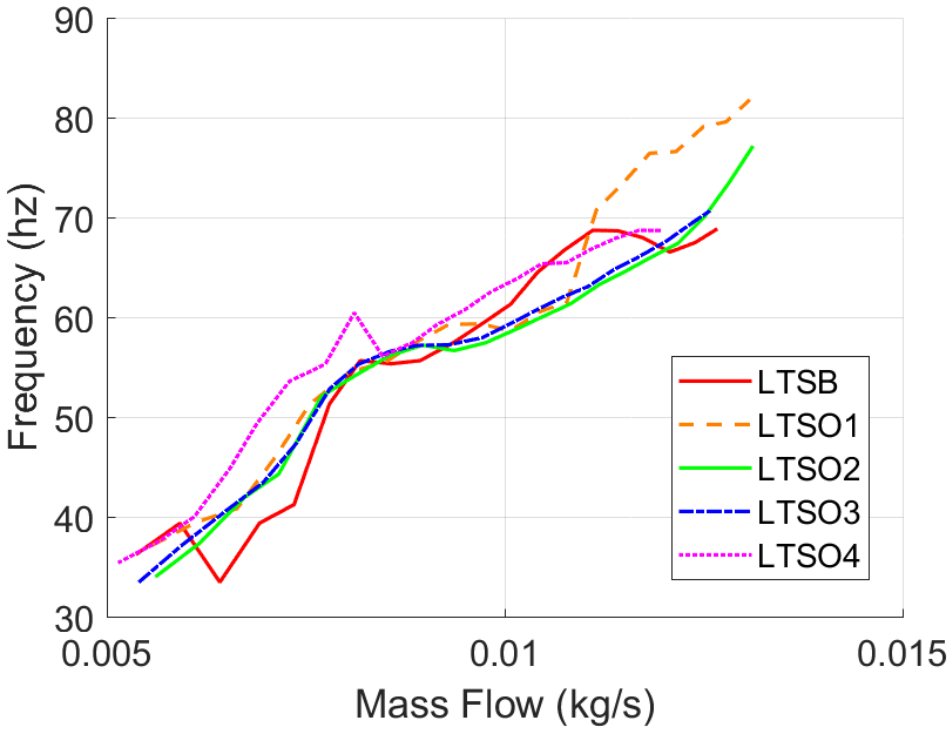

Fig. 3.22 Frequency vs mass flow rate for the large thick round oscillators with the outlet geometry varied by ±10% and ±20%.

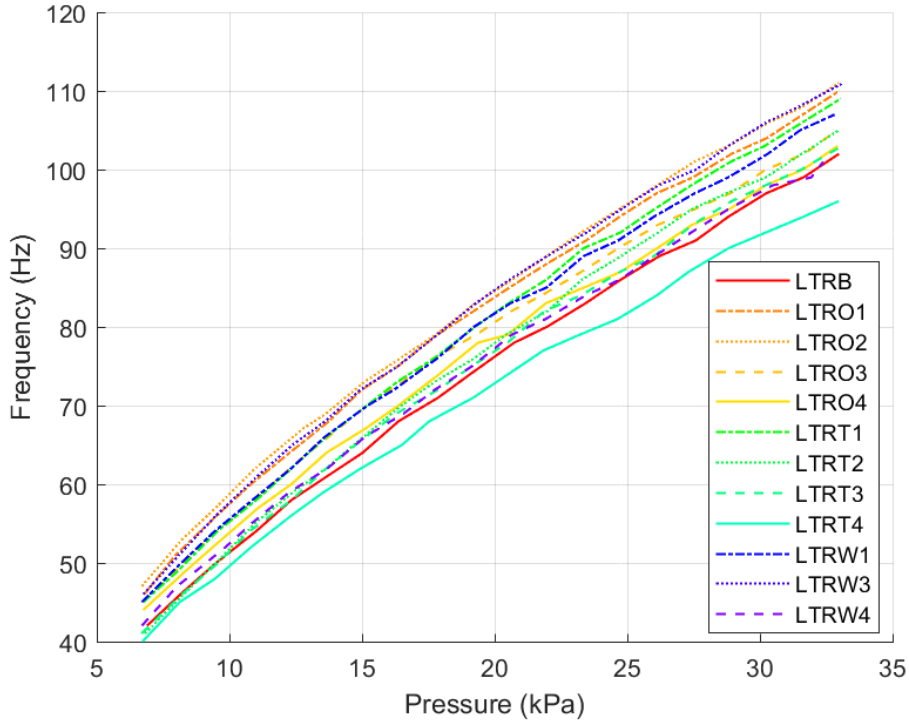

Fig. 3.23 Frequency vs pressure for the large thick round oscillators, AR = 1.

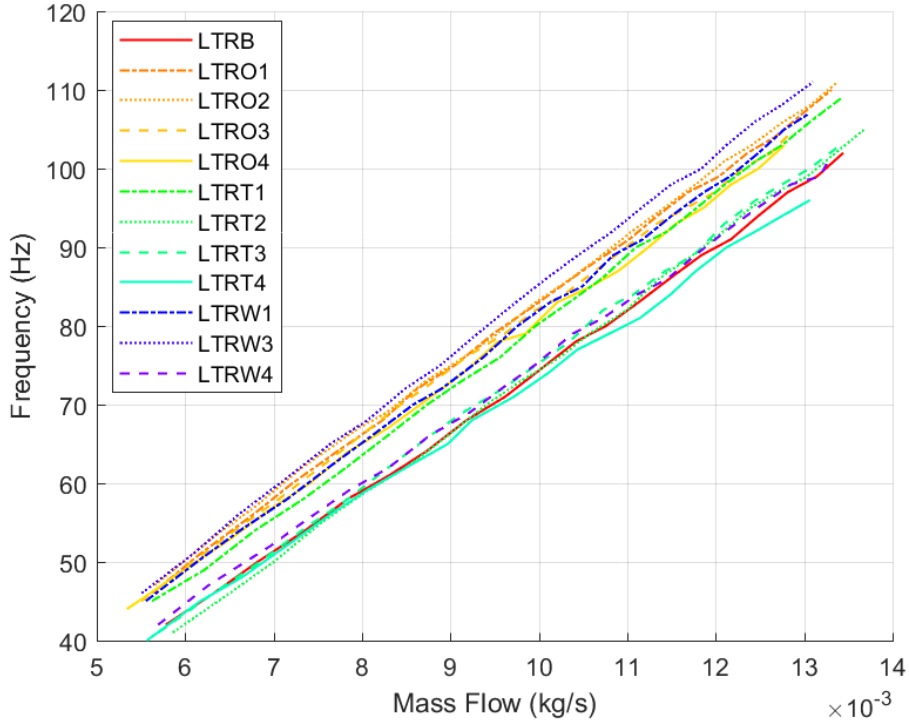

Fig. 3.24 Frequency vs mass flow rate for the large thick round oscillators, AR = 1.

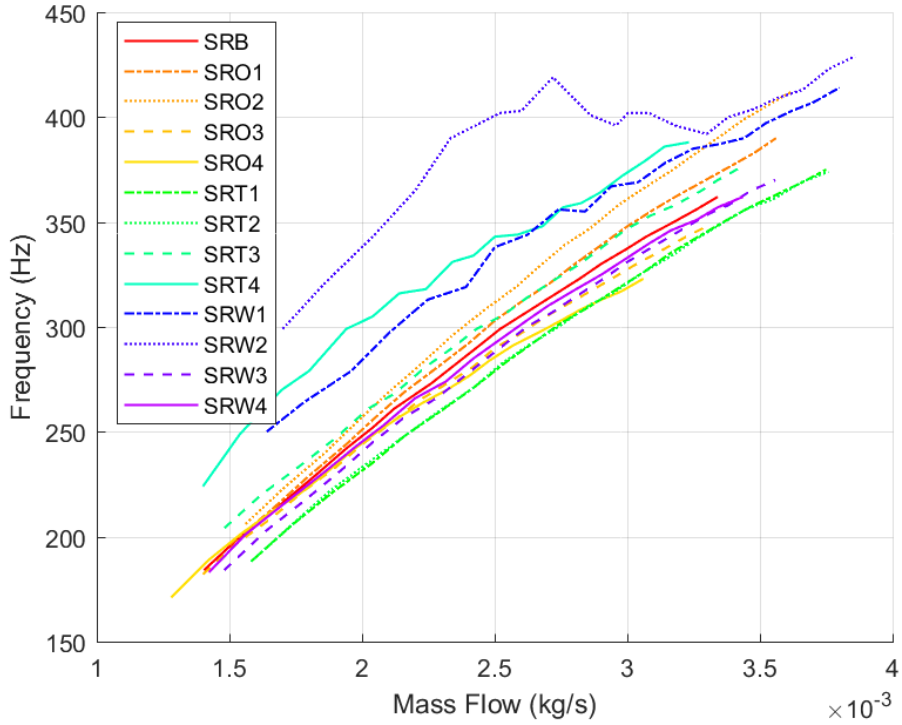

Fig. 3.25 Frequency vs mass flow rate for the small round oscillators, AR = 2.

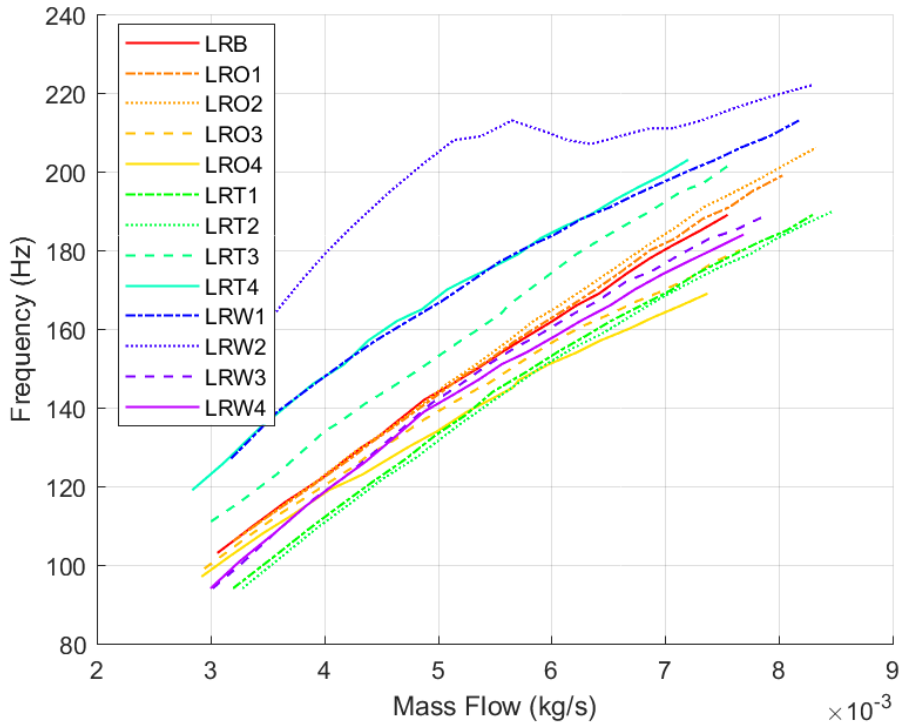

Fig. 3.26 Frequency vs mass flow rate for the large round oscillators, AR = 4.

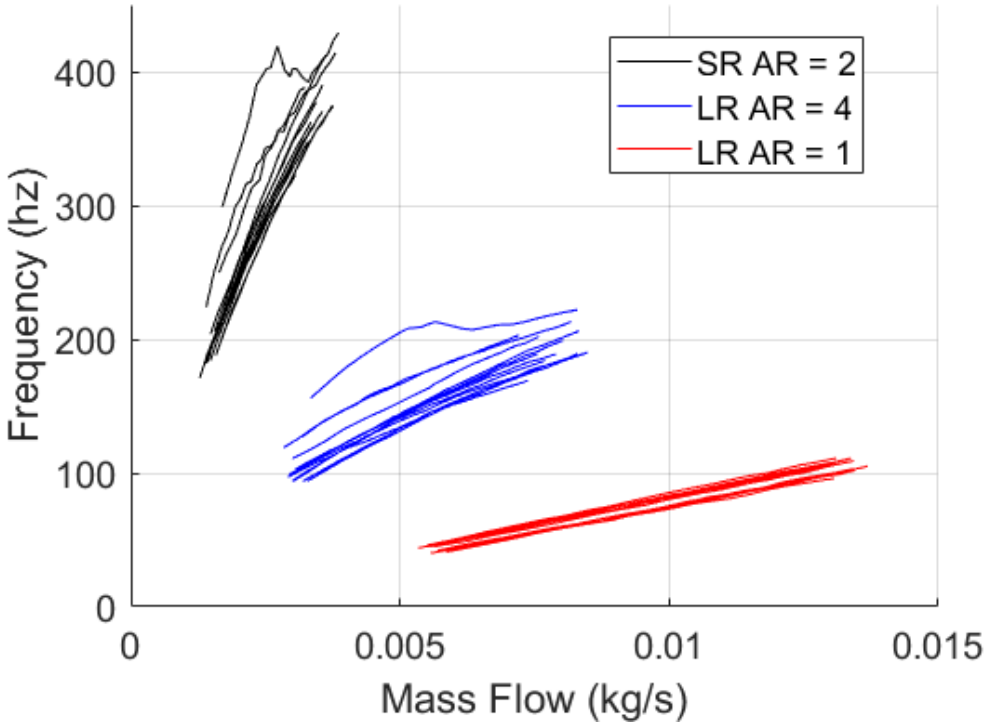

Fig. 3.27 Frequency vs mass flow rate for all round oscillators.

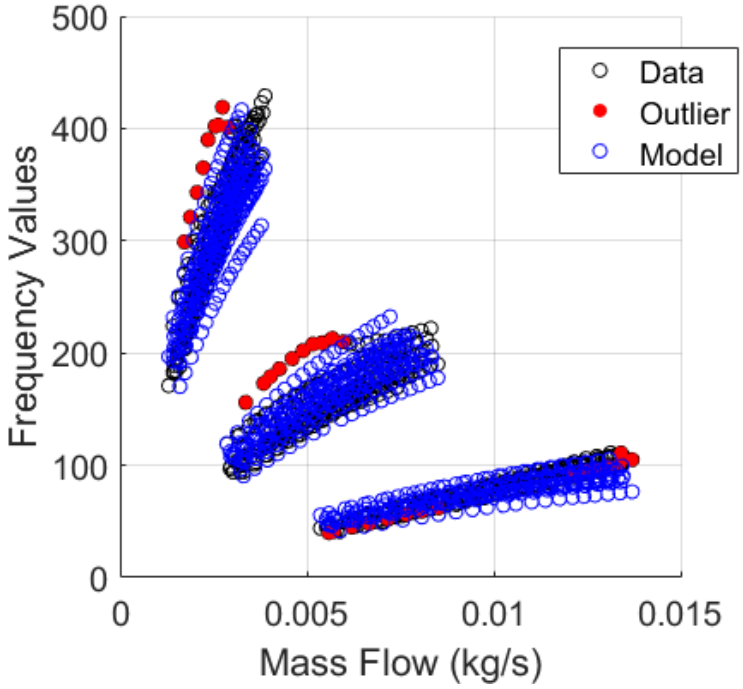

Fig. 3.28 Non-Linear model results compared to recorded data.

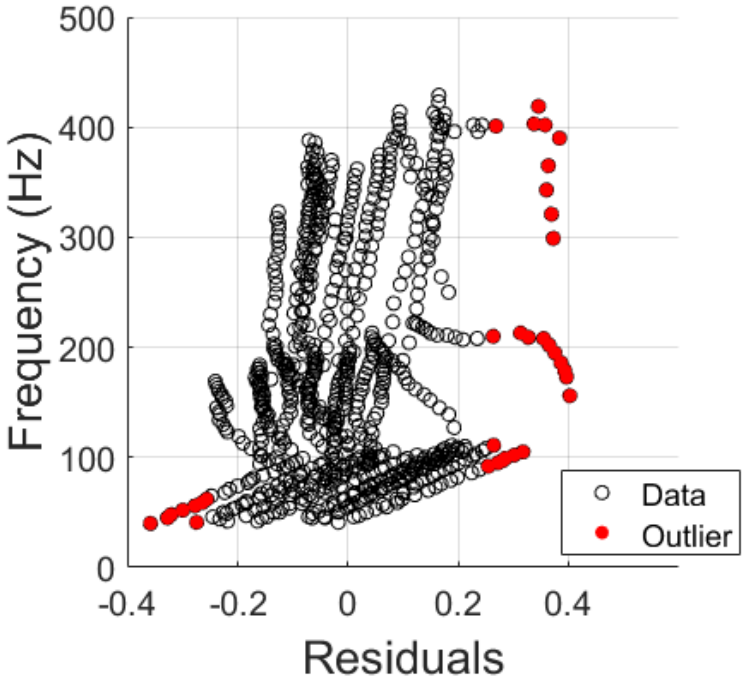

Fig. 3.29 Non-Linear model residuals at 5% confidence level

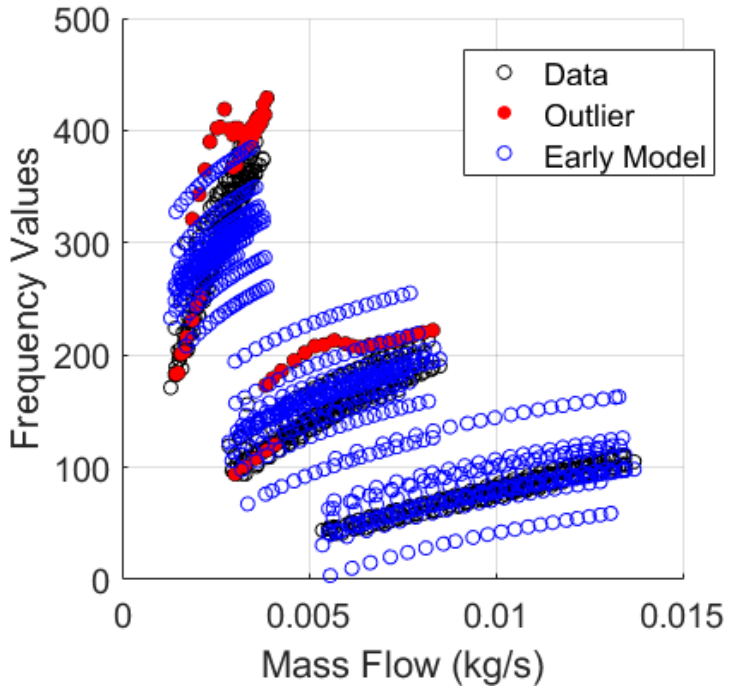

Fig. 3.30 Early model results compared to recorded data

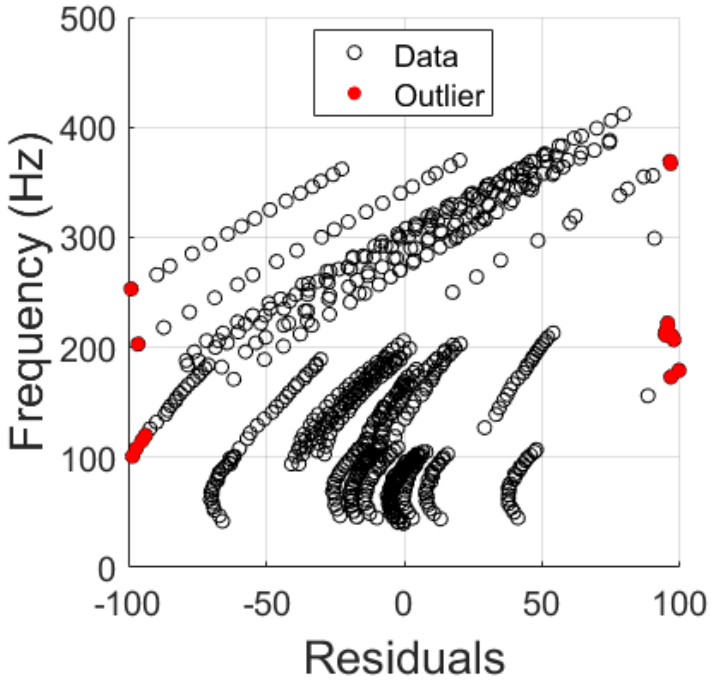

Fig. 3.31 Early model residuals at 5% confidence level

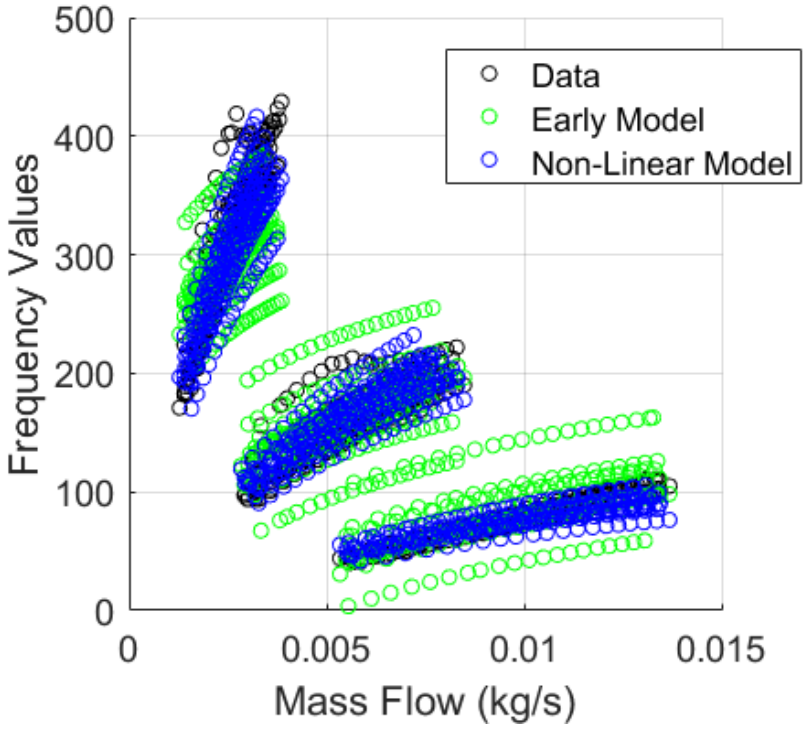

Fig. 3.32 Comparison of the early model and non-linear model to the collected data

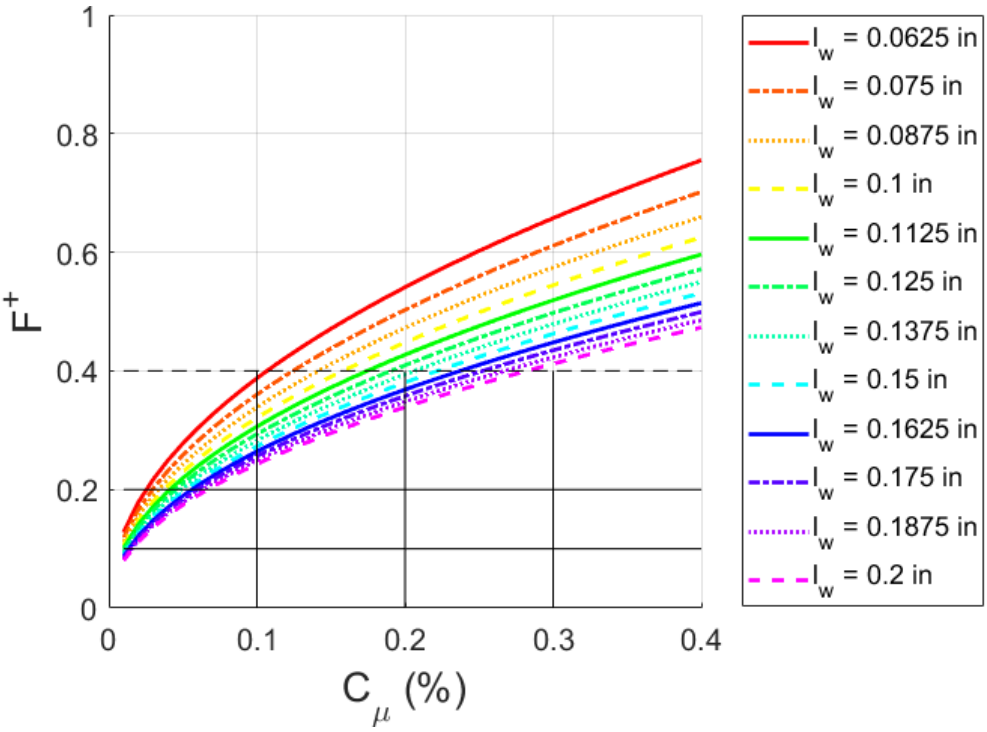

Fig. 3.33 Carpet plot comparing F^+ vs C_μ vs l_w for $\alpha = 0°$ and $\delta_t = 0°$ and $n = 28$ oscillators

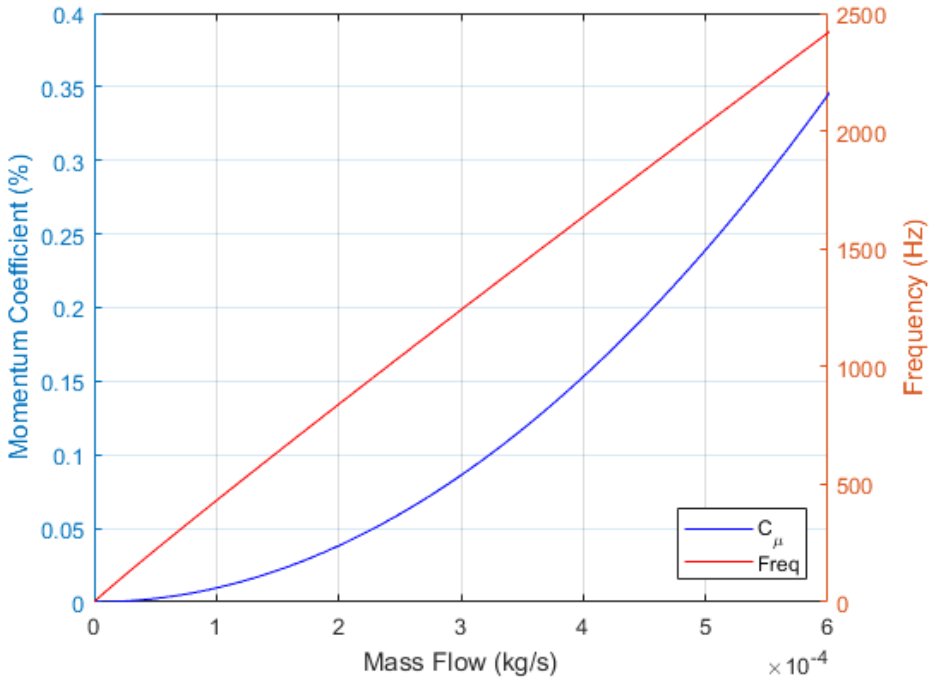

Fig. 3.34 C_μ and f vs $\dot{m}$ for the embedded oscillators using the non-linear frequency model

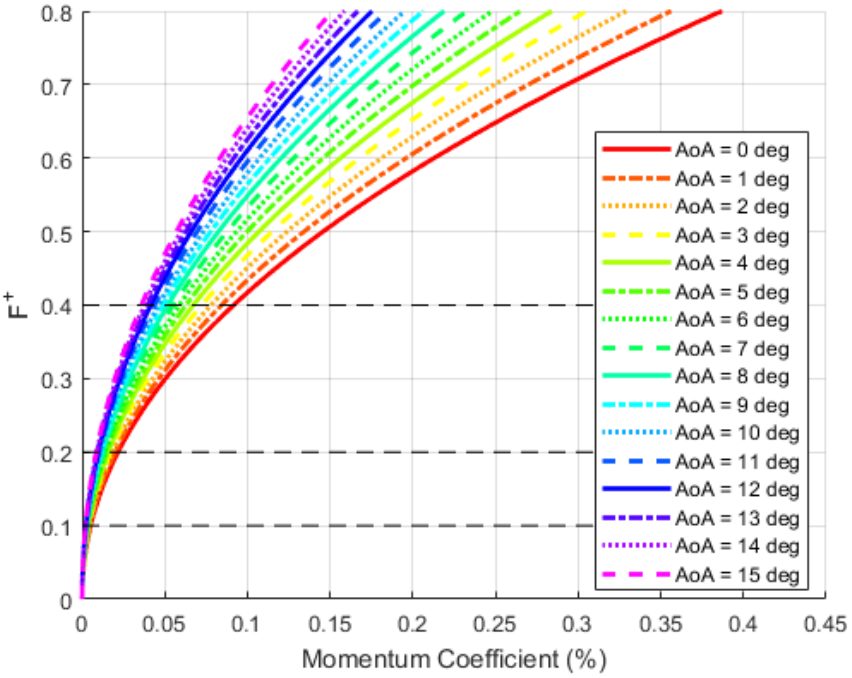

Fig. 3.35 Carpet plot of C_μ vs F^+ at various α for a $\delta_f = 0°$ for the non-linear frequency model

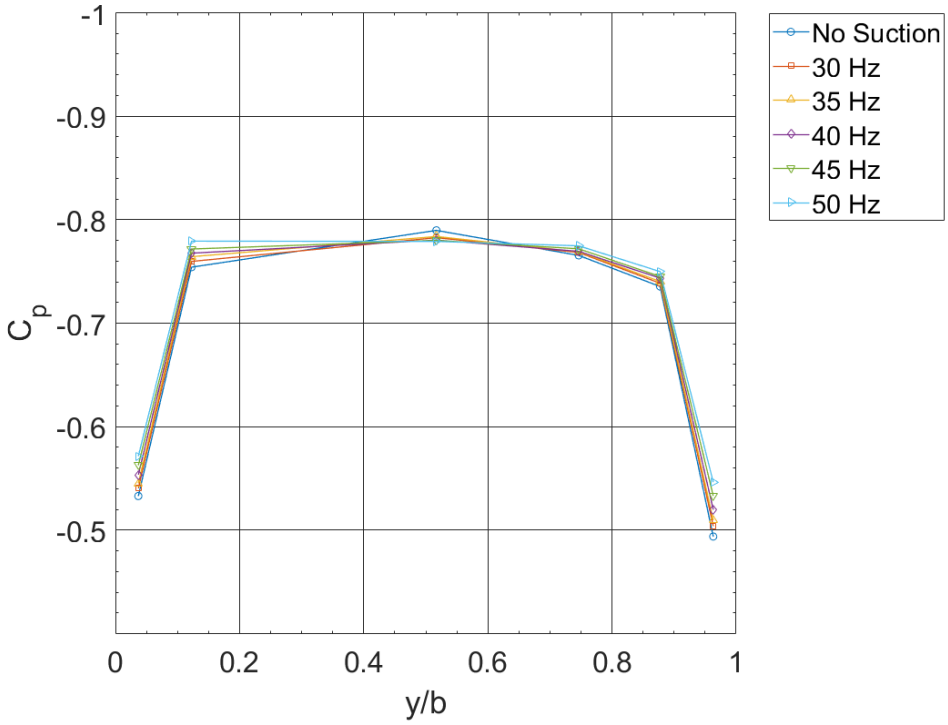

Fig. 3.36 Spanwise pressure distribution for the S414 configuration at $\alpha = 5°$ and various VFD settings for applied suction

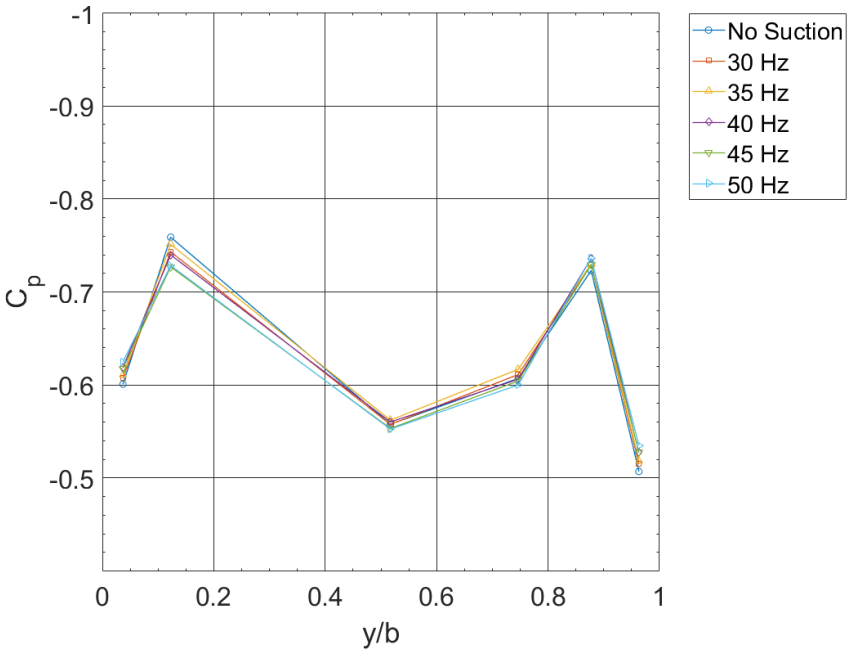

Fig. 3.37 Spanwise pressure distribution for the S414 configuration at $\alpha = 15°$ and various VFD settings for applied suction

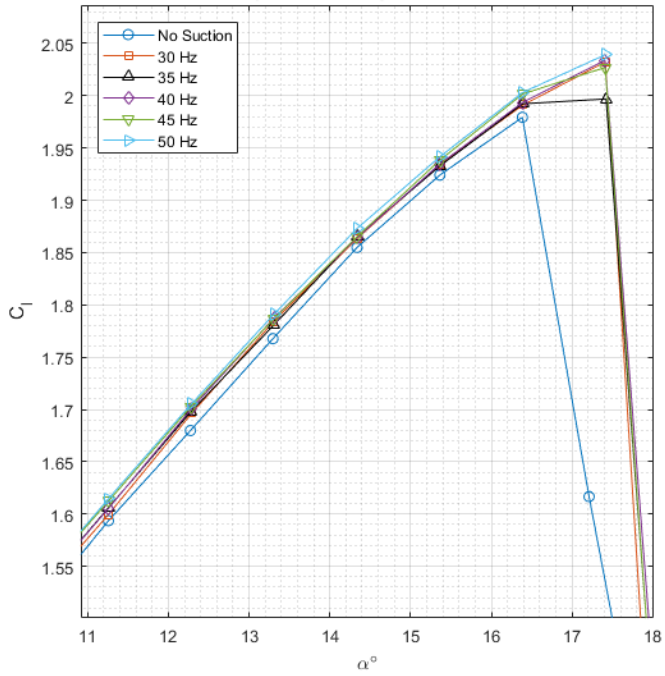

Fig. 3.38 Lift curves for the S414 configuration with $\delta_f = 0°$ at various VFD settings for the applied suction

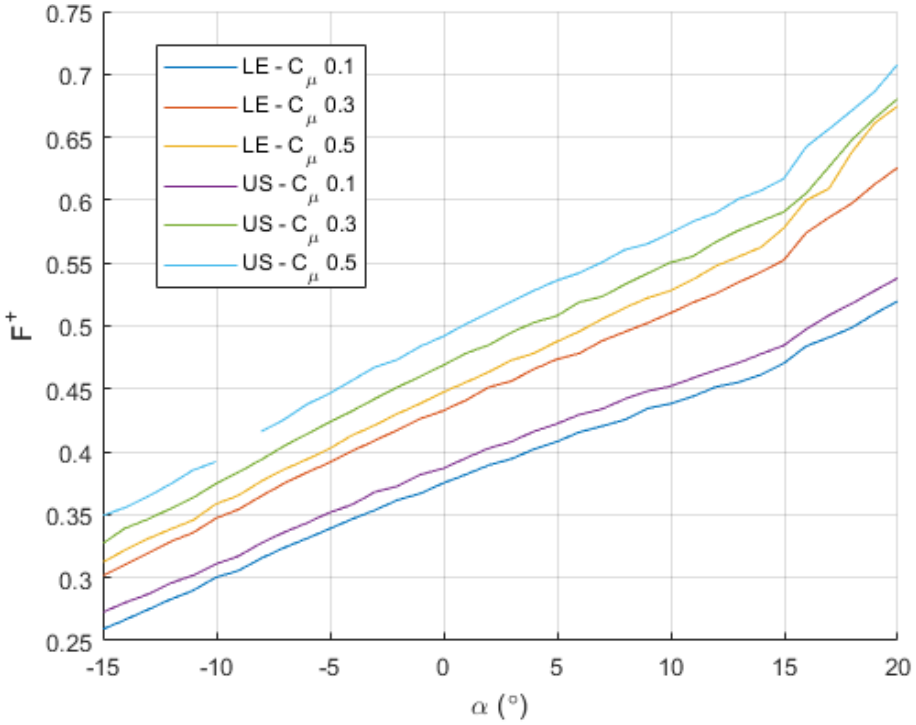

Fig. 3.39 F^+ vs α as recorded for HLC at a $\delta_t = 0°$

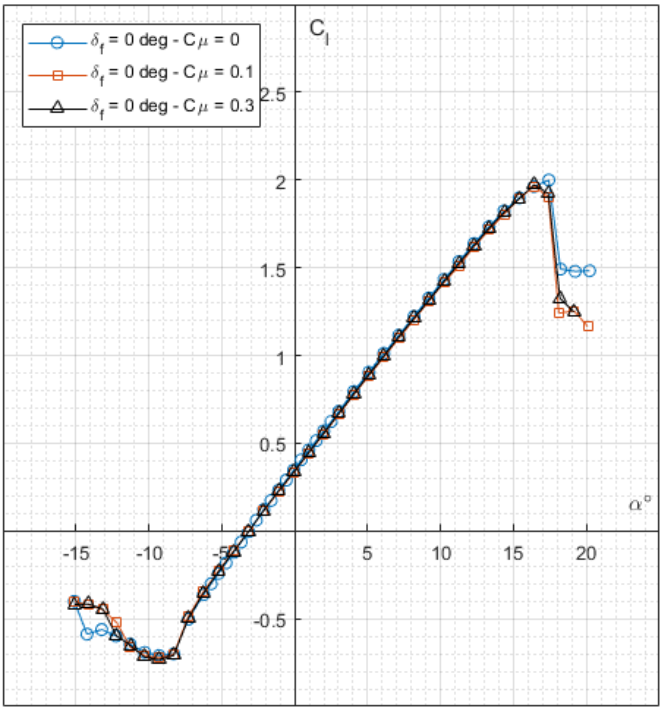

Fig. 3.40 Lift polar for S414 Configuration with $\delta_f = 0°$ for the leading edge oscillators

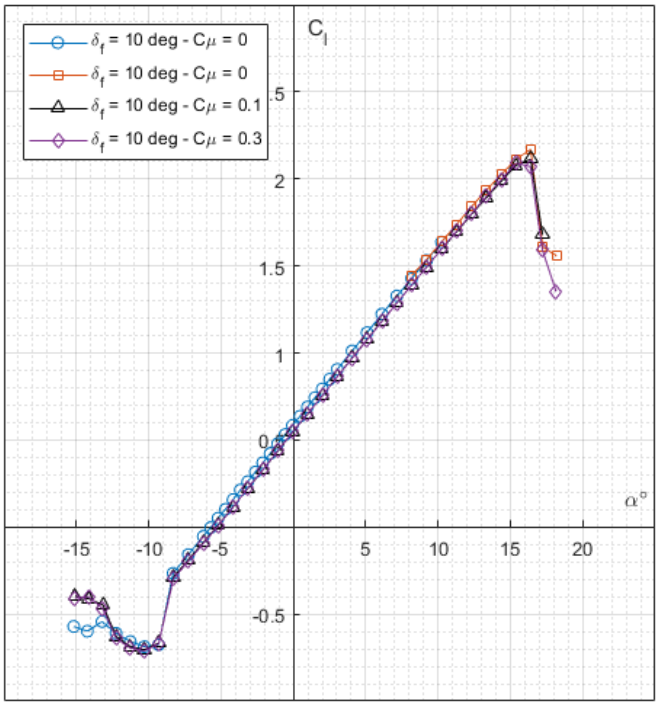

Fig. 3.41 Lift polar for S414 Configuration with $\delta_f = 10°$ for the leading edge oscillators

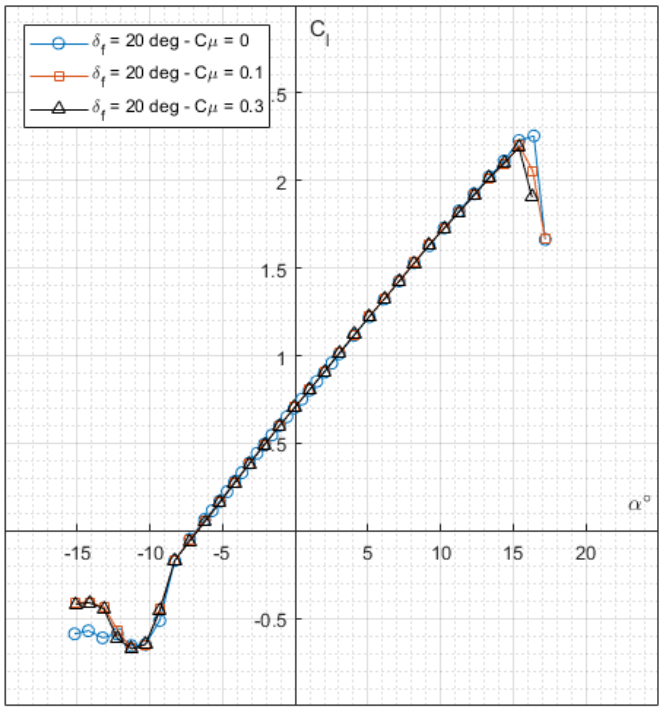

Fig. 3.42 Lift polar for S414 Configuration with $\delta_f = 20°$ for the leading edge oscillators

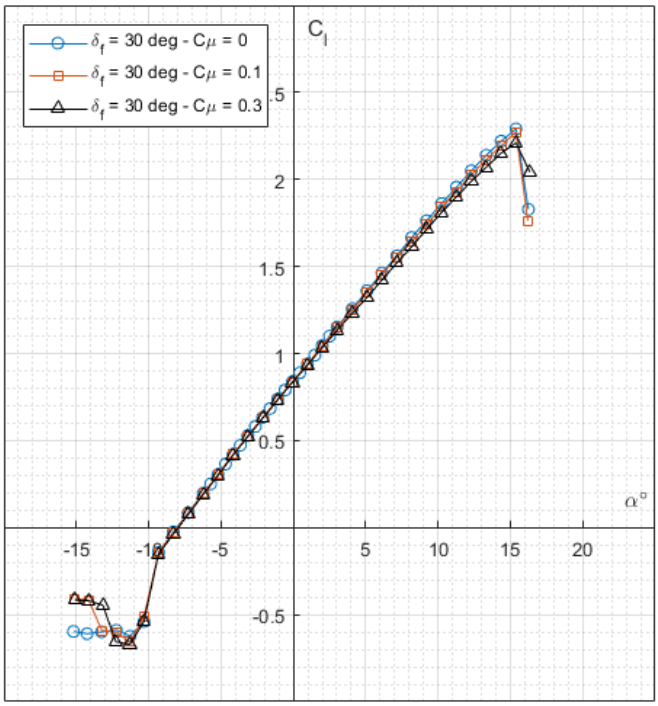

Fig. 3.43 Lift polar for S414 Configuration with $\delta_f = 30°$ for the leading edge oscillators

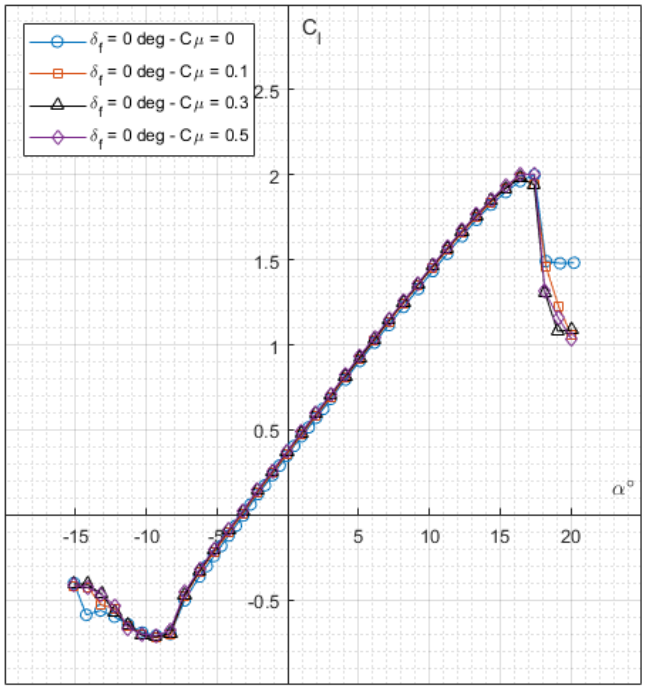

Fig. 3.44 Lift polar for S414 Configuration with $\delta_f = 0°$ for the upper surface oscillators

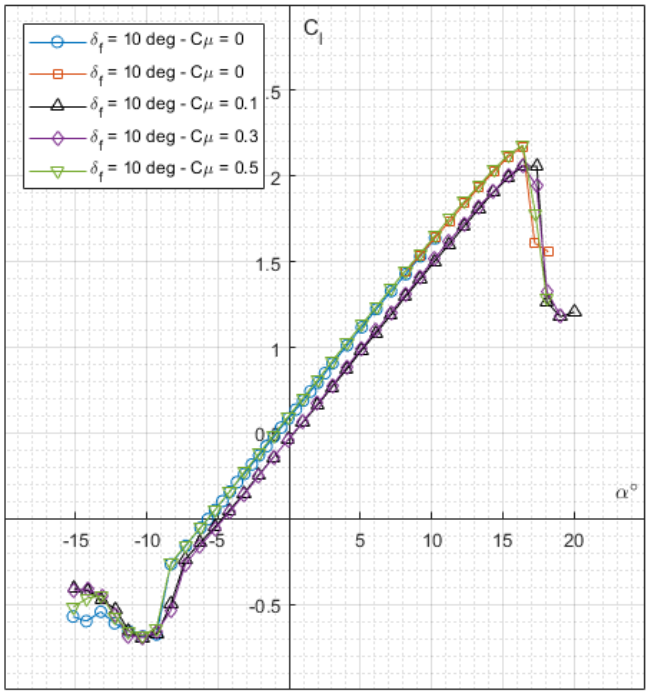

Fig. 3.45 Lift polar for S414 Configuration with $\delta_f = 10°$ for the upper surface oscillators

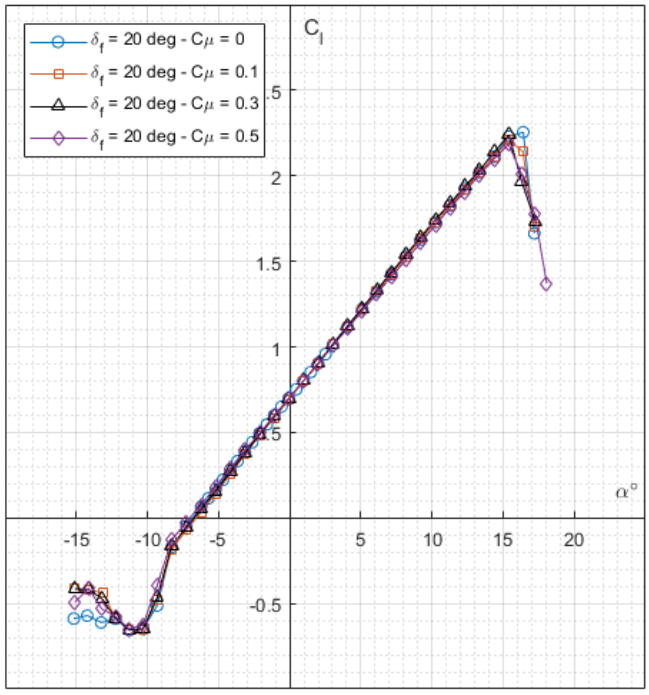

Fig. 3.46 Lift polar for S414 Configuration with $\delta_f = 20°$ for the upper surface oscillators

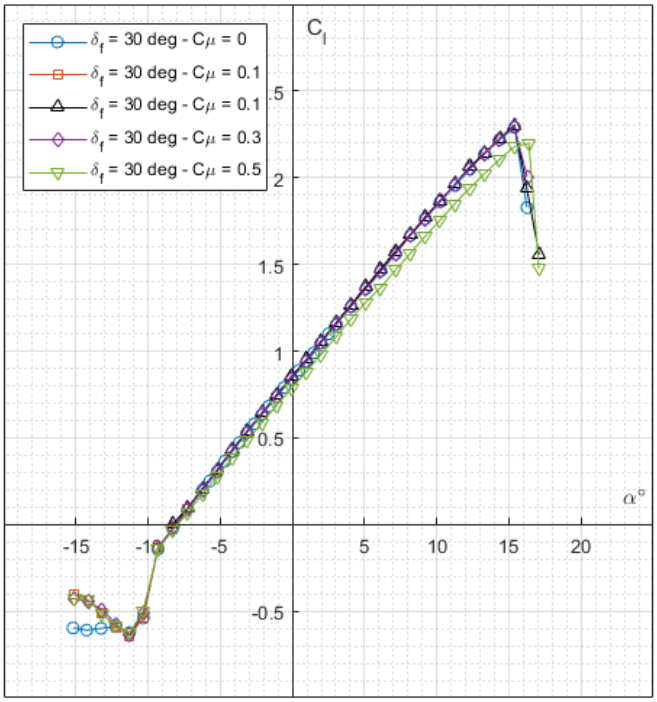

Fig. 3.47 Lift polar for S414 Configuration with $\delta_f = 30°$ for the upper surface oscillators

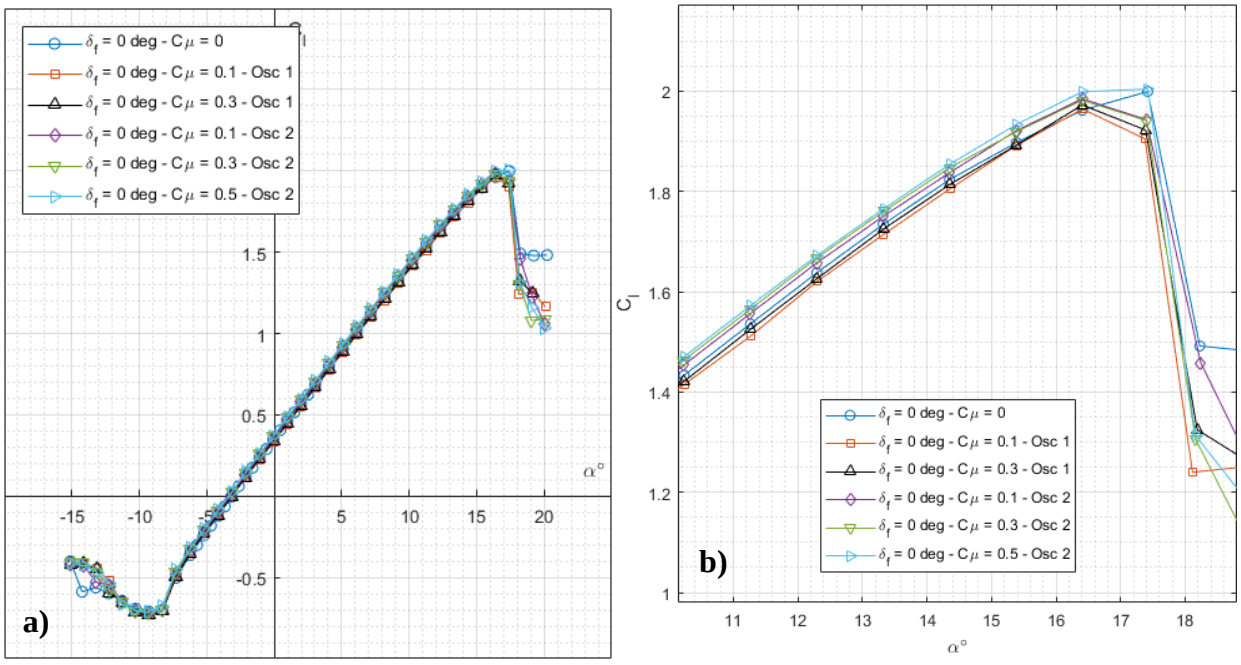

Fig. 3.48 Lift polar for S414 Configuration with $\delta_f = 0°$ for all oscillators. (left) full polar (right) positive α stall

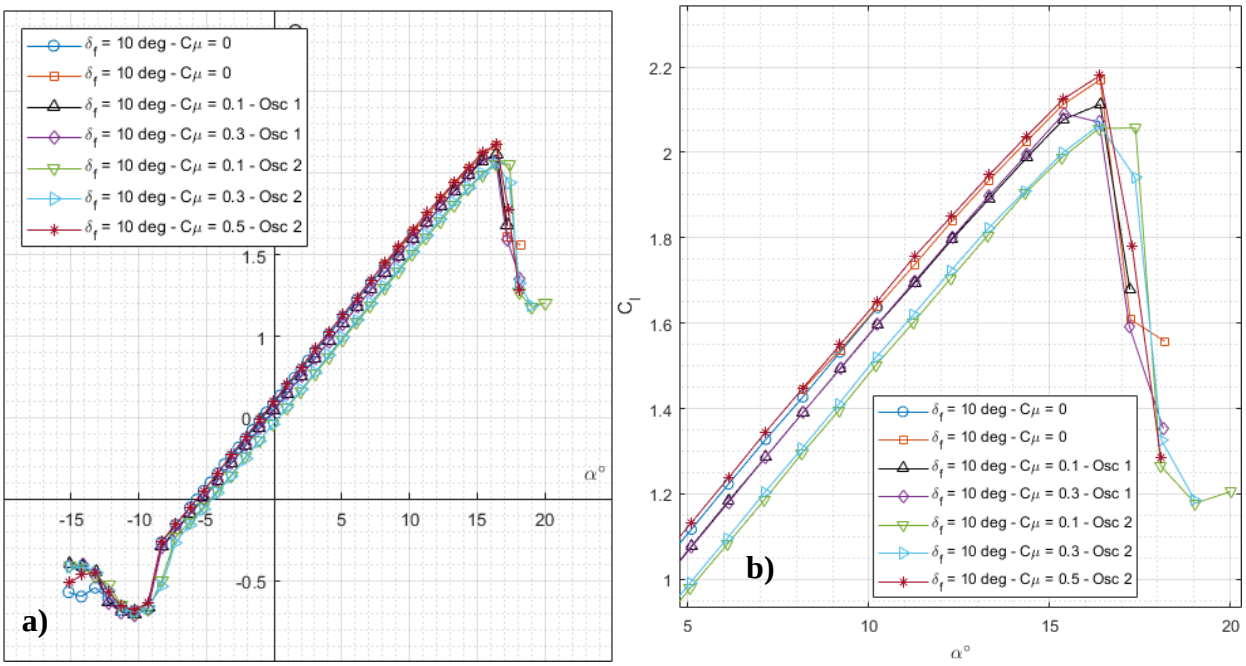

Fig. 3.49 Lift polar for S414 Configuration with $\delta_f = 10°$ for all oscillators. (left) full polar (right) positive α stall

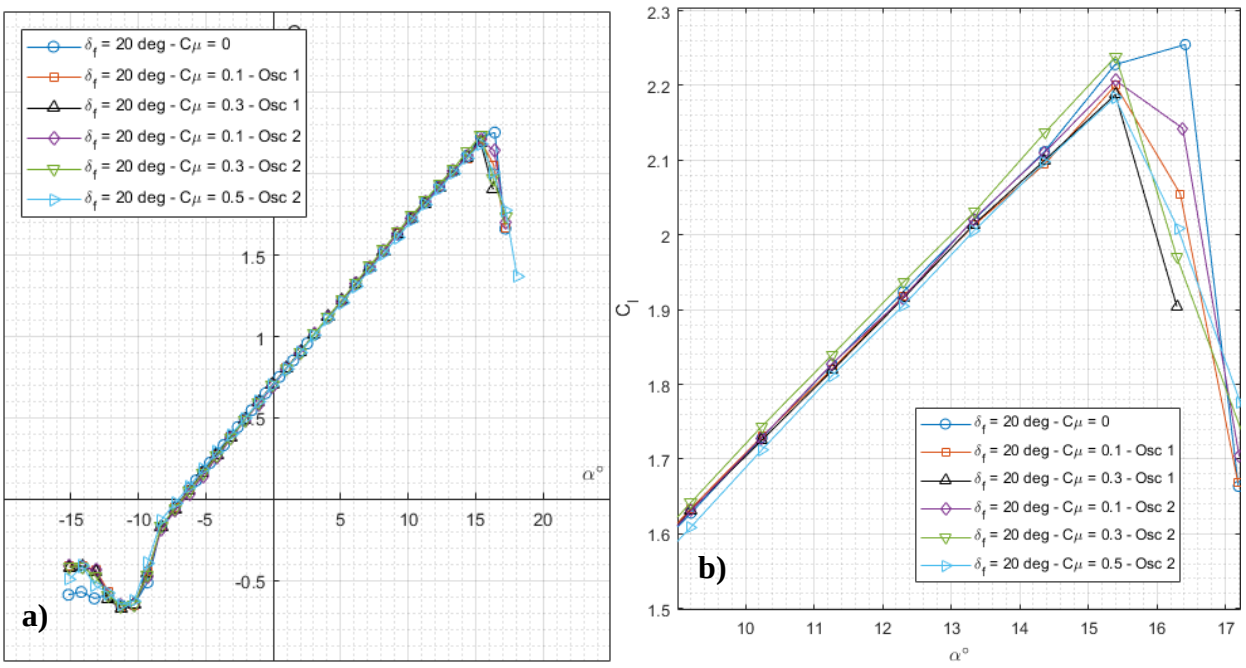

Fig. 3.50 Lift polar for S414 Configuration with $\delta_f = 20°$ for all oscillators. (left) full polar (right) positive α stall

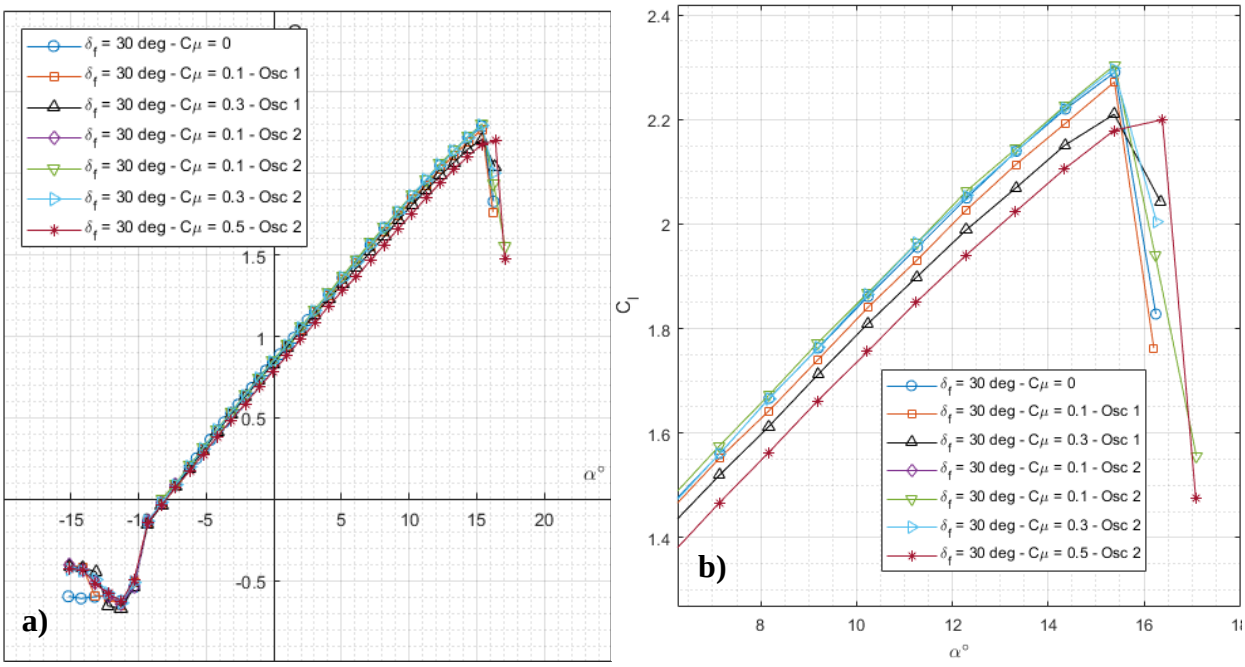

Fig. 3.51 Lift polar for S414 Configuration with $\delta_f = 30°$ for all oscillators. (left) full polar (right) positive α stall

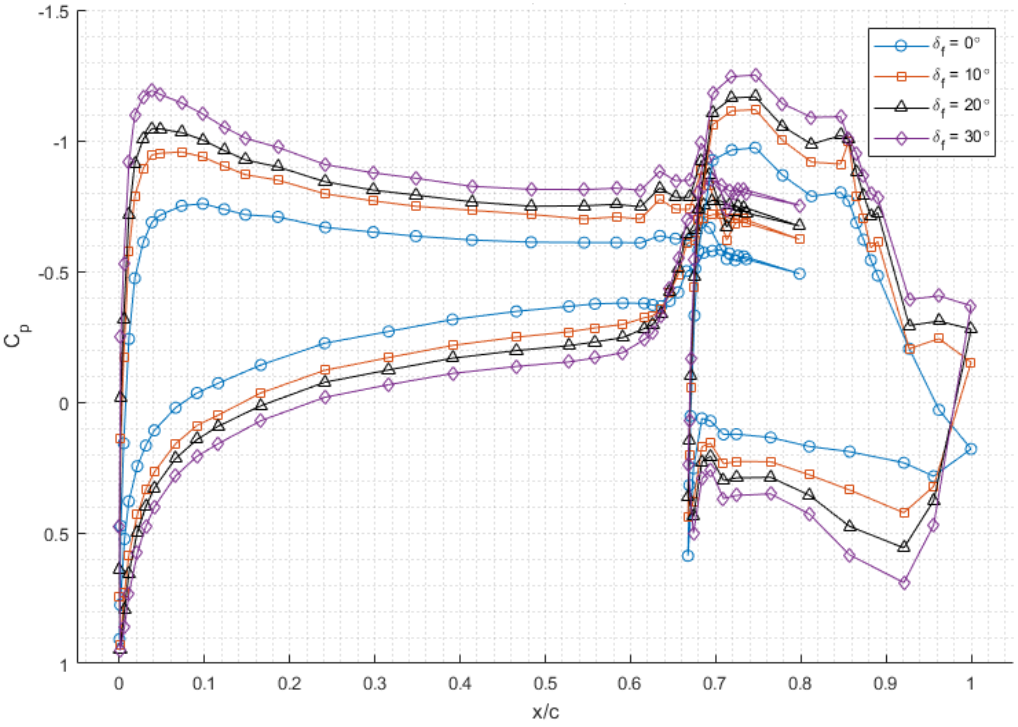

Fig. 3.52 C_p distributions for each δ_f at Re = 1.8e6, M = 0.18, and $\alpha = 1°$ with no actuation for the S414 Configuration

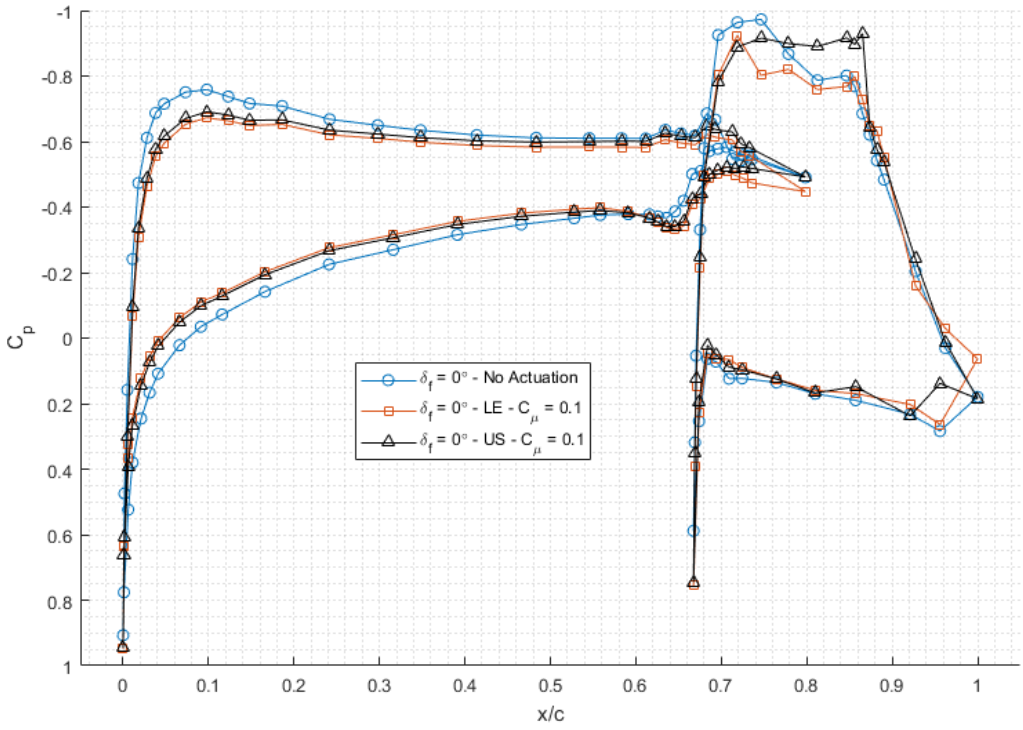

Fig. 3.53 C_p distributions for $\delta_f = 0°$ at Re = 1.8e6, M = 0.18, and $\alpha = 1°$ comparing each oscillator set for the S414 Configuration

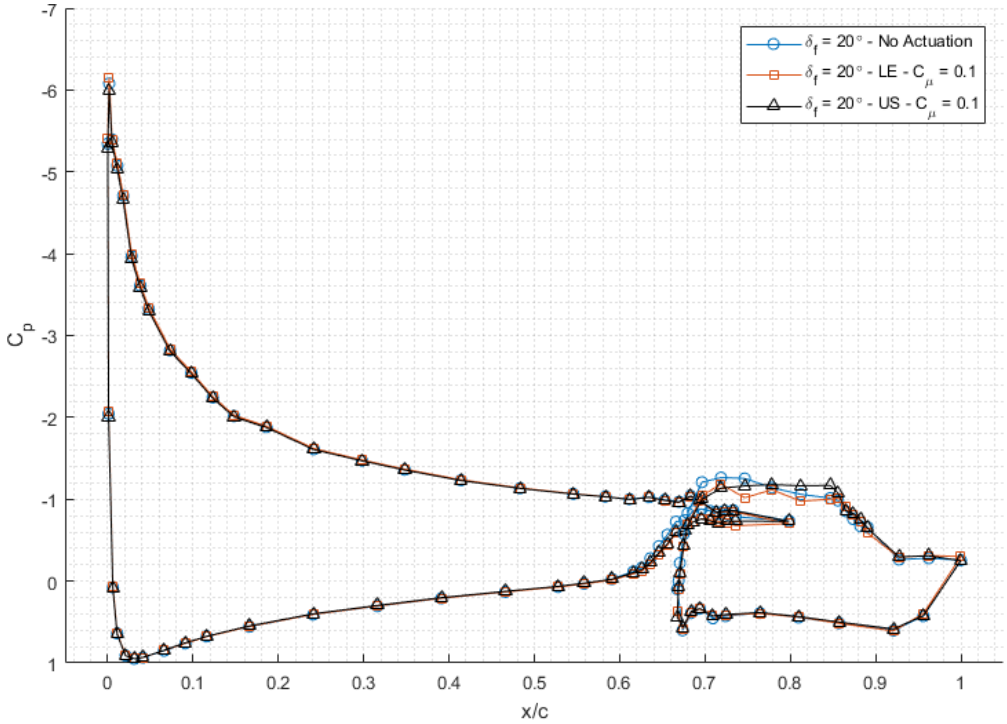

Fig. 3.54 C_p distributions for $\delta_f = 20°$ at Re = 1.8e6, M = 0.18, and $\alpha = 10°$ showing the separation over the deflected flap.

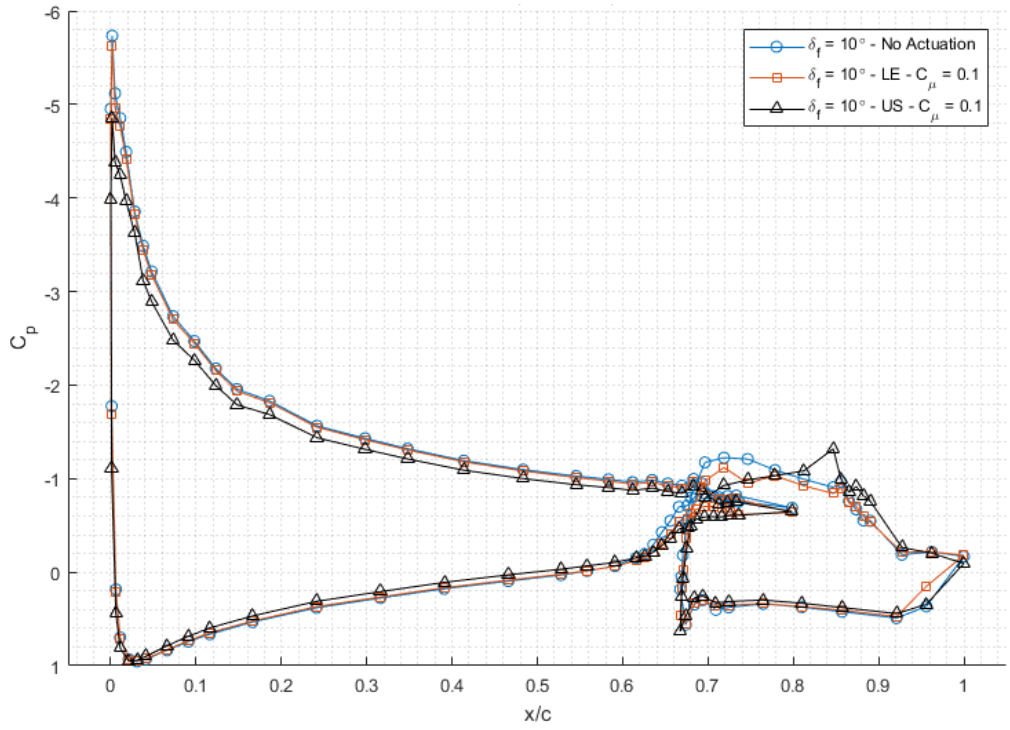

Fig. 3.55 C_p distributions for $\delta_f = 10°$ at Re = 1.8e6, M = 0.18, and $\alpha = 10°$ showing the separation over the deflected flap with some alleviation due to upper surface actuation

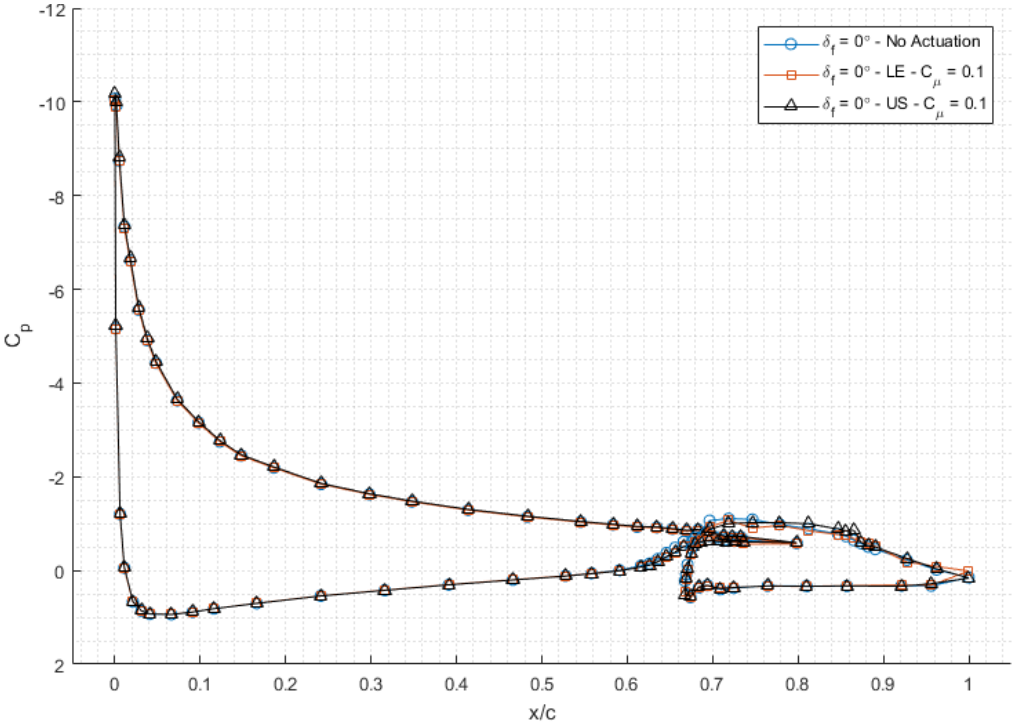

Fig. 3.56 C_p distributions for $\delta_f = 0°$ at Re = 1.8e6, M = 0.18, and $\alpha = 15°$ showing the influence of actuation at higher α.

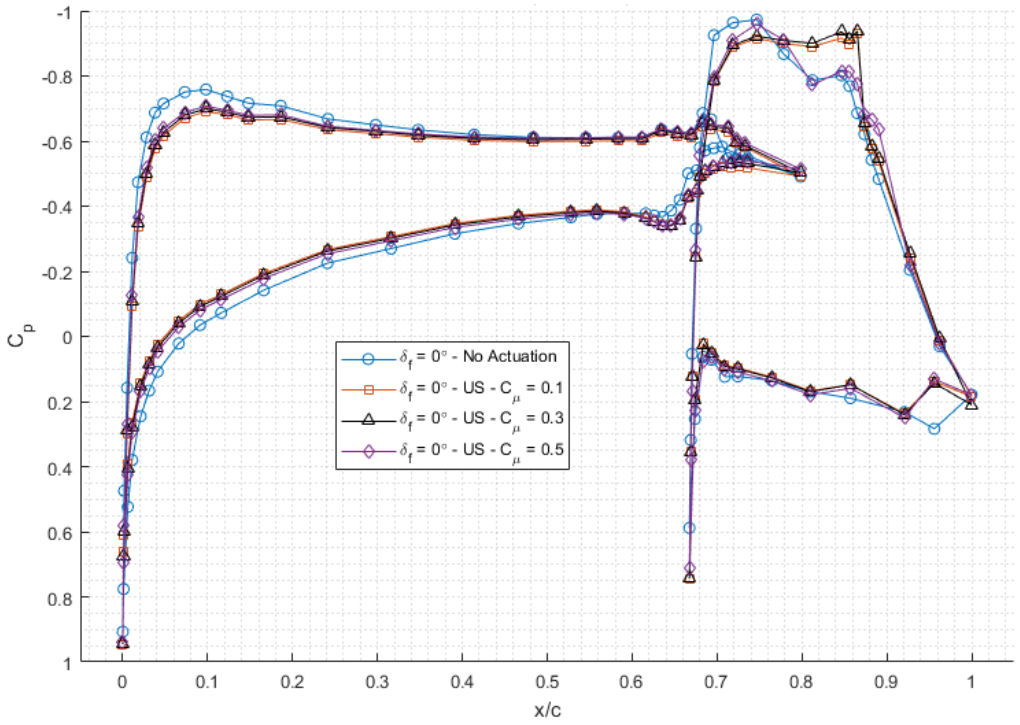

Fig. 3.57 C_p distributions for $\delta_f = 0°$ at Re = 1.8e6, M = 0.18, and $\alpha = 1°$ comparing the upper surface oscillators at various C_μ

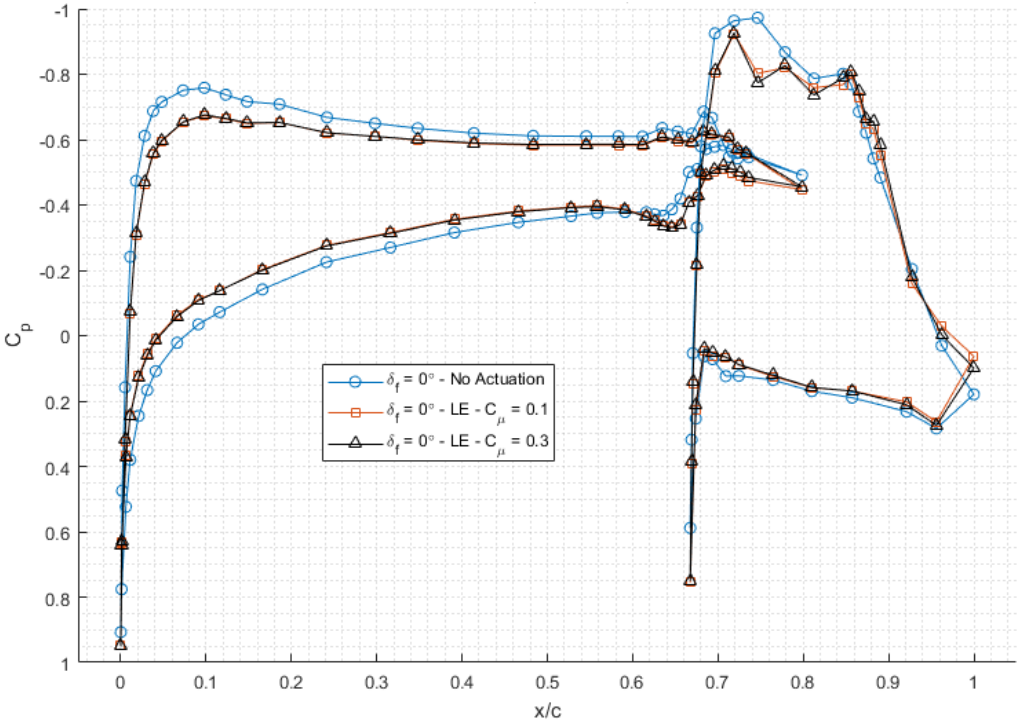

Fig. 3.58 C_p distributions for $\delta_f = 0°$ at Re = 1.8e6, M = 0.18, and $\alpha = 1°$ comparing the leading edge oscillators at various C_μ

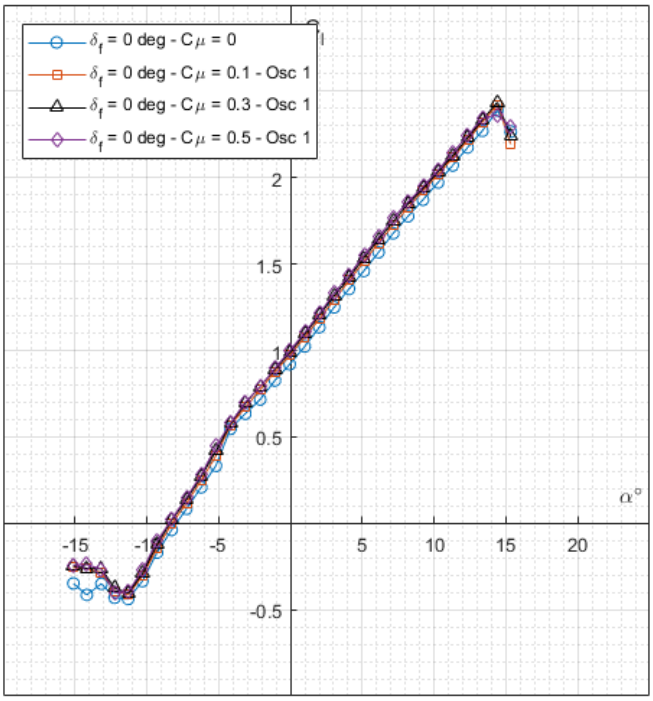

Fig. 3.59 Lift polar for the HLC with $\delta_f = 0°$ for the leading edge oscillators

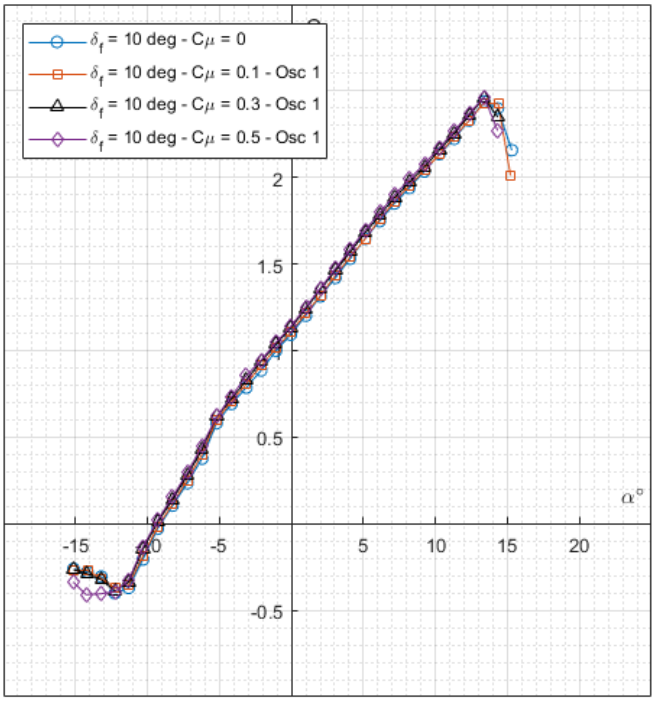

Fig. 3.60 Lift polar for the HLC with $\delta_f = 10°$ for the leading edge oscillators

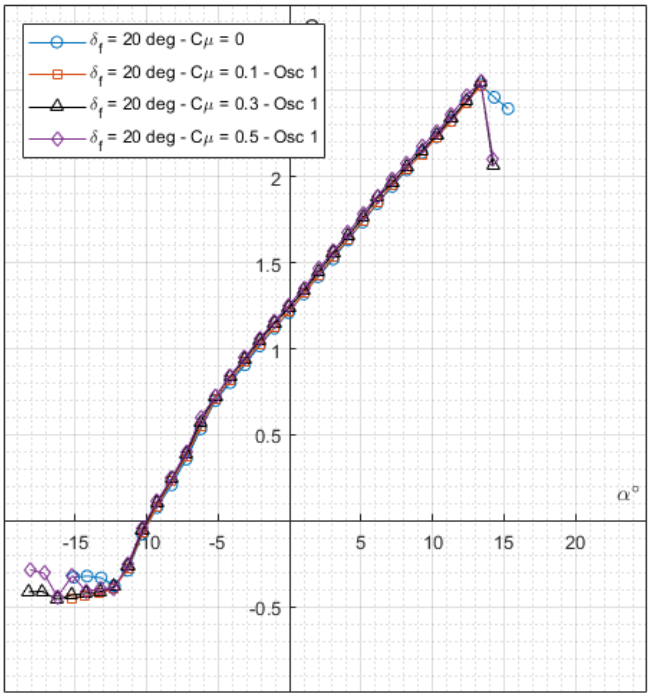

Fig. 3.61 Lift polar for the HLC with $\delta_f = 20°$ for the leading edge oscillators

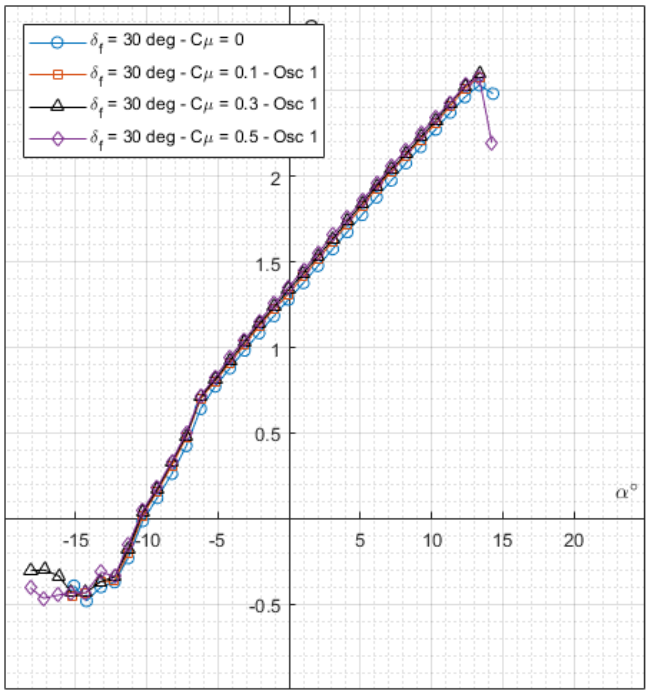

Fig. 3.62 Lift polar for the HLC with $\delta_f = 30°$ for the leading edge oscillators

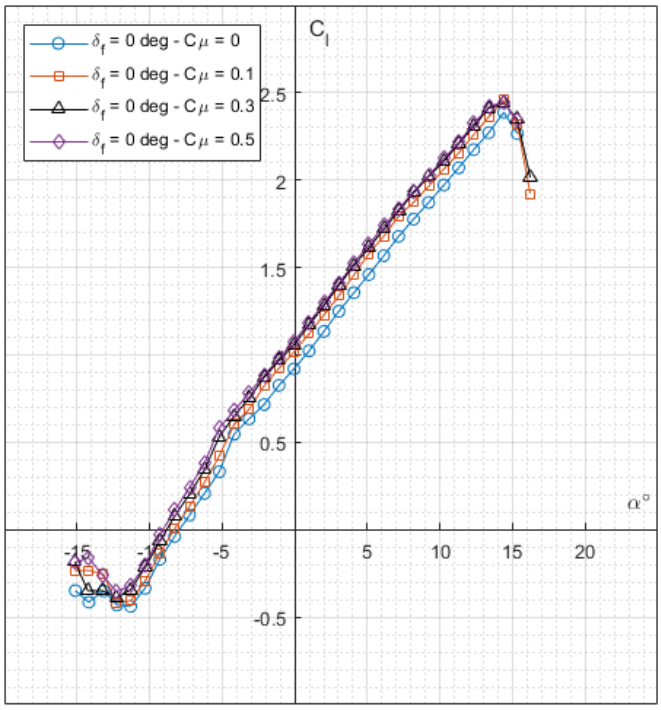

Fig. 3.63 Lift polar for the HLC with $\delta_f = 0°$ for the upper surface oscillators

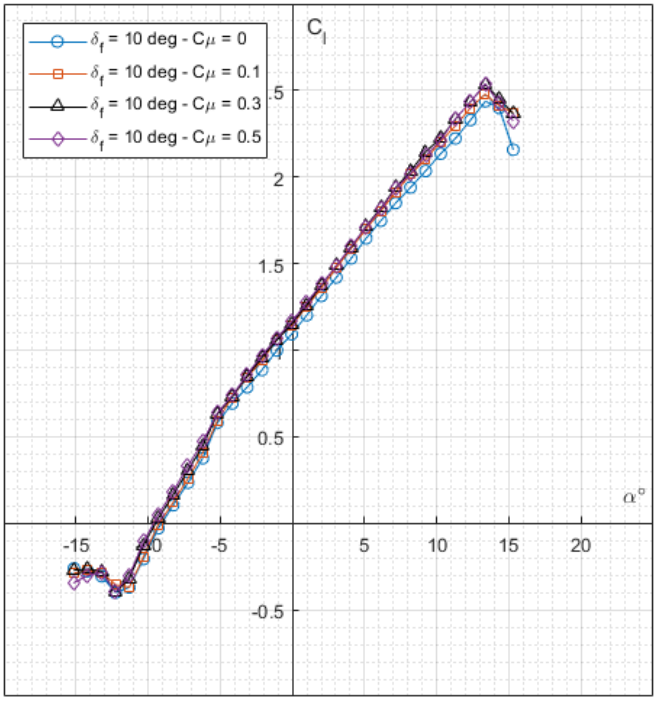

Fig. 3.64 Lift polar for the HLC with $\delta_f = 10°$ for the upper surface oscillators

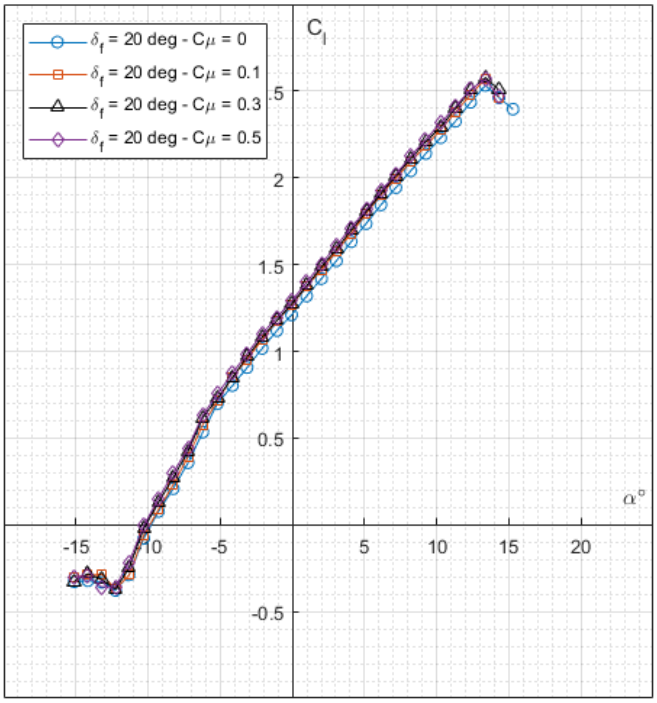

Fig. 3.65 Lift polar for the HLC with $\delta_f = 20°$ for the upper surface oscillators

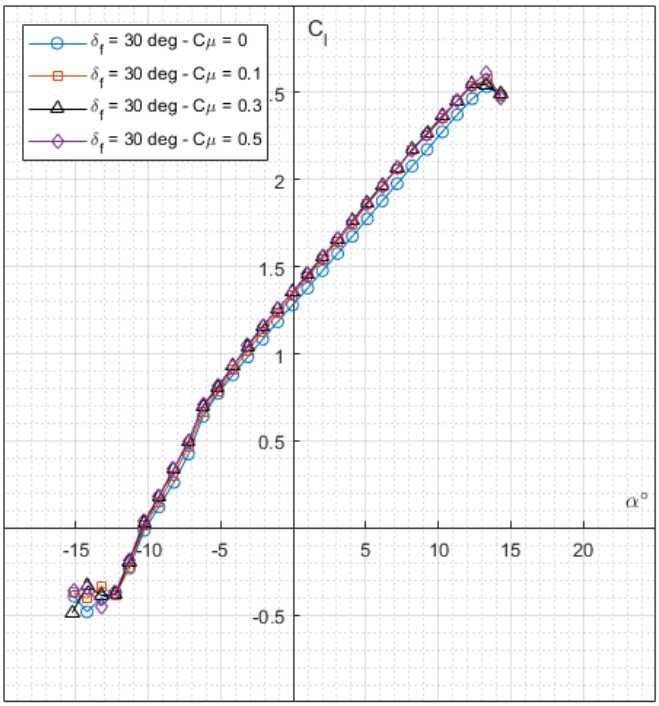

Fig. 3.66 Lift polar for the HLC with $\delta_f = 30°$ for the upper surface oscillators

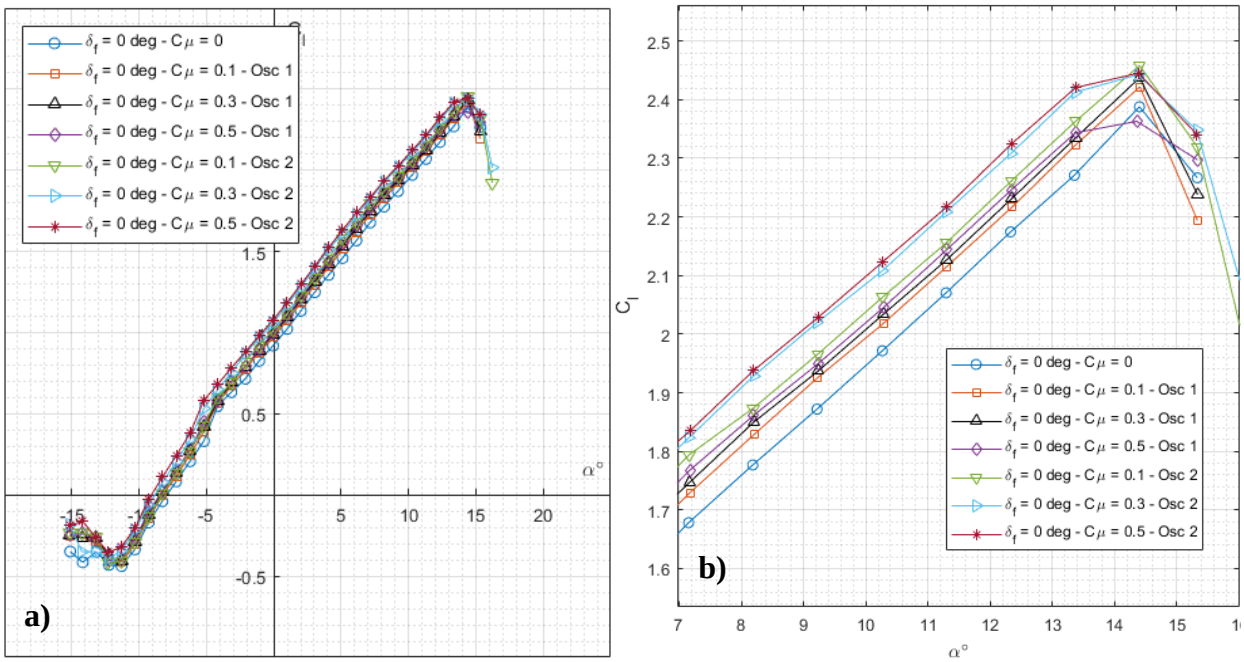

Fig. 3.67 Lift polar for HLC with $\delta_f = 0°$ for all oscillators. (left) full polar (right) positive α stall

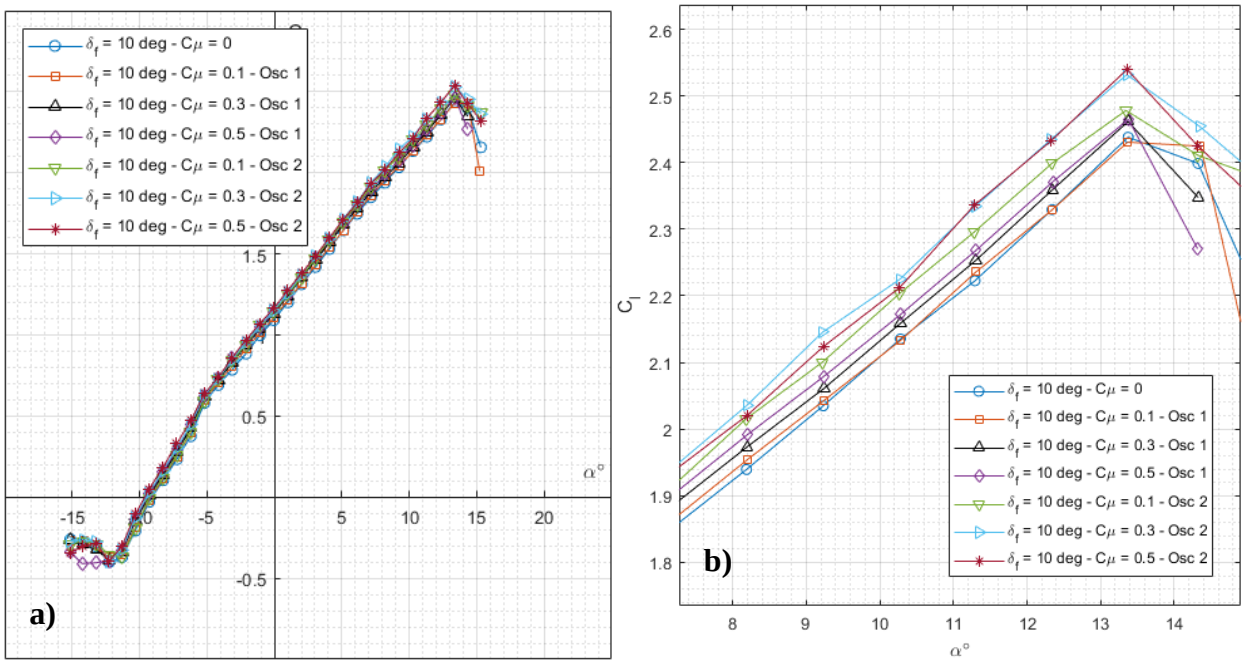

Fig. 3.68 Lift polar for HLC with $\delta_f = 10°$ for all oscillators. (left) full polar (right) positive α stall

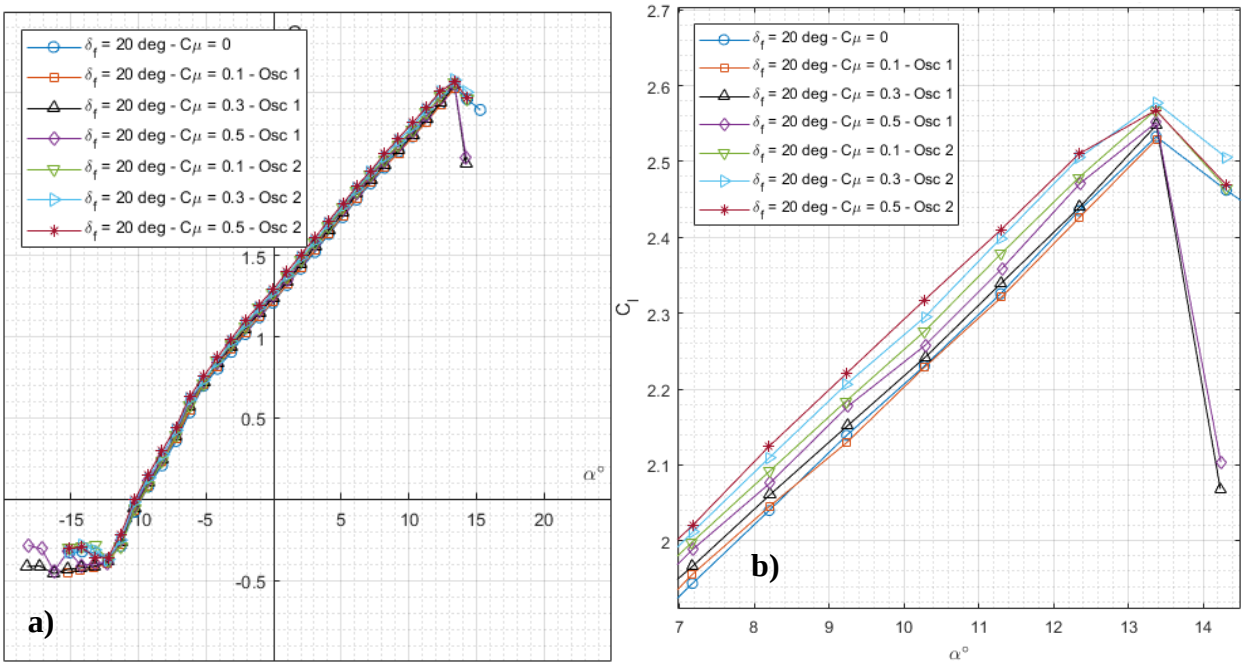

Fig. 3.69 Lift polar for HLC with $\delta_f = 20°$ for all oscillators. (left) full polar (right) positive α stall

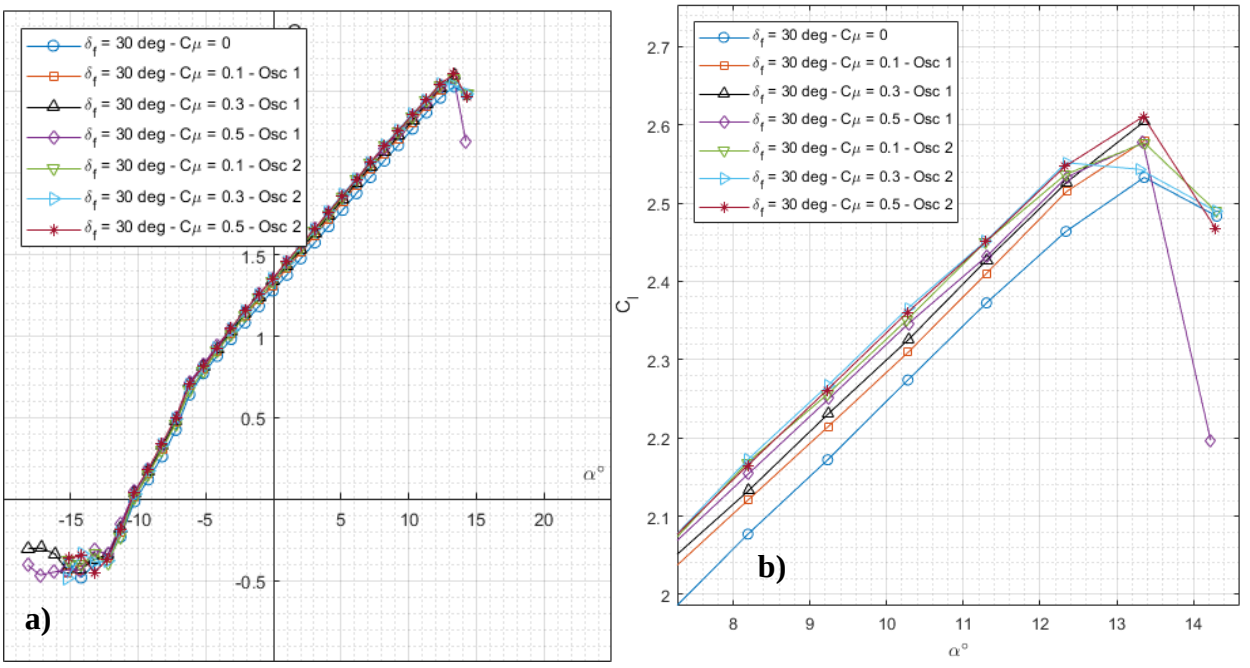

Fig. 3.70 Lift polar for HLC with $\delta_f = 30°$ for all oscillators. (left) full polar (right) positive α stall

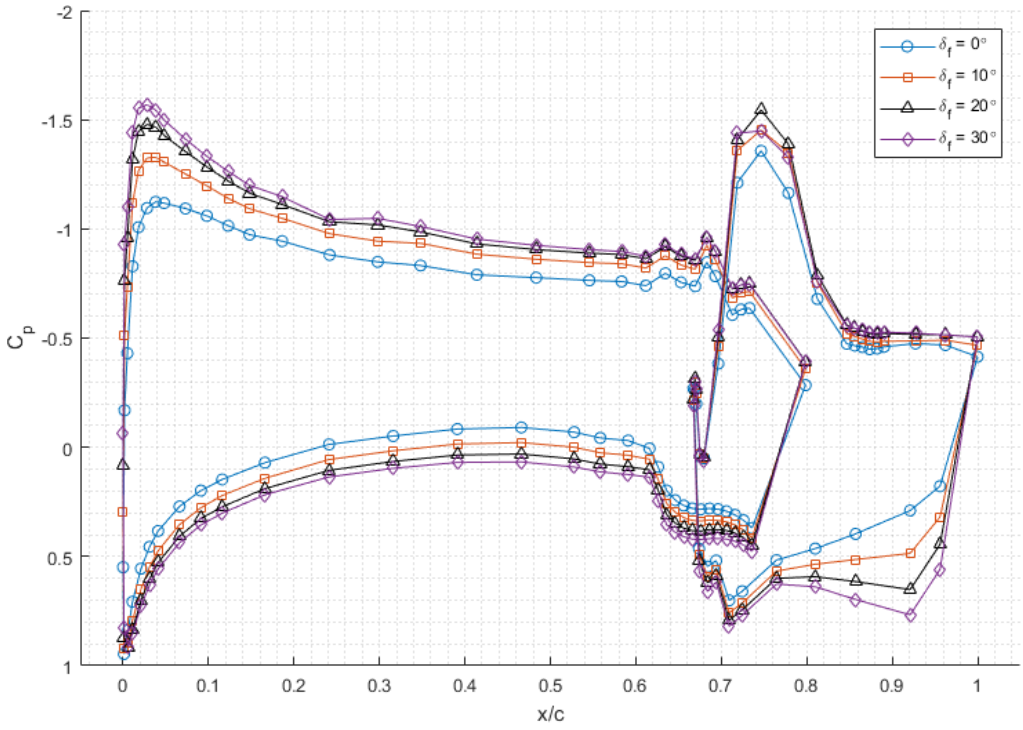

Fig. 3.71 C_P distributions for each δ_f at Re = 1.8e6, M = 0.18, and $\alpha = 1°$ with no actuation for the HLC

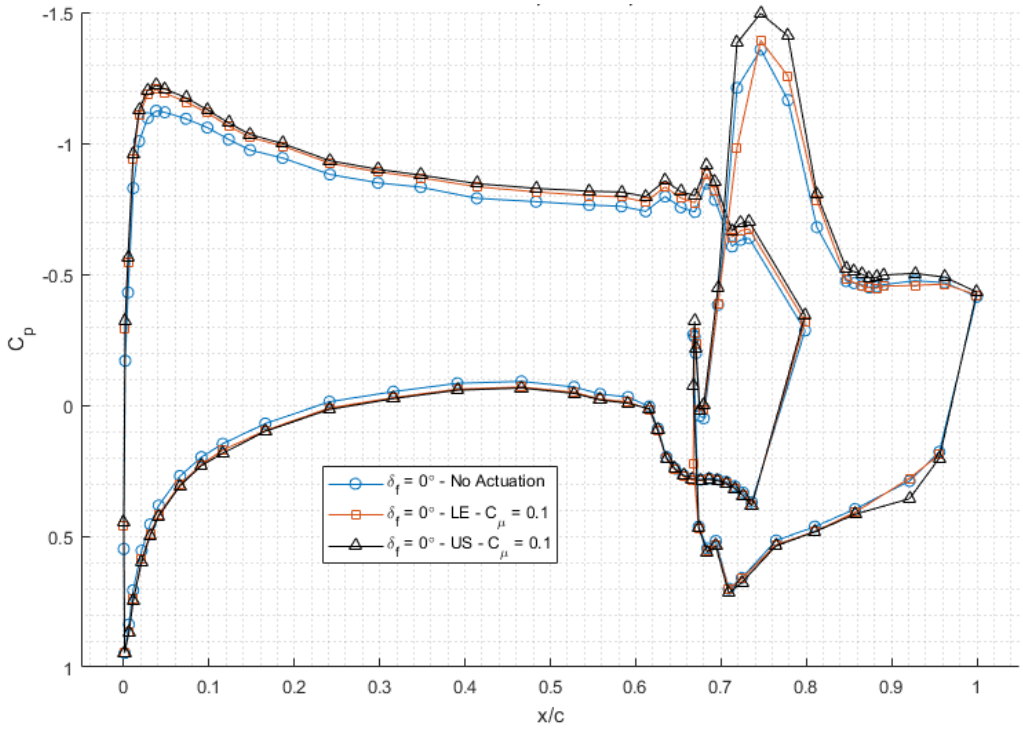

Fig. 3.72 C_P distributions for $\delta_f = 0°$ at Re = 1.8e6, M = 0.18, and $\alpha = 1°$ comparing each oscillator set for the HLC

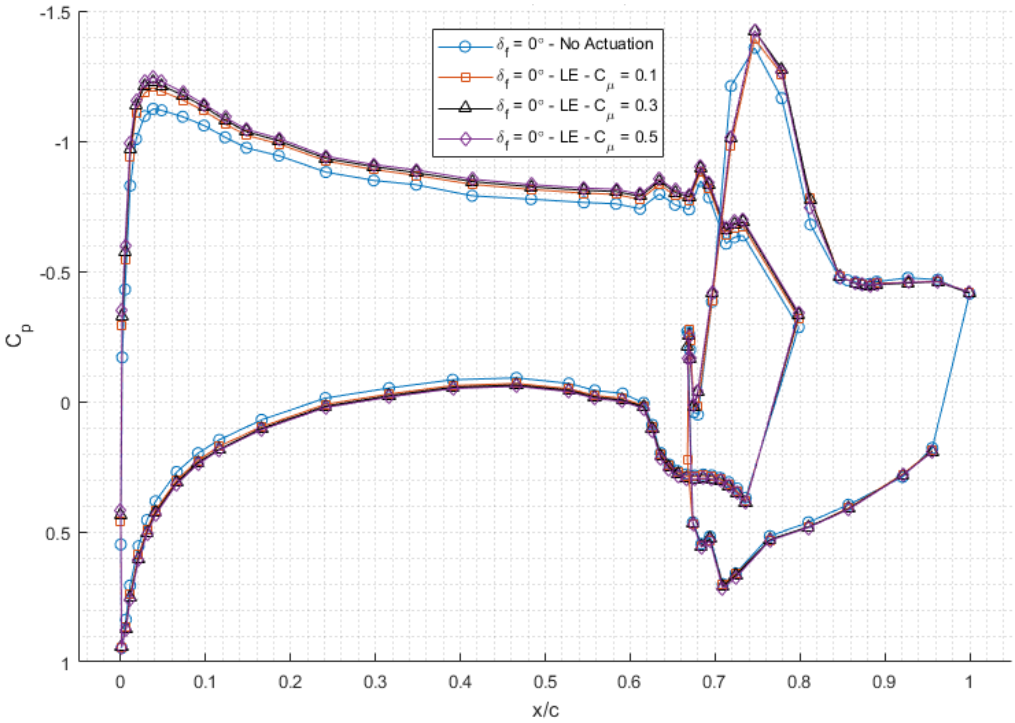

Fig. 3.73 C_P distributions for $\delta_f = 0°$ at Re = 1.8e6, M = 0.18, and $\alpha = 1°$ comparing the leading edge oscillators at various C_μ

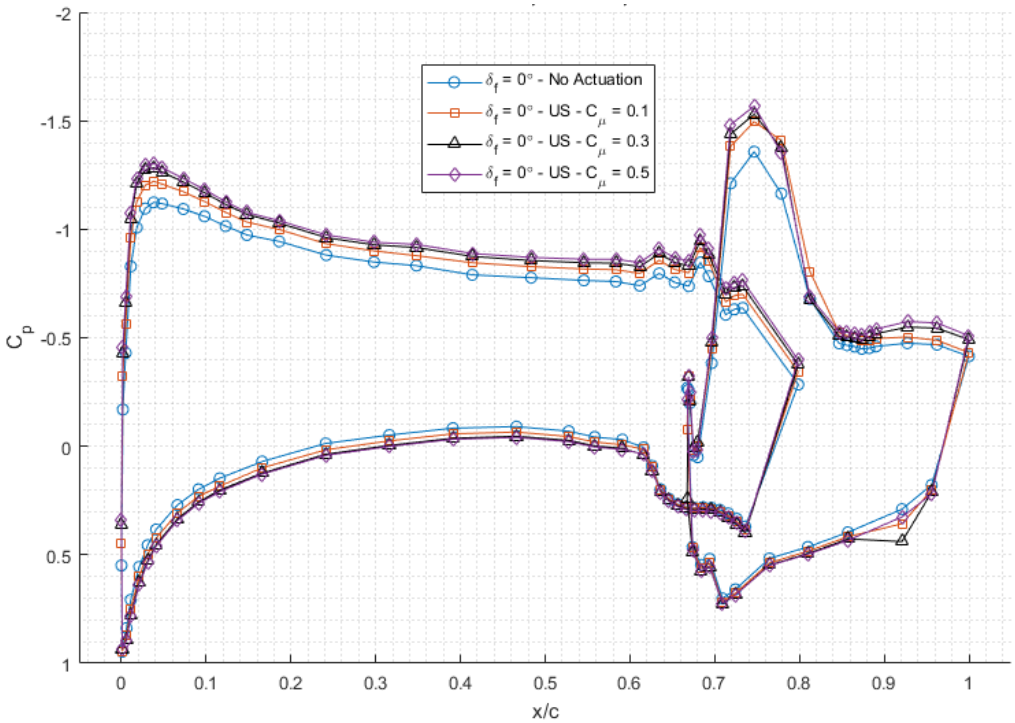

Fig. 3.74 C_P distributions for $\delta_f = 0°$ at Re = 1.8e6, M = 0.18, and $\alpha = 1°$ comparing the upper surface oscillators at various C_μ

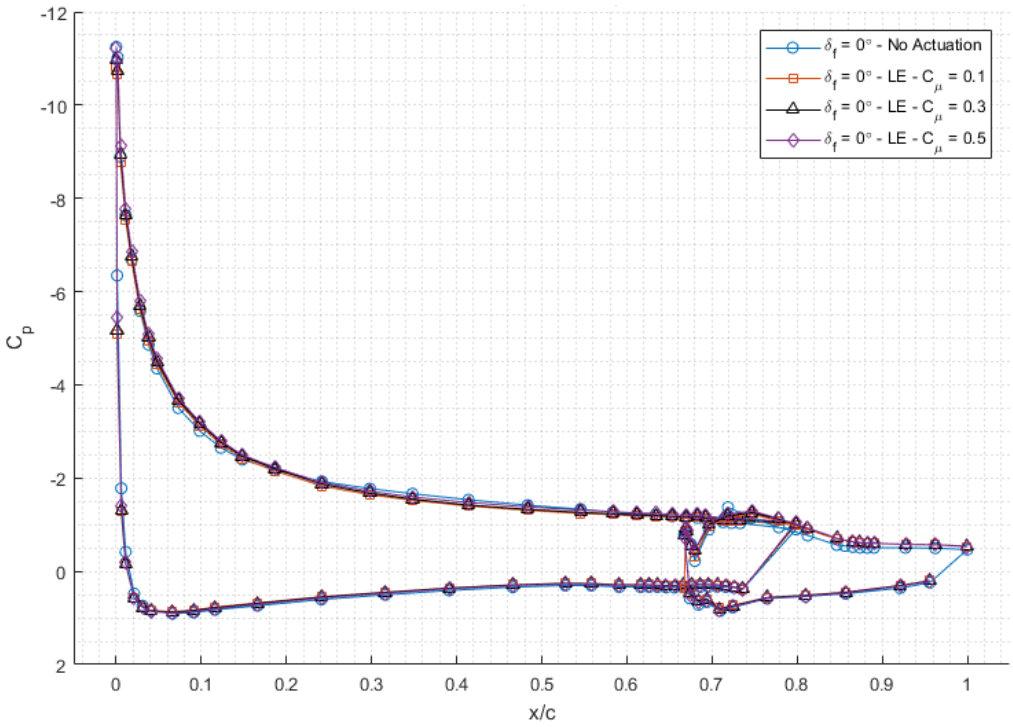

Fig. 3.75 C_P distributions for $\delta_f = 0°$ at Re = 1.8e6, M = 0.18, and $\alpha = 15°$ comparing the leading edge oscillators at various C_μ

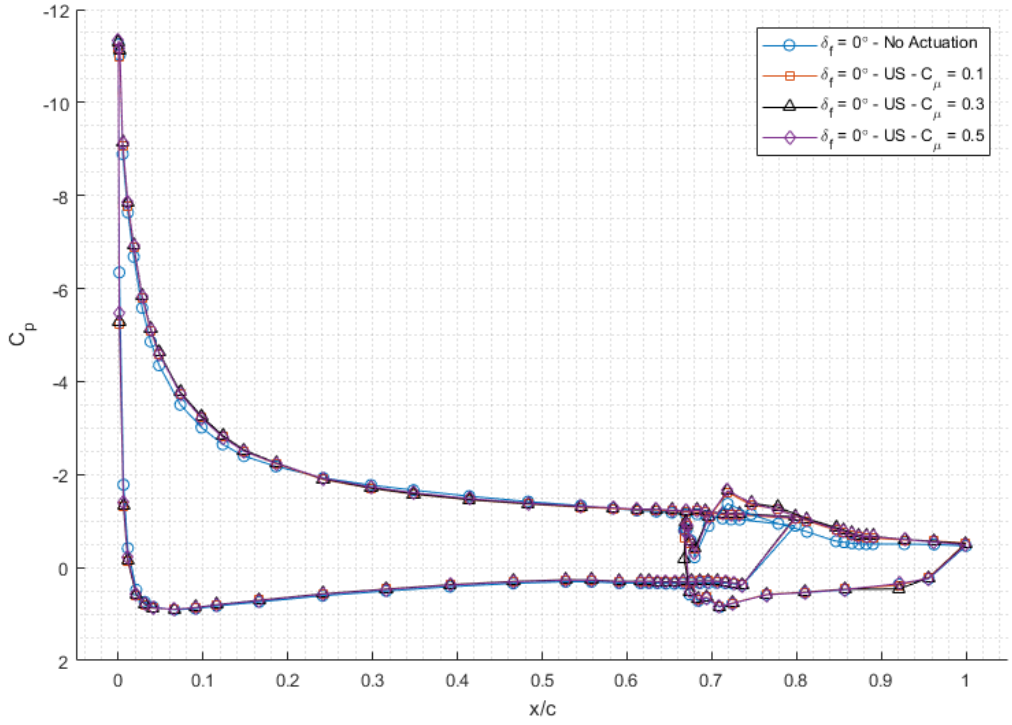

Fig. 3.76 C_P distributions for $\delta_f = 0°$ at Re = 1.8e6, M = 0.18, and $\alpha = 15°$ comparing the upper surface oscillators at various C_μ

Chapter 4: Summary and Conclusions

An experimental study was performed to investigate the effect of geometric variations on the frequency behavior of fluidic oscillators and study the influence of embedded fluidic oscillators for control of trailing-edge separation on a multi-element SNLF S414 airfoil. Fluidic oscillators are unique devices with no moving components that generate a constant sweeping planar jet whose frequency is dependent on the inlet conditions and internal geometry. This investigation was motivated by a desire to determine a model to predict the frequency behavior of the fluidic oscillators based on variations in their internal geometry and inlet conditions so that they can be sized to target certain F^+ and C_μ for flow control of a given wing. Using the oscillator model, this study then sought to better control trailing-edge separation for the S414 under different configurations and maximize the total lift of the airfoil.

Experiments were performed on 78 parametric variations of two different fluidic oscillator designs, one with a square internal geometry and sharp edges and one with a round internal geometry and round edges. Geometric variations include the inlet length, internal wedge length into the mixing chamber, outlet length, oscillator thickness, and overall oscillator scale. A hot-film probe was used to collect velocity data for each oscillator as it was cycled through a back pressure of 6.89 kPa (1 psig) to 34.45 kPa (5 psig) in 1.378 kPa (0.2 psig) increments. The oscillators were mounted vertically in a quiescent room to avoid any potential wall effects. A FFT was applied to

the hot-film data acquired for each oscillator and inlet pressure to build frequency curves, which illustrated the changing behaviors of the oscillators under varying geometric and inlet condition. It was found that square and round oscillators did not behave similarly under each geometric variation, but individually kept mostly consistent trends as the scale and aspect ratio of the oscillator varied. Overall, the round oscillators showed a smooth, monotonic increase in frequency that was linearly related to the inlet mass flow at an aspect ratio of 1; the square oscillators had a non-regular inconsistent increase in frequency with respect to an increase in inlet mass flow. The inconsistencies in the square oscillators could likely be attributed to a different behavior in the mixing chamber as a result of the sharp edges leading to larger regions of separation.

Due to the inconsistency in the square oscillator behavior, a model was only developed for the round oscillators. Using the calculated data, a non-linear multivariate analysis was performed, and a stepwise procedure was used to build a predictive model for the jet oscillation frequency of the round oscillators under varying geometric parameters and differing inlet conditions. This model demonstrated a good estimator of the collected data, with a $R^2_{adj} = 0.9546$. The model was able to capture important variations seen in the data, including different oscillator scales drastically changing the resultant frequency, in some cases by an order of magnitude, and the aspect ratio dependency of the slope of the frequency with respect to the inlet mass flow. Recommended future work includes continued development of the model and examining fluidic oscillators with scales outside of the tested range and geometric variations in other parameters such as feedback channels.

Using the newly-built model, a set of fluidic oscillators were sized to be embedded in the aft element of the S414. While sizing the fluidic oscillators for the S414 airfoil, $F^+ \approx 0.1$ and $C_\mu \approx 0.1 - 0.2\%$ were targeted. Additional constrains were introduced based on the limited internal space for the embedded oscillators and necessary pneumatic plumbing to supply them. The characteristic length for F^+ is the projected vertical distance from the top of a 10% chord flap on the aft element to its trailing edge. Since this projected distance is dependent on the angle of attack and flap deflection angle, the oscillators were sized for the S414 configuration to be close in order of magnitude to $F^+ \approx 0.1$ with $\delta_f = 0°$ and $\alpha = 0°$ with a $C_\mu \approx 0.1 - 0.2\%$, and it was expected that the F^+ would vary greatly during testing as C_μ was kept constant.

The S414 airfoil was tested in two different configurations, a baseline as-designed configuration and a high-lift configuration, where the aft element aggressively shifted to augment the lift of the airfoil system. The aft element was designed such that two rows of embedded

oscillators could be individually tested at 0.7c and 0.8c, corresponding to the aft element leading edge and upper surface, respectively. Data were collected for each S414 configuration at $\delta_f = 0°, 10°, 20°$ and $30°$ for each of the two rows of oscillators for a $C_\mu = 0.1\%, 0.3\%,$ and 0.5%. Few flow features on the baseline S414 configuration exist that would benefit from applied unsteady actuation. The effect from the leading-edge oscillators was mostly overpowered by the aft element suction peak and provided almost no increase in lift. While the upper surface oscillators did extend the favorable pressure gradient further aft, there was no appreciable increase in lift as this just shifted some loading from the fore element to the aft element. Overall, the baseline S414 configuration saw little improvement in the overall airfoil lift using fluidic oscillators, regardless of location or C_μ value.

In contrast, the high lift configuration has a large portion of the upper surface in the aft element separated and benefitted greatly by the application of flow actuation. The leading-edge oscillators did shift the lift curve up slightly, but the flow field was quickly "saturated" and saw diminishing gains after $C_\mu = 0.1\%$. Additionally, due to the new positioning of the aft element, the airflow dumping off the trailing edge of the fore element corresponded to a location similar to where the leading-edge oscillators were installed, which reduced the overall effectiveness of the applied actuation. However, the upper surface oscillators applied unsteady actuation at the edge of the large pressure spike from the dumping velocity, before the separated region. This resulted in a large shift in the lift curve even at a $C_\mu = 0.1$. Like the leading-edge oscillators, there were diminishing gains in lift as the C_μ was further increased. Overall, the HLC saw large improvements in the airfoil lift with applied unsteady actuation from both the leading-edge oscillators and the upper surface oscillators, however the upper surface oscillators were more efficient and generated larger improvements in airfoil lift.

Chapter 5: Uncertainty Analysis

As with all experimental investigations, there is a degree of uncertainty in the results, which is presented in this chapter. Analyzing the uncertainties in acquired data helps to assess the scatter in results over multiple trials[20], which allows for a better interpretation in the significance of experimental results. Kline and McClintock[21] and Airy[22] described the uncertainty in a measurement as the "possible value that an error may have". Bias and precision errors are the two forms of errors that appear in these experimental results. Uncertainties in the measurement capabilities of given equipment or accuracy of calibration is presented as bias error. These uncertainties can also be classified as "fixed" since these uncertainties create a repeatable and consistent offset from the true value. Random variance in experimental results is the source of precision errors. The combination of both bias and precision errors provides the best estimate in measurement errors[20].

A set of N observations of the variable (X) with a mean ($X_{(N)}$) has an associated precision or uncertainty (U_x), which can be calculated using[20],

$$U_x = \frac{tS_{(N)}}{\sqrt{N}} \tag{5.1}$$

In Eq (5.1 $S_{(N)}$ represents the standard deviation for the set of N observations that was used to calculate the mean $X_{(N)}$ and t is the Student's t statistic that is used to determine the level of confidence desired in the uncertainty calculations based on the number of samples N.

Several independently measured variables (x_i) are used to determine the reduced variable of an experiment (R) and is represented by,

$$R = R(x_1, x_2, \dots, x_n) \tag{5.2}$$

It can be assumed that the uncertainties of each measured variable are independent of each other since each measurement was acquired individually. The associated "bias" error (U_R) can thus be calculated by taking the root mean square of the uncertainty for each corresponding component used to calculate the reduced variable[21],

$$U_R = \sqrt{\left(\frac{\partial R}{\partial x_1} U_{x_1}\right)^2 + \left(\frac{\partial R}{\partial x_2} U_{x_2}\right)^2 + \cdots + \left(\frac{\partial R}{\partial x_n} U_{x_n}\right)^2} \tag{5.3}$$

Using the described method, resulting "bias" uncertainties associated with flow conditions, performance coefficients, and active flow control parameters are presented in section 5.1

5.1. Uncertainty in Performance Measurements

5.1.1. Uncertainty in Flow Conditions.

Flow condition uncertainties were calculated using the equations presented in this section. Table 5.1 gives examples of the calculated variables at a 95% confidence level for a given condition. Included are results for estimates of the freestream dynamic pressure, ambient density, ambient dynamic viscosity, freestream velocity, and Reynolds number. Ansell[23] presents a detailed derivation of each of these equations. These were calculated using,

$$U_{q_\infty} = \sqrt{\left(\frac{\partial q_\infty}{\partial (P_{ss} - P_{ts})} U_{(P_{ss} - P_{ts})}\right)^2} \tag{5.4}$$

$$U_{\rho_{amb}} = \sqrt{\left(\frac{\partial \rho_{amb}}{\partial P_{amb}} U_{P_{amb}}\right)^2 + \left(\frac{\partial \rho_{amb}}{\partial T_{amb}} U_{T_{amb}}\right)^2} \tag{5.5}$$

$$U_{\mu_{amb}} = \sqrt{\left(\frac{\partial \mu_{amb}}{\partial T_{amb}} U_{T_{amb}}\right)^2} \tag{5.6}$$

$$U_{U_\infty} = \sqrt{\left(\frac{\partial U_\infty}{\partial q_\infty} U_{q_\infty}\right)^2 + \left(\frac{\partial U_\infty}{\partial \rho_{amb}} U_{\rho_{amb}}\right)^2} \tag{5.7}$$

$$U_{Re} = \sqrt{\left(\frac{\partial Re}{\partial U_\infty} U_{U_\infty}\right)^2 + \left(\frac{\partial Re}{\partial \rho_{amb}} U_{\rho_{amb}}\right)^2 + \left(\frac{\partial Re}{\partial \mu_{amb}} U_{\mu_{amb}}\right)^2 + \left(\frac{\partial Re}{\partial c} U_c\right)^2} \tag{5.8}$$

5.1.2. Uncertainty in the Pressure and Performance Coefficients

Uncertainties associated with the pressure and performance coefficient results, C_p, C_l, $C_{m,LE}$, and C_d were calculated using the equations presented in this section. Collazo[24] presents a detailed derivation of C_p, C_l, $C_{m,LE}$, while Ansell[23] presents a derivation for C_d. Table 5.2 presents examples of the calculated uncertainties from this section, similarly for a 95% confidence level. Uncertainties were calculated using,

$$U_{C_p} = \sqrt{\left(\frac{\partial C_p}{\partial \Delta P} U_{\Delta P}\right)^2 + \left(\frac{\partial C_p}{\partial P_0} U_{P_0}\right)^2 + \left(\frac{\partial C_p}{\partial P_\infty} U_{P_\infty}\right)^2} \tag{5.9}$$

$$U_{C_n} = \sqrt{\begin{array}{c}\left(\frac{\partial C_n}{\partial C_{p_{l,i+1}}} U_{C_{p_{l,i+1}}}\right)^2 + \left(\frac{\partial C_n}{\partial C_{p_{l,i}}} U_{C_{p_{l,i}}}\right)^2 + \left(\frac{\partial C_n}{\partial C_{p_{u,i+1}}} U_{C_{p_{u,i+1}}}\right)^2 + \cdots \\ \left(\frac{\partial C_n}{\partial C_{p_{u,i}}} U_{C_{p_{u,i}}}\right)^2 + \left(\frac{\partial C_n}{\partial x_{l,i+1}} U_{x_{l,i+1}}\right)^2 + \cdots \\ \left(\frac{\partial C_n}{\partial x_{l,i}} U_{x_{l,i}}\right)^2 + \left(\frac{\partial C_n}{\partial x_{u,i+1}} U_{x_{u,i+1}}\right)^2 + \left(\frac{\partial C_n}{\partial x_{u,i}} U_{x_{u,i}}\right)^2\end{array}} \tag{5.10}$$

$$U_{C_a} = \sqrt{\begin{array}{c}\left(\frac{\partial C_a}{\partial C_{p_{l,i+1}}} U_{C_{p_{l,i+1}}}\right)^2 + \left(\frac{\partial C_a}{\partial C_{p_{l,i}}} U_{C_{p_{l,i}}}\right)^2 + \left(\frac{\partial C_a}{\partial C_{p_{u,i+1}}} U_{C_{p_{u,i+1}}}\right)^2 + \cdots \\ \left(\frac{\partial C_a}{\partial C_{p_{u,i}}} U_{C_{p_{u,i}}}\right)^2 + \left(\frac{\partial C_a}{\partial y_{l,i+1}} U_{y_{l,i+1}}\right)^2 + \left(\frac{\partial C_a}{\partial y_{l,i}} U_{y_{l,i}}\right)^2 + \cdots \\ \left(\frac{\partial C_a}{\partial y_{u,i+1}} U_{y_{u,i+1}}\right)^2 + \left(\frac{\partial C_a}{\partial y_{u,i}} U_{y_{u,i}}\right)^2\end{array}} \tag{5.11}$$

$$U_{C_l} = \sqrt{\left(\frac{\partial C_l}{\partial C_n} U_{C_n}\right)^2 + \left(\frac{\partial C_l}{\partial C_a} U_{C_a}\right)^2 + \left(\frac{\partial C_l}{\partial \alpha} U_\alpha\right)^2} \tag{5.12}$$

$$U_{C_{m,LE}} = \sqrt{\begin{array}{c}\left(\frac{\partial C_{m,LE}}{\partial C_{p_{l,i+1}}} U_{C_{p_{l,i+1}}}\right)^2 + \left(\frac{\partial C_{m,LE}}{\partial C_{p_{l,i}}} U_{C_{p_{l,i}}}\right)^2 + \left(\frac{\partial C_{m,LE}}{\partial C_{p_{u,i+1}}} U_{C_{p_{u,i+1}}}\right)^2 + \cdots \\ \left(\frac{\partial C_{m,LE}}{\partial C_{p_{u,i}}} U_{C_{p_{u,i}}}\right)^2 + \left(\frac{\partial C_{m,LE}}{\partial y_{l,i+1}} U_{y_{l,i+1}}\right)^2 + \left(\frac{\partial C_{m,LE}}{\partial y_{l,i}} U_{y_{l,i}}\right)^2 + \cdots \\ \left(\frac{\partial C_{m,LE}}{\partial y_{u,i+1}} U_{y_{u,i+1}}\right)^2 + \left(\frac{\partial C_{m,LE}}{\partial y_{u,i}} U_{y_{u,i}}\right)^2 + \left(\frac{\partial C_{m,LE}}{\partial x_{l,i+1}} U_{x_{l,i+1}}\right)^2 + \cdots \\ \left(\frac{\partial C_{m,LE}}{\partial x_{l,i}} U_{x_{l,i}}\right)^2 + \left(\frac{\partial C_{m,LE}}{\partial x_{u,i+1}} U_{x_{u,i+1}}\right)^2 + \left(\frac{\partial C_{m,LE}}{\partial x_{u,i}} U_{x_{u,i}}\right)^2\end{array}} \tag{5.13}$$

$$U_{C_{m,c/4}} = \sqrt{\left(\frac{\partial C_{m,c/4}}{\partial C_{m,LE}} U_{C_{m,LE}}\right)^2 + \left(\frac{\partial C_{m,c/4}}{\partial C_l} U_{C_l}\right)^2} \tag{5.14}$$

$$U_{C_d} = \sqrt{\left(\frac{\partial C_d}{\partial q_\infty} U_{q_\infty}\right)^2 + \left(\frac{\partial C_d}{\partial c} U_c\right)^2 + \left(\frac{\partial C_d}{\partial P_{0,\infty}} U_{P_{0,\infty}}\right)^2 + \sum_{i=1}^{n_{wake}-1} \left(\frac{\partial C_d}{\partial P_{0,w}} U_{P_{0,w}}\right)^2} \tag{5.15}$$

The partial derivatives for $C_{m,LE}$ used in this study were calculated using,

$$\frac{\partial C_{m,LE}}{\partial C_{p_{u,i+1}}} = \sum \frac{({y_{u,i+1}}^2 - {y_{u,i}}^2)}{2} + \sum \frac{({x_{u,i+1}}^2 - {x_{u,i}}^2)}{2} \tag{5.16}$$

$$\frac{\partial C_{m,LE}}{\partial C_{p_{u,i}}} = \sum \frac{({y_{u,i+1}}^2 - {y_{u,i}}^2)}{2} + \sum \frac{({x_{u,i+1}}^2 - {x_{u,i}}^2)}{2} \tag{5.17}$$

$$\frac{\partial C_{m,LE}}{\partial C_{p_{l,i+1}}} = \sum \frac{({y_{l,i+1}}^2 - {y_{l,i}}^2)}{2} + \sum \frac{({x_{l,i+1}}^2 - {x_{l,i}}^2)}{2} \tag{5.18}$$

$$\frac{\partial C_{m,LE}}{\partial C_{p_{l,i}}} = \sum \frac{({y_{l,i+1}}^2 - {y_{l,i}}^2)}{2} + \sum \frac{({x_{l,i+1}}^2 - {x_{l,i}}^2)}{2} \tag{5.19}$$

$$\frac{\partial C_{m,LE}}{\partial y_{u,i+1}} = \sum \frac{(C_{p_{u,i+1}} + C_{p_{u,i}})}{2} y_{u,i+1} \tag{5.20}$$

$$\frac{\partial C_{m,LE}}{\partial y_{u,i}} = -\sum \frac{(C_{p_{u,i+1}} + C_{p_{u,i}})}{2} y_{u,i} \tag{5.21}$$

$$\frac{\partial C_{m,LE}}{\partial y_{l,i+1}} = -\sum \frac{(C_{p_{l,i+1}} + C_{p_{l,i}})}{2} y_{l,i+1} \tag{5.22}$$

$$\frac{\partial C_{m,LE}}{\partial y_{l,i}} = \sum \frac{(C_{p_{l,i+1}} + C_{p_{l,i}})}{2} y_{l,i} \tag{5.23}$$

$$\frac{\partial C_{m,LE}}{\partial x_{u,i+1}} = \sum \frac{(C_{p_{u,i+1}} + C_{p_{u,i}})}{2} x_{u,i+1} \tag{5.24}$$

$$\frac{\partial C_{m,LE}}{\partial x_{u,i}} = -\sum \frac{(C_{p_{u,i+1}} + C_{p_{u,i}})}{2} x_{u,i} \tag{5.25}$$

$$\frac{\partial C_{m,LE}}{\partial x_{l,i+1}} = -\sum \frac{(C_{p_{l,i+1}} + C_{p_{l,i}})}{2} x_{l,i+1} \tag{5.26}$$

$$\frac{\partial C_{m,LE}}{\partial x_{l,i}} = \sum \frac{(C_{p_{l,i+1}} + C_{p_{l,i}})}{2} x_{l,i} \tag{5.27}$$

5.2. Uncertainty in Active Flow Control Parameters

The associated uncertainties for the non-dimensional actuation frequency, jet momentum coefficient, and oscillator frequency were calculated using the following equations. Table 5.3 presents examples of these calculated uncertainties at a 95% confidence level.

$$U_{l_c} = \sqrt{\left(\frac{\partial l_c}{\partial c_t} U_{c_f}\right)^2 + \left(\frac{\partial l_c}{\partial \alpha_m} U_{\alpha_m}\right)^2 + \left(\frac{\partial l_c}{\partial \alpha_{tab}} U_{\alpha_{tab}}\right)^2} \tag{5.28}$$

$$U_f = \sqrt{\left(\frac{\partial f}{\partial \dot{v}} U_{\dot{v}}\right)^2 + \left(\frac{\partial f}{\partial l_o} U_{l_o}\right)^2 + \left(\frac{\partial f}{\partial l_t} U_{l_t}\right)^2 + \left(\frac{\partial f}{\partial l_w} U_{l_w}\right)^2 + \left(\frac{\partial f}{\partial t} U_t\right)^2} \tag{5.29}$$

$$U_{F^+} = \sqrt{\left(\frac{\partial F^+}{\partial U_\infty} U_{U_\infty}\right)^2 + \left(\frac{\partial F^+}{\partial f} U_f\right)^2 + \left(\frac{\partial F^+}{\partial l_c} U_{l_c}\right)^2} \tag{5.30}$$

$$U_{C_\mu} = \sqrt{\begin{array}{c}\left(\frac{\partial C_\mu}{\partial c} U_c\right)^2 + \left(\frac{\partial C_\mu}{\partial b} U_b\right)^2 + \left(\frac{\partial C_\mu}{\partial t} U_t\right)^2 + \left(\frac{\partial C_\mu}{\partial l_o} U_{l_o}\right)^2 + \cdots \\ \left(\frac{\partial C_\mu}{\partial \dot{m}} U_{\dot{m}}\right)^2 + \left(\frac{\partial C_\mu}{\partial U_\infty} U_{U_\infty}\right)^2 + \left(\frac{\partial C_\mu}{\partial \rho_{amb}} U_{\rho_{amb}}\right)^2\end{array}} \tag{5.31}$$

5.3. Uncertainty in Frequency Model Development

The uncertainties in the development of the predictive model for fluidic oscillator frequencies are addressed in this section. This includes uncertainty in hot-film measurements, FFT analysis, and the non-linear multivariate regression.

5.3.1. Hot-Film Measurements

Many potential uncertainty sources exist for hot-film probe measurements. These can include calibration, probe vibration, probe angle effects, and heat conduction. Hot-film calibration

is described by Ansell[23], where it was assumed to be the largest contributing factor to uncertainty. Flow angularity was considered the largest source of uncertainty in Whalen[25], where a detailed analysis of flow angularity uncertainty, along with probe vibration and heat conduction uncertainties, are described. In this study, hot-film measurements were used only for to determine the frequencies of each fluidic oscillator, flow velocities were not calculated or used. It is assumed that the uncertainties would present as bias error and result in an offset that will not affect the resulting frequencies recorded. There would, however, be uncertainties in the FFT determining the resulting frequencies, which is detailed in section 5.3.2.

5.3.2. Uncertainty in FFT determination of frequency

Uncertainty in the determination of frequency, amplitude, and phase with FFT come from two main sources, quantization and time jitter[26]. For synchronous sampling, the uncertainty in the amplitude and phase tones is equal to the uncertainty in corresponding DFT samples, while asynchronous sampling also results in uncertainties from spectral leakage[27]. During this study, however, it will be assumed that these errors are negligible compared to the errors introduced by the frequency resolution of the PSDs used to identify the resulting frequencies. Frequency resolution is dependent on the size of the Hamming window used to isolate various segments for FFT analysis. This results in a frequency uncertainty of ±1 Hz and ±1.33 Hz for the round and square oscillators respectively, which was incorporated into the evaluation of the frequency uncertainty used in Eq (5.29.

5.3.3. Uncertainty in the predictive model

Resulting statistical data from the development of the predictive frequency model can be seen in Table 3.1. A summary of standard deviations in each coefficient determined from the non-linear regression model can be seen in this table. The model resulted in an $R^2{}_{adj} = 0.9546$ and a $R^2 = 0.9549$, indicated a large portion of the data variance can be correlated to the model. For this study it will be assumed that there is an additional 4.51% uncertainty in frequency prediction due to the fit of the model to the collected data. This additional uncertainty was incorporated in Eq (5.29 through an additional term, which in addition to the uncertainty from section 5.3.2, results in the following modified uncertainty equation,

$$U_f = \sqrt{\left(\frac{\partial f}{\partial \dot{v}} U_{\dot{v}}\right)^2 + \left(\frac{\partial f}{\partial l_o} U_{l_o}\right)^2 + \left(\frac{\partial f}{\partial l_t} U_{l_t}\right)^2 + \left(\frac{\partial f}{\partial l_w} U_{l_w}\right)^2 + \cdots \left(\frac{\partial f}{\partial t} U_t\right)^2 + {U_{window}}^2 + (f(1-R^2))^2} \quad (5.32)$$

5.4. Chapter 5 Tables

Table 5.1 Example uncertainties for test conditions of the SNLF S414 at $Re_c = 1.8x10^6$ and $\alpha = 5°$ with $\delta_f = 10°$ and $C_\mu = 0.3$

Parameter	Reference Value	Absolute Uncertainty	Relative Uncertainty (%)
c	18 in	±0.005 in	±0.0278
α	4.987°	±0.02°	±0.4010
$q_{\infty,setra}$	0.3144 psi	±0.000771 psi	±0.2451
$q_{\infty,PSI}$	0.3159 psi	±0.001425 psi	±0.4513
P_{amb}	14.494 psi	±0.008 psi	±0.0552
T_{amb}	531.71°R	±1.8°R	±0.3385
ρ_{amb}	2.288E-03 slugs/ft^3	±7.745E-06 slugs/ft^3	±0.3385
μ_{amb}	3.810E-07 lb-s/ft^2	±1.265E-09 lb-s/ft^2	±0.3319
U_∞	199.0 ft/s	±0.3368 ft/s	±0.1693
Re_c	1791933	±9034	±0.5042

Table 5.2 Example uncertainties for airfoil pressure and performance coefficients of the SNLF S414 at $Re_c = 1.8x10^6$ and $\alpha = 5°$ with $\delta_f = 10°$ and $C_\mu = 0.3$

Parameter	Reference Value	Absolute Uncertainty	Relative Uncertainty (%)
C_p 5 psi (x/c=0.00167)	-1.1647	±0.012551	±1.0776
C_p 1 psi (x/c=0.61167)	-0.7595	±0.005603	±0.7377
C_l	0.94573	±0.047006	±4.9703
$C_{m,c/4}$	-0.13073	±0.019980	±15.2837
C_d	0.01963	±0.000719	±3.6602

Table 5.3 Example uncertainties for active unsteady flow control parameters of the SNLF S414 at $Re_c = 1.8x10^6$ and $\alpha = 5°$ with $\delta_f = 10°$ and $C_\mu = 0.3$

Parameter	Reference Value	Absolute Uncertainty	Relative Uncertainty (%)
f	1068.6 Hz	±49.979 Hz	±4.6772
F^+	5.904	±0.284	±4.8153
C_μ	0.30355	±0.00899	±2.9602

References

[1] Ostermann, F., Woszidlo, R., Nayeri, C.N., Paschereit, C.O., "Experiemental Comparison between the Flow Field of Two Common Fluidic Oscillator Designs," AIAA SciTech Forum, 53rd Aerospace Sciences Meeting, 5-9 January 2015, Kissimmee FL, AIAA Paper 2015-0781.

[2] Woszidlo, R., Ostermann, F., Nayeri, C.N., Paschereit, C.O., "The time-resolved natural flow field of a fluidic oscillator," Springer Exp Fluids (2015) 56:125, 3 June 2015, DOI 10.1007/s00348-015-1993-8.

[3] Gartlein, S., Woszidlo, R., Ostermann, F., Nayeri, C.N., Paschereit, C.O., "The Time-Resolved Internal and Externaml Flow Field Properties of a Fluidic Oscillator," AIAA SciTech Forum, 52nd Aerospace Sciences Meeting, 13-17 January 2014, National Harbour MD, AIAA Paper 10.2514/6.2014-1143.

[4] Bobusch, B.C., Woszidlo, R., Bergada, J.M., Nayeri, C.N., and Paschereit, C. O., "Experimental study of the internal flow structures inside a fluidic oscillator," Exp Fluids (2015) 54:1559, 11 Nov 2012, DOI 10.1007/s00348-013-1559-6.

[5] Bobusch, B. C., Woszidlo, R., Kruger, O., Paschereit, O., "Numerical Investigations on Geometric Parameters Affecting the Oscillation Properties of a Fluidic Oscillator," AIAA 21st Computational Fluid Dynamics Conference, 24-27 June 2013, San Diego CA, AIAA Paper 2013-2709.

[6] Seo, J. H., and Mittal, R., "Computational Modeling and analysis of Sweeping Jet Fluidic Oscillators," AIAA Aviation Forum. 47th AIAA Fluid Dynamics Conference, 5-9 June 2017, Denver Co, AIAA Paper 10.2514/6.2017-3312.

[7] Hossian, M.A., et al., "Effects of Roughness on the Performance of Fluidic Oscillators," AIAA SciTech Forum, 55th Aerospace Sciences Meeting, 9-13 January 2017, Grapevine TX, AIAA Paper 2017-0770.

[8] Griffin, J., Oyarzun, M., Cattafesta, L. N., Tu, J. H., Rowley, C. W., Mittal, R., "Control of a canonical separated flow," 43rd Fluid Dynamics Conference, 2013.

[9] Gupta, R. and Ansell, P.J., "Closed-Loop Trailing-Edge Separation Control System Using Empirical Mode Decomposition," *AIAA Journal*, Vol. 56, No. 1, 2018, pp. 121-131.

[10] Volino, R. J., Kartuzova, O., Ibrahim, M. B., "Separation Control on a Very High Lift Low Pressure Turbine Airfoil Using Pulsed Vortex Generator Jets," J. Turbomach, 133, 041021, 2011, 13 pages; doi:10.1115/1.4003024.

[11] Amitay, M., Glezer, A., "Role of actuation frequency in controlled flow reattachment over a stalled airfoil," AIAA journal, 40(2), 2002, pp. 209-216.

[12] Somers, Dan M. and Maughmer, Mark D., "Design and Experimental Results for the S414 Airfoil," U.S. Army Research, Development and Engineering Command, RDECOM TR 10-D-112, Aug. 2010.

[13] Maughmer, Mark D., Premi, Amandeep and Somers, Dan M., "Exploration of a Slotted Laminar-Flow-Control Airfoil Concept," Final Technical Report – NASA Grant No. NNX13AB86A, Nov. 2013.

[14] Twiss, D., "High-Lift Configuration of a Slotted Natural Laminar Flow Airfoil," Master's Thesis, University of Illinois at Urbana–Champaign, Urbana, IL, 2019.

[15] Catalano, F.M., et al., "Wind Tunnel Wall Boundary Layer Control for 2D High Lift Wing Testing," 24th International Congress of the Aeronautical Sciences, 29 Aug - 3 Sept 2004, Yokohama Japan.

[16] Paschal, K., et al., "Evaluation of Tunnel Sidewall Boundary Layer = Control Systems for High-Lift Airfoil Testing," AIAA 9th Applied Aerodynamics Conference, 23-25 September 1991, Baltimore MD, AIAA Paper 91-3243

[17] Jones, B. M., "Measurement of Profile Drag by the Pitot-Traverse Method," Tech. Rep. 1688, Aeronautical Research Council R&M, 1936.

[18] Schlichting, H., "Boundary-Layer Theory," McGraw-Hill Book Company, New York, 1979.

[19] Barlow, J.B., Rae, W.H. Jr. and Pope, A., "Low-Speed Wind Tunnel Testing," 3rd Edition, John Wiley & Sons, Inc., New York, 1999.

[20] Moffat, R.J., "Describing the Uncertainties in Experimental Results," Experimental and Thermal Fluid Sciences, Vol. 1, No. 1, 1988, pp. 3–17.

[21] Kline, S. J., and McClintock, F. A., "Describing Uncertainties in Single Sample Experiments," Mech. Eng., 3-8 Jan. 1953.

[22] Airy, Sir George Biddle, "Theory of Errors of Observation," Macmillan, London, 1879.

[23] Ansell, P.J., "Unsteady Modes in the Flowfield about an Airfoil with a Leading-Edge Horn-Ice Shape," Ph.D. Dissertation, University of Illinois at Urbana-Champaign, Urbana, IL, 2013.

[24] Collazo Garcia III, A., "Aerodynamic Characterization of a Griffith-Type Transonic, Laminar-Flow Airfoil," Master's Thesis, University of Illinois at Urbana–Champaign, Urbana, IL, 2019.

[25] Whalen, E.A., "Aerodynamics of Runback Ice Accretions," Ph.D. Dissertation, University of Illinois at Urbana–Champaign, Urbana, IL, 2007.

[26] Betta, G., Liguori, C., Pietrosanto, A., "Propagation of uncertainty in a discrete Fourier transform algorithm," *Measurement*, Vol. 27, Issue 4, 2000, pp. 231-239.

[27] Liguori, C. "Uncertainty on Signal Parameter Estimation in Frequency Domain," 11th IMEKO TC-4 Symp., 13-14 September 2001, Lisbon Portugal, ISBN 972-98115-4-7